# Using frozen hydrogen particles to observe rotating and quantized flows in liquid helium

A Dissertation
Presented to the Faculty of the Graduate School
of
Yale University
In Candidacy for the Degree of
Doctor of Philosophy

by
Gregory P. Bewley

Dissertation Director: Katepalli R. Sreenivasan

December 2006

## Abstract

Using frozen hydrogen particles to observe rotating and quantized flows in liquid helium

Gregory P. Bewley
2006

We present a novel technique for tracing liquid helium flows, and use this technique to make observations of fluid dynamics in both the normal fluid and the superfluid phases of liquid helium. To visualize fluid motions, we create a suspension of frozen hydrogen particles with diameters on the order of one micron. We show theoretically that the hydrogen particles we generate can be used to make quantitative measurements of local flow velocities in turbulent liquid helium, and that these particles are the only ones we know of that are suitable for this purpose. In experimental work, we use the particles in normal liquid helium to examine the effect of the Coriolis force on the decay of classical turbulence using the Particle Image Velocimetry technique (PIV). We observe grid-generated turbulence in a steadily rotating frame and find that the evolution of the flow depends intimately on boundary conditions because of the production in the fluid of standing inertial wave modes of the container. Separately, we present what are very probably the first documented images of the cores of quantized vortices residing in the superfluid phase of liquid helium. Filaments we observe in the fluid are probably formed by the particle-trapping action of the quantized vortices. Although others have speculated how particles in superfluid helium could act as passive tracers of a flow, as they do in the normal fluid, our images indicate that the presence of particles in the superfluid may transform the topology of vortex tangles by stabilizing forks in the vortices.

# Acknowledgements

I am grateful to my adviser, Katepalli Sreenivasan, for his steadfast support and guidance. I am also indebted to Dan Lathrop for accepting me in his lab and providing countless invaluable ideas. I wish to thank Rustom Bhiladvala for introducing me to science and lab work, and Chris White for initiating me in the techniques required to perform these experiments. My work would not have progressed without the engaging discussions I have had with Eric Kostelich, Narendra Kumar, Leo Maas, Joe Niemela, and Ladik Skrbek. I am especially beholden to Joe Vinen for the encouragement to experiment with superfluid helium, and to Russ Donnelly who proposed rotating the superfluid in order to confirm our observation of vortices. I also thank my committee members Ed Bolton, Marshall Long, Juan de la Mora, and Kailas Purushothaman. I greatly appreciate the assistance of Don Martin and my many inspiring lab mates both at Yale and at the University of Maryland. Finally, I would not have survived without the unreserved support of my friends and family. Thank you.

# Contents

**Acknowledgements** **i**

**Contents** **ii**

**List of figures** **viii**

**List of tables** **xviii**

**1. Introduction** **1**

1.1 Scales of turbulent motion 2

1.2 Benefits of helium as a test fluid 3

1.2.1 Classical hydrodynamics 3

1.2.2 Quantum hydrodynamics 4

1.3 Available techniques for velocity measurement 5

1.4 The difficulties of observing liquid helium flows 6

1.4.1 Small length scales 6

1.4.2 Particle suspensions 7

1.5 Summary 8

**2. Apparatus and methods** **10**

2.1 The apparatus 10

2.1.1 The cryostat 12

2.1.2 The cooling protocol 12

2.1.3 The channel 13

2.1.4 The grid 14

2.1.5 The linear motor 15

2.1.6 Air bearing 15

2.1.7 Camera 16

2.1.8 Laser and optics 17

2.2 Particle image velocimetry 18
2.2.1 Brief description 18
2.2.2 Data processing 20
2.2.3 Limitation of the PIV technique at high Reynolds numbers 21
**3. Particle selection 23**
3.1 Tracer particle fidelity 23
3.1.1 A method to evaluate a particle as a fluid tracer 23
3.1.2 Suggested alternate formulation 26
3.2 Large Froude and Stokes effects 28
3.2.1 Vibrated particles 28
3.2.2 Measurement of large scale flow properties 28
3.3 Particle clumping 30
3.3.1 Comparison of forces 31
3.3.2 Rate of coagulation 34
3.3.3 Suspension stabilization 35
3.3.4 Methods for dispersing particles 37
3.4 Evaluation of available seeding techniques 37
3.4.1 Commercially available particles – hollow glass spheres 37
3.4.2 Commercially available particles – solid beads 40
3.4.3 Commercially available particles – other types of particles 43
3.4.4 Review of previous work to make frozen particles 43
3.5 The first hydrogen injector 44
3.5.1 The basic properties of hydrogen 45
3.5.2 First attempts to make hydrogen particles 45
3.6 The improved hydrogen injector 48
3.6.1 The injector 48
3.6.2 Procedure 49
3.6.3 Results 50
3.7 Discussion 51
3.7.1 Particle volume fraction 51

3.7.2 Particle size 51
3.7.3 Model of injector function 53
3.7.4 Practical considerations 54
3.7.5 A note on the injection of particles into superfluid helium 55
3.7.6 Final analysis 55
3.8 Conclusions 57
**4. Decaying grid turbulence 58**
4.1 Background 58
4.1.1 Homogeneous and Isotropic Turbulence 58
4.1.2 Grid Turbulence 59
4.1.3 Theoretical predictions of the decay rate 60
4.1.4 Experimental observations 62
4.2 Methods 63
4.2.1 Protocol 63
4.2.2 Image timing 64
4.3 PIV measurements using hydrogen particles 65
4.3.1 PIV Data 66
4.3.2 Mean Flow 66
4.3.3 Turbulent energy decay 70
4.3.4 The strength of the mean flow 71
4.3.5 A comment on the magnitude of the observed variables 72
4.3.6 A note on thermal input 73
4.4 Conclusions 74
**5. Turbulence in a rotating container 75**
5.1 Rotating flows 75
5.1.1 The Coriolis acceleration and its effects 76
5.1.2 The parameter space investigated 78
5.1.3 Two-dimensional flows 78
5.1.4 Inertial waves 79
5.1.5 Inertial wave modes of a container 80

5.1.6 Reflecting inertial waves 81
5.1.7 Rotating, decaying homogeneous turbulence 82
5.2 Previous experimental work 82
5.3 Apparatus and methods 85
5.3.1 Experimental protocol for the cryogenic fluids 86
5.3.2 Spinup of the fluid 86
5.3.3 Liquid nitrogen 87
5.3.4 Water channel 88
5.4 Results 90
5.4.1 The energy decay 90
5.4.2 The mean flow 90
5.4.3 Transform of the mean flow 92
5.4.4 The circular apparatus 94
5.4.5 Revisiting the square channel data 96
5.4.6 The square channel with liquid helium 98
5.5 Discussion 100
5.5.1 The modes in liquid helium 100
5.5.2 The right experiment 100
5.5.3 The source of energy for the large scales 102
5.5.4 The parameter *J* 102
5.5.5 Why the modes have not been previously observed in this context 103
5.5.6 A note on the decay rate 104
5.6 Conclusions 104
**6. Visualizing quantized vortex lines 105**
6.1 Background 105
6.1.1 Basic physical properties of liquid helium 106
6.1.2 Quantized vortices 108
6.1.3 Quantization and the evolution of vortices 110
6.1.4 The two-fluid model 112
6.1.5 Residual vortices 114

6.1.6 A rotating superfluid 115
6.1.7 Flows in He II 116
6.1.8 Previous experimental observations 117
6.2 Methods 119
6.2.1 The formation of a superfluid 119
6.2.2 Preparation of the particle suspension in He II 120
6.2.3 Gathering data near the transition temperature 121
6.2.4 Gathering data in the rotating frame 122
6.3 Results 125
6.3.1 The filaments 125
6.3.2 Review of the assumptions 128
6.3.3 Evenly spaced particles 131
6.4 Discussion 133
6.4.1 A particle trapping mechanism 134
6.4.2 Trapping time and particle size 136
6.4.3 The driving force for the formation of vortex filaments 138
6.4.4 Limitations of the observation 139
6.4.5 The significance of branches 142
6.4.6 The dotted lines 143
6.5 Conclusions 144
**7. Conclusions and future work 145**
7.1 Improvements to the apparatus 146
7.1.1 Heat input 146
7.1.2 Controlling experimental conditions 147
7.1.3 An additional window 148
7.1.4 Particle tracking 149
7.2 Particle characterization 149
7.3 Classical turbulence 150
7.3.1 Decaying turbulence in a non-rotating frame of reference 150
7.3.2 Rotating turbulence 150

7.4 Experiments in He II 151
7.4.1 Quenches through transition 152
7.4.2 Dotted lines 154
7.4.3 Tkachenko waves 154
7.4.4 Laser tweezers – plucking a quantized vortex 155
7.4.5 The wanderers 155
7.4.6 Branching and networks 155
7.4.7 Onset of turbulence 156
7.5 Closing remarks 158
**Bibliography**

# List of figures

1.1: Viscosity and density for various fluids. All properties are given at atmospheric pressure. The properties of air are given at room temperature. For liquid nitrogen and liquid helium, they are given at their boiling points, 77 K and 4.2 K, respectively. 4

2.1: A picture of the apparatus showing the cryostat that rotates about the vertical axis on an air bearing, along with the camera and associated electronic equipment. Also shown are the linear motor that draws a grid through the channel inside the cryostat, and the optics used to illuminate particles suspended in the fluid. The cryostat is about one meter tall. 11

2.2: The drawing shows the interior of the cryostat. At the core is the 5 cm square channel through which we draw a grid. The main helium reservoir above it, as well as the annular liquid nitrogen jacket and outer wall of the cryostat each have circular cross sections. Between each concentric vessel is a common vacuum space. 13

2.3: An illustration of the grid shows its mesh spacing, $M$, and the grid stem by which it is pulled through the channel. 14

2.4: The line traces the path of the laser beam, the circles represent mirrors. All fixtures below the air bearing are fixed to an optical table; everything above the air bearing rotates together, including the beam when it is carefully aligned with the axis of rotation. 18

2.5: Examples of two images taken at successive times are shown at the top left. Small regions are taken from the images, called interrogation areas. The

cross-correlation of the interrogation areas is computed, shown in the top right. The location of the peak gives the relative offset, $\Delta x$, of the particles between the two interrogation areas. A vector is assigned to the center of the interrogation area, whose magnitude and direction are given by $\Delta x/\Delta t$. This calculation is repeated for a chosen set of pairs of interrogation areas in the two images. 19

3.1: The van der Waals potential as a function of sphere separation is the dashed line. We use Hamaker's constant for polystyrene, $A = 8 \times 10^{-20}$ J, but the Hamaker constant for most materials is of the same order. An exception is liquid helium, and since Hamaker's constant for liquid helium is much smaller (Paalanen and Iye 1985), we do not need to account for it as the intervening fluid (Heimenz and Rajagoplan 1997). 31

3.2: The ratio of the attractive van der Waals force to the fluid shear induced separation force for polystyrene spheres in a turbulent flow at $Re_\lambda = 400$. The ratio is given as a function of the sphere's radius for several surface separations. The surface separation is expressed as a fraction of the sphere radius, imagining that some surface roughness keeps the spheres further apart than if they were perfect spheres. For particles smaller than a few microns, the van der Waals force is much larger than our estimated upper bound for the separation force. 34

3.3: An image of a suspension of hollow glass spheres in liquid helium. 38

3.4: The chart shows the Stokes and Froude numbers as they evolve in a turbulent flow generated by a grid with 7.2 mm mesh spacing, $M$, drawn at $U = 2.0$ m/s in liquid helium. The parameters are calculated for a 9 μm hollow glass sphere. The horizontal line is the maximum value for either parameter determined in section 3.2, and that either one parameter or the other is larger at any moment indicates that the particle does not trace fluid motions accurately. 40

3.5: On the left are clumps of 2 μm polystyrene particles in liquid helium. On the right are identical particles in water, using a surfactant to disperse them. 41

3.6: The chart shows the Stokes and Froude numbers as they evolve in a turbulent flow generated by a grid with 7.2 mm mesh spacing, $M$, drawn at $U$ = 2.0 m/s in liquid helium. The parameters are calculated for a clump of polystyrene particles with a characteristic diameter of 2.4 μm. The horizontal line is the maximum value for either parameter determined in section 3.2, and that either one parameter or both is larger at any moment indicates that the particle clump does not trace fluid motions accurately. 42

3.7: The liquid hydrogen injector consists of concentric stainless steel tubes that are kept from touching each other with Teflon spacers every 6 cm. A vacuum develops between them when the injector is cooled. Hydrogen gas is introduced at the top. A wire along the length of the core and a wire wrapped around the nozzle can separately be heated to keep the interior of the injector above the freezing point of hydrogen. 46

3.8: On the left is a liquid hydrogen jet in liquid helium. On the right are the resultant solid hydrogen "snow flakes." 47

3.9: The schematic shows the design of our diluted hydrogen injector. Hydrogen gas diluted with helium is introduced at the top, and enters the cryostat through the inner of two concentric stainless steel tubes. The mixture cools on passage through the injector and exits below the free surface of liquid helium. 49

3.10: Hydrogen particles generated by diluting hydrogen gas with helium in a 1 : 10 ratio are shown. The particle size distribution appears polydisperse, but overall the particles appear smaller and more numerous than those shown in figures 3.3, 3.5, and 3.8. 50

3.11: The chart shows the Stokes and Froude numbers as they evolve in a turbulent flow generated by a grid with 7.2 mm mesh spacing, $M$, drawn at

$U$ = 2.0 m/s in liquid helium. The parameters are calculated for hydrogen particles with a characteristic diameter of 3 μm. The horizontal line is the maximum value for either parameter determined in section 3.2; note that the scale in this chart is different than in the comparable figures 3.3 and 3.6. In this example, the hydrogen particles are suitable for making quantitative measurements of local fluid velocities in the turbulent flow. 52

4.1: Images are taken at each tick mark. Each set of five ticks is called a packet, and the image frames are equispaced in time within each packet. We program the time between frames within each packet, and the time between packets, to grow larger as the turbulent velocities decay, such that the particles move a constant distance between images in a packet. 64

4.2: PIV vectors computed from two images taken 1 ms apart about 140 ms after the grid has passed the field of view at 1.0 m/s. Processing on images of hydrogen particles is done according to the description in section 2.2, with an interrogation area size of 24 × 24 pixels in the final pass. 65

4.3: A cross section of the channel, and a sketch of the large scale flow the grid generates as it is towed along the length of the channel. In the area we observe through the window, the flow appears uniform, though it must recirculate down the sides of the channel. 67

4.4: A sketch of one of four flush-fitting windows in the side walls of the channel. The fine line traces the outline of the original flat windows. The grid passes on the right in this drawing, and the vacuum space is on the left. The vacuum seal is formed by crushing an indium wire between the window and the channel wall. 68

4.5: The mean flow as a fraction of the grid velocity, $U_g$, using liquid nitrogen in the channel, and using different grid designs. The solid lines are the for the grid in its original configuration, drawn from its center by a rod, the dashed lines are for the grid drawn from its corners, and the dotted lines

are for the original configuration, but with flush fitting windows. The strength of the currents is comparable despite the modifications. 69

4.6: The streamwise mean flow with a 0.33 mm wire around the perimeter of the grid, in both liquid nitrogen and helium. The transverse mean flow remains largely unchanged, is always smaller than 1% of the grid velocity, and is not shown. 70

4.7: The decay of kinetic energy per unit mass in the flow generated by a grid passing through liquid helium as a function of time since the grid has passed. Variables are normalized by the grid parameters, the grid velocity, $U_g$ = 1.0 m/s, and the mesh spacing, $M$ = 7.2 mm. 71

4.8: The fluctuating energy relative to the energy in the mean for the same flow as in figure 4.7. The streamwise fluctuations are compared to the streamwise mean, and the transverse fluctuations are compared to the transverse mean. 72

5.1: The Reynolds-Rossby number parameter plane using the large scales of the flow, such that $Ro = u/\Omega L$, and $Re = uL/\nu$, showing the limits in each parameter we can achieve simultaneously using our apparatus. Here, the variable $u$ is the root-mean-square flow velocity, and $L$ is the characteristic size of the energy-containing scales, which (for convenience) we take to be the mesh spacing of the grid, $M$. The bold lines are trajectories taken from data presented in this chapter, but any combination of larger Rossby number and smaller Reynolds number can be achieved by choosing appropriate initial conditions. 77

5.2: The circular cylindrical channel is put in place of the cryostat and is filled with water. The position of the false ceiling is adjustable. The indicated window faces the camera, while the laser passes through the curved wall of the channel. 88

5.3: The crosses are the decay of kinetic energy in a channel rotating at about 1 Hz filled with liquid nitrogen, after being agitated with a grid. The solid

line is from data acquired in the same way, but without system rotation, at a mesh Reynolds number of 72,000. In the stationary case, the decay of kinetic energy is slightly steeper than $t^{-1}$, which is expected of a lower Reynolds number flow, as described in chapter 4. The decay with rotation shows strong fluctuations in time. 91

5.4: The mean flow for the same data as in figure 5.3. Streamwise flows are in the direction of grid motion. 91

5.5: The mean flow shown in figure 5.4 relative to the stochastic fluctuations in the local velocity. The solid line is the streamwise velocity component; the dashed line is the transverse component. The oscillations are of comparable magnitude to the fluctuations throughout the decay. 92

5.6: The transform of the repeatable mean flow shown in figure 5.4, generated by a grid drawn through liquid nitrogen in a square channel rotating at $\Omega = 0.98$ Hz. The energy in each transform lies predominantly below a frequency that is twice the system rotation rate, as must be the case for inertial waves. 93

5.7: The mean flow in the water channel for $h = 80$ cm, comparable to figure 5.4 of the same measurement, but using liquid nitrogen in a square channel. 94

5.8: The transform of the streamwise, or axial, mean flow shown in figure 5.7. The vertical lines are the locations of inertial wave modes predicted by Kelvin's linear, inviscid theory given in section 5.1.4. 95

5.9: We plot as circles the frequencies of the dominant peaks in spectra, such as the one in figure 5.8, for a series of aspect ratios, $h/b$, where $h$ is the length of the channel along the axis of rotation, and $b$ is its radius. The curves are calculated according to (5.1.8) for different combinations of axial and transverse wavenumbers. 96

5.10: The frequency spectrum of velocity fluctuations in a rotating square channel filled with liquid nitrogen. The vertical lines are predictions made

by Maas (2005), whose [axial, transverse] wavenumbers are given in the order of increasing frequency. Most of the peaks correspond to successively higher axial wavenumbers. 97

5.11: The decay of energy in liquid helium with and without rotation. The solid curve is from figure 4.6, for a mesh Reynolds number of 283,000. The crosses trace a curve similar to that observed in liquid nitrogen in figure 5.3. 98

5.12: The mean flow in liquid helium, relative to the fluctuations. The solid line is the streamwise velocity component; the dashed line is the transverse component. The oscillations are of comparable magnitude to the fluctuations throughout the decay. 99

5.13: The solid curve is the transform of the streamwise mean flow in liquid helium. It shows well defined peaks, all lying below twice the rotation rate. We show the data from figure 5.6 using liquid nitrogen as a dashed curve. The peaks of the two curves coincide at high frequencies, but not below $\omega/2\Omega \approx 0.4$. We indicate the frequencies of some high axial wavenumber inertial wave modes as suggestions, but there are many other modes with frequencies that do not lie near peaks. 99

6.1: Phase diagram for helium near the lambda point, from Donnelly (1967). 107

6.2: The specific heat of liquid helium as a function of temperature at the saturated vapor pressure, from data collected by Donnelly and Barenghi (1998). 107

6.3: The two curves shown are the densities of the normal fluid and superfluid in the two fluid model of He II, at its saturated vapor pressure. The densities sum to the whole fluid's density, which is almost constant as a function of temperature and nearly equals 0.14 g/cc. At the lambda point, He II is entirely accounted for by the normal fluid part. At absolute zero, He II is a pure superfluid. 114

6.4: Data taken from Yarmchuk et al. (1979) is shown. The spots are the intersections of quantized vortices in a steadily rotating bucket where they intersect with the free surface. The rotation rate of the bucket generally increases from the left to the right in the sequence of images, as they are oriented here. 118

6.5: The time line of an experiment is portrayed in the figure. The relative times, temperatures, and the slopes of the curve are consistent with a typical experiment, though the temperature can be allowed to fall significantly further by leaving open the vacuum pumping valve for longer than indicated. 120

6.6: The times and temperatures for images taken during four selected, but typical, trials. The curves can be compared to the one in figure 6.5. We estimate the net cooling rate as 350 mW from the slope of the curves and the volume of liquid helium. Using this cooling rate, we integrate the heat capacity in figure 6.2 to produce the solid curve shown. The offset of this curve from the data can be attributed to systematic error in the thermometer. However, the origin of the differences of shape of the curves is unknown, and may be due to overturning of the fluid as its density changes near the lambda point. 122

6.7: Panel (a) shows a suspension of hydrogen particles just above the transition temperature. Panels (b), (c), and (d) show similar hydrogen particles after the fluid is cooled below the lambda point. Some particles have collected along branching filaments, while other are randomly distributed as before. Fewer free particles are apparent in (b), (c), and (d) only because the light intensity is reduced to highlight the brighter filaments in the image. The nature of the branching filaments is discussed in section 6.4. 124

6.8: The picture shows an example of particles arranged along vertical lines. The system rotation axis is vertical. On the left is the original, and on the right is an enhanced and inverted version. The spacing of lines is remarkably

uniform, although there are occasional distortions of the lattice and possible points of intersection. 126

6.9: The axis of rotation is normal to the page. We assume a triangular array of vortices; their intersections with the horizontal plane are indicated by dots. The light sheet also intersects the page, and its cross section is represented by the dashed lines at the orientation relative to the lattice assumed in our calculation of line density. 127

6.10: We compute the density of lines made visible by particles as in figure 6.8, according (6.3.1) and the assumptions discussed in the text. The error bars are the standard deviation of all the measurements made at each rotation rate. Feynman's rule is given by (6.1.14), and the significance of the dashed line is described in section 6.3.2. 128

6.11: As in figure 6.9, we show the intersection of vortices with the horizontal plane as spots. However, consider a light sheet orientation different from the simplest one that illuminates a different line spacing than the minimum lattice spacing. 130

6.12: A series of images of particles regularly spaced along lines, taken during three independent excursions below the phase transition temperature by steadily cooling the fluid. In (a), the temperature is 32 mK below the lambda point, and about 350 s have passed since attaining the transition temperature. In (b), the temperature is 25 mK below the lambda point, and about 300 s have elapsed. In (c), the temperature is 28 mK below the lambda point, and about 400 s have elapsed. Temperatures are accurate to within 5 mK, and times within 40 s. Dotted lines such as these were not observed before or after the stated times, or at other temperatures. 132

6.13: The circles show the mean of histograms of particle spacings along dotted lines, where the histogram for each line is normalized by the mean spacing along that line. The solid line is the distribution of mean spacings among the different dotted lines normalized by the overall mean spacing. The

spacing along a particular line is seen to have a narrower distribution than the difference in spacings between different lines. 133

6.14: The chart shows the ratio of the total drag on a vortex due to mutual friction to the drag caused by the presence of particles trapped on the line. We include a factor $\sigma$, describing the spacing of the particles. For $\sigma = 1$, the particles are next to each other, for $\sigma = 10$, they are 10 diameters apart. Particle drag is always stronger than mutual friction if the particles entirely cover the line. 141

7.1: The panels show the coarsening of a hydrogen particle suspension in liquid helium as the fluid is cooled through the superfluid phase transition. In (a), the temperature is 2.173 K, in (b) it is 2.170 K, in (c) it is 2.167 K, and in (d) it is 2.163 K. 153

7.2: These images were taken while superfluid liquid helium had reached a state of steady rotation about the vertical axis, under similar conditions as figure 6.8. It is likely, however, that the presence of a higher concentration of particles has caused the lattice of quantized vortices to pinch together in places. 156

# List of tables

3.1: We list the B numbers, defined in section 3.1.2, for a variety of particles in liquid helium near its boiling point. Particles that satisfy our condition that B > 1 are marked by a bold font. The 4 μm hollow glass particles are hypothetical – we do not know of any that are manufactured. As discussed in the text, it is unlikely that polystyrene particles can be suspended as individual particles, since they have a strong tendency to aggregate into larger clumps. Therefore, the hydrogen particles are the only particles we know of that we can use to accurately trace the motions of liquid helium. 56

5.1: Numerical results from Maas (2005) for the modes in a square channel with aspect ratio $h/2b = 5$. The numbers are the frequencies of the modes relative to the inertial frequency, or $\omega_M/2\Omega$. The first pair of rows is the symmetric and asymmetric modes, as defined by Maas (2003), with varying axial wavenumber, and transverse wavenumber equal to one. The second pair of rows is for modes with the same axial wavenumbers and a transverse wavenumber of two. 81

# Chapter 1

# Introduction

A common objective unites the results presented in this dissertation: to make quantitative measurements of local flow velocities in liquid helium. Liquid helium is an interesting test fluid for at least two reasons. First, its viscosity is the smallest of all fluids, and second, it undergoes a phase transition to a superfluid state as it is cooled to very low temperatures. As is well known, however, the material properties of liquid helium present challenges to the realization our objective. In this chapter, we introduce the motivations for our experiments and the fundamental problems surmounted.

We present a novel technique for tracing liquid helium flows, and use this technique to make observations of fluid dynamics in both the normal fluid and the superfluid phases of liquid helium. To visualize fluid motions, we create a suspension of frozen hydrogen particles with diameters of the order of one micron. Using these particles, we measure the decay rate of grid-generated turbulence at a higher Reynolds number than those reported earlier. We also present what are very probably the first documented images of the cores of quantized vortices residing in the superfluid phase of liquid helium. Filaments we observe in the fluid are probably formed by the particle-trapping action of the quantized vortices.

Another uniting theme in this work is system rotation, which we use to observe the effect of the Coriolis force on the decay of classical turbulence, as well as to establish an interpretation of the particle-decorated filaments as quantized vortices in the superfluid phase of liquid helium. In normal liquid helium, we observe grid-generated turbulence and find that container-sized scales of motion affect the evolution of both stationary and rotating turbulence, although such large scales are often ignored in experimental studies. In particular, in a steadily rotating frame of reference we conclude that the evolution of the flow depends intimately on boundary conditions. These results preclude experimental verification of general statements about homogeneous rotating turbulence.

## 1.1 Scales of turbulent motion

We approach our investigation from the perspective of classical turbulence. The momentum equation governing the motions of a Newtonian fluid may be written as

$$\partial \boldsymbol{u}/\partial t + \boldsymbol{u}\cdot\nabla\boldsymbol{u} = -\nabla P + \nabla^2\boldsymbol{u} / Re, \tag{1.1.1}$$

where $\boldsymbol{u} = \boldsymbol{u}(\boldsymbol{x}, t)$ is the velocity field, which is a function of time, $t$, and space, $\boldsymbol{x}$, and $P$ is the pressure. Combinations of $U$ and $L$, the velocity and length scales characteristic of the flow, normalize all variables which results in the appearance in the equation of

$$Re = UL/\nu, \tag{1.1.2}$$

the Reynolds number, where $\nu$ is the fluid's kinematic viscosity. Equation (1.1.1) is the Navier-Stokes equation, which, in conjunction with a statement about the conservation of mass, $\nabla\cdot\boldsymbol{u} = 0$, fully specifies the evolution of incompressible fluid motions, subject to the appropriate initial and boundary conditions.

Turbulence is often viewed as a collection of superimposed unsteady fluid motions occurring on a wide range of length scales (Frisch 1995). The largest scales are shaped by the forcing mechanism of turbulence; it is at these scales that kinetic energy is typically 'injected' into fluid motions. The largest scales are thought to evolve as in an inviscid fluid, and break up into successively smaller scales. The process continues until the action of viscosity on a motion of a particular scale becomes significant, and energy is removed from the flow as heat. By assuming that the behavior of the smallest scales are governed entirely by viscosity and the rate of energy dissipation, $\varepsilon = -dE/dt$, of the flow's average kinetic energy per unit mass, $E$, Kolmogorov (1941) arrived at a measure of the smallest scales of motion:

$$\eta = \nu^{3/4}/\varepsilon^{1/4}. \tag{1.1.3}$$

The Reynolds number, in this context, gauges the separation of the large and small scales, and governs the extent to which different length scale regimes of the flow can be considered statistically independent. Frisch (1995) gives a more detailed introduction.

## 1.2 Benefits of helium as a test fluid

### 1.2.1 Classical hydrodynamics

There is interest in data acquired at high Reynolds numbers, as it is only in this regime that certain statistics of the flow are expected to exhibit predictable scaling. The argument for using liquid helium in experimental studies of fluid dynamics centers on its low kinematic viscosity, which is 40 times lower than that of water at room temperature, and lower than that of any other known fluid. The properties of liquid helium are compared to common fluids in figure 1.1. As can be judged from equation (1.1.2),

helium's low viscosity enables flows with large Reynolds numbers to be generated on physical scales more easily realizable in the laboratory. This property, along with others such as the large thermal expansion coefficient of cold gaseous helium, has led several research groups to pursue fluid dynamics experiments using helium (Skrbek et al. 1999, Sreenivasan and Donnelly 2001, Skrbek 2004, Niemela and Sreenivasan 2006).

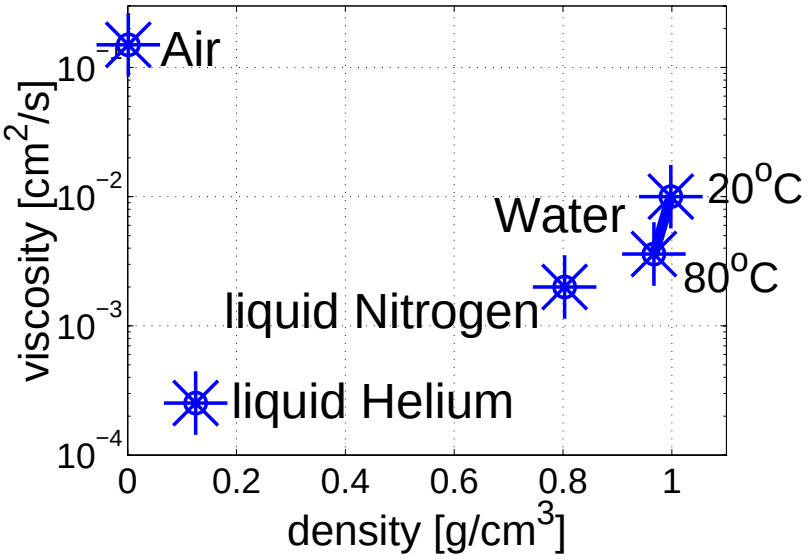


**Figure 1.1**: Viscosity and density for various fluids. All properties are given at atmospheric pressure. The properties of air are given at room temperature. For liquid nitrogen and liquid helium, they are given at their boiling points, 77 K and 4.2 K, respectively.

### 1.2.2 Quantum hydrodynamics

Liquid helium undergoes a phase transition to a state exhibiting properties characteristic of a superfluid, as it is cooled below 2.177 K. Using liquid helium, we may study behavior governed by quantum mechanics exhibited on a macroscopic scale. In particular, there exist vortices with quantized circulation and a core diameter of the order of an angstrom, extending in length for many millimeters (Donnelly 1967).

Since the discovery of quantized vortices 50 years ago, scientists have prodded the coldest phase of liquid helium knowing that it contains distinct and enduring structures whose geometry they could only imagine. No one has succeeded in visualizing the three-dimensional shape of quantized vortices. It is a remarkable testament to the ingenuity of low temperature scientists that so much has been learned about quantum hydrodynamics without the flow visualizations and velocity measurement techniques that are routine in classical hydrodynamics.

Quantized vortices are a close approximation to ideal line vortices, and a turbulent state of vortices has been studied analytically and numerically as such a system (e.g., Schwartz 1988). Recently, however, it has been recognized that turbulence in superfluid helium appears on the large scale very much like classical turbulence, with the same scalings in frequency spectra and the same energy decay law (Maurer and Tabeling 1998 and Smith et al. 1993).

## 1.3 Available techniques for velocity measurement

Direct observations of fluid dynamics in liquid helium are scarce because, aside from the technical difficulty of working at low temperatures, there are only a limited number of available measurement techniques. Several research groups are adapting techniques used in common fluids to cryogenic ones. These efforts include the adaptation of particle image velocimetry (PIV) by White et al. (2002) and Zhang and Van Sciver (2005), laser Doppler velocimetry (LDV) by Nakano and Murakami (1992), and hot wires by Castaing et al. (1992). An additional technique called particle tracking is a promising alternative to PIV, although it has not been implemented in cryogenic fluids

(see Voth et al. 2002 who used it to measure the accelerations of particles in water). Adapting each of the tools poses a technical challenge, primarily because the use of cryogenic fluids requires great improvement in the spatial resolution of the probe.

Following the example of our predecessor (White 2001), we pursue the development of PIV as a tool for observing the motions of liquid helium. PIV allows large amounts of data to be gathered quickly and yields direct information about spatial structure that cannot be attained by other techniques. PIV requires that a suitable passive tracer particle be found, which would also be useful for LDV or particle tracking.

## 1.4 The difficulties of observing liquid helium flows

### 1.4.1 Small length scales

The same property, low viscosity, which makes liquid helium valuable for generating a high Reynolds number flow also makes the observation of its fluid motions difficult. Increasing the Reynolds number of a flow without increasing its overall size forces the small scales to shrink. The statement can be clarified by expanding in (1.1.3) the dissipation, $\varepsilon$. By dimensional arguments, dissipation is proportional to $U^3/L$ at large Reynolds numbers, where $L$ is a characteristic measure of the large scales, and is therefore independent of viscosity (e.g., Sreenivasan 1984). It is then seen that the small scale given by (1.1.3), and usually referred to as the Kolmogorov scale,

$$\eta = \nu^{3/4}/\varepsilon^{1/4} \sim (\nu^3 L/U^3)^{1/4}, \tag{1.4.1}$$

shrinks with decreasing viscosity and with increasing $U$, for fixed $L$. In order to resolve all scales of motion, our measurement probe must correspondingly shrink in size. For

conditions typical in our apparatus, flow velocities are about 2 cm/s and the length scale, $L$, is about 0.5 cm, so that the Kolmogorov scale, $\eta$, is about 10 μm.

### 1.4.2 Particle suspensions

PIV is typically used to infer the velocity of a fluid from the motion of particles, in which case we require that the velocity of the particle be close to the local fluid velocity in the absence of the particle. For making velocity measurements of the more common fluids, water and air, the choice of tracer particle is most frequently limited by imaging requirements. The particle must be large enough that it can be imaged with the available illumination and detection equipment. In cryogenic fluids such as liquid helium, there are at least three additional complications.

First, the low viscosity of liquid helium demands that we be careful when considering the fidelity with which the particle follows the fluid motions. In order for a particle successfully to trace the fluid, the size of the particle must be small, as already hinted in the previous section. In fact, for solid particles made of readily available materials, the required particle size approaches the wavelength of visible light (about 0.5 μm). Such small particles are difficult to detect optically, since the light scattered by a particle diminishes dramatically with its size (Mie scattering).

Second, the low density of liquid helium, which at its boiling point is one eighth that of water, compounds the problem of small viscosity. This is because almost all solid materials known to us are significantly denser than liquid helium; many of the materials commonly considered less dense are porous, and it is difficult to manufacture very small particles that are porous. A particle made of a dense material will sink. In many cases,

this settling velocity is higher than it would be in air, despite the lower density of air. We use hydrogen to make particles because the density of its solid, 0.088 g/cc, is within 50% of the density of liquid helium.

Finally, we shall see that because liquid helium is non-polar and below the glass transition temperature of polymers, the usual methods of overcoming the mutual attraction of particles fail. In water, researchers use surfactants to disperse particles, but none exist for liquid helium. The particles inevitably form clusters that are too large to trace the flow accurately. Our small hydrogen particles, however, permit us a window in time during which aggregation has not progressed to an unacceptable level.

## 1.5 Summary

The problem of demonstrating the feasibility of PIV in liquid helium lies primarily in the manufacture of suitable particles. Although our predecessors have made progress, the need remains to develop a satisfactory tracer particle. We mean this in the sense that further work is necessary in order that the measurement of particle velocities in liquid helium can be used to answer basic questions about turbulence dynamics. We have found a solution by generating small frozen hydrogen particles.

After the description of the experimental apparatus in chapter 2, the rest of the thesis is divided into four parts. In chapter 3, we establish the need for new tracer particles and describe our technique for generating them. In chapter 4, we show that measurements of particle velocities produce results generally consistent with expectations for decaying grid turbulence. In chapter 5, we introduce rotating flows and the previous experimental efforts to observe rotating homogeneous turbulence. We use the hydrogen

particles and PIV to demonstrate the presence of standing inertial waves whose frequencies are determined by the geometry of the container. Finally, in chapter 6, we introduce superfluidity and present pictures of thin filaments that we argue are the first-ever outlines of quantized vortex cores in a three-dimensional and random environment.

# Chapter 2

# Apparatus and methods

We now describe the apparatus common to all the investigations presented in this thesis, and offer an introduction to PIV. Our apparatus allows the generation of intense turbulence and rapid rotation simultaneously. The outside radius of the vessel containing the fluid is no more than 15 cm, yet we are able to generate flows with Reynolds numbers approaching the highest ones observed using a grid in an inertial frame. The small size enables easy mechanical rotation so that the Rossby number (non-dimensional inverse rotation rate) can be quite small. Much of the data we collect from the flows we generate is processed using PIV. Other methods and further details specific to particular experiments are described in their respective chapters.

## 2.1 The apparatus

The cryostat, grid, and linear motor actuator are largely the same as used by White et al. (2002), and are described in White's thesis (2001). We review these systems, as well as an air bearing, camera, laser and optics installed for the current investigations.

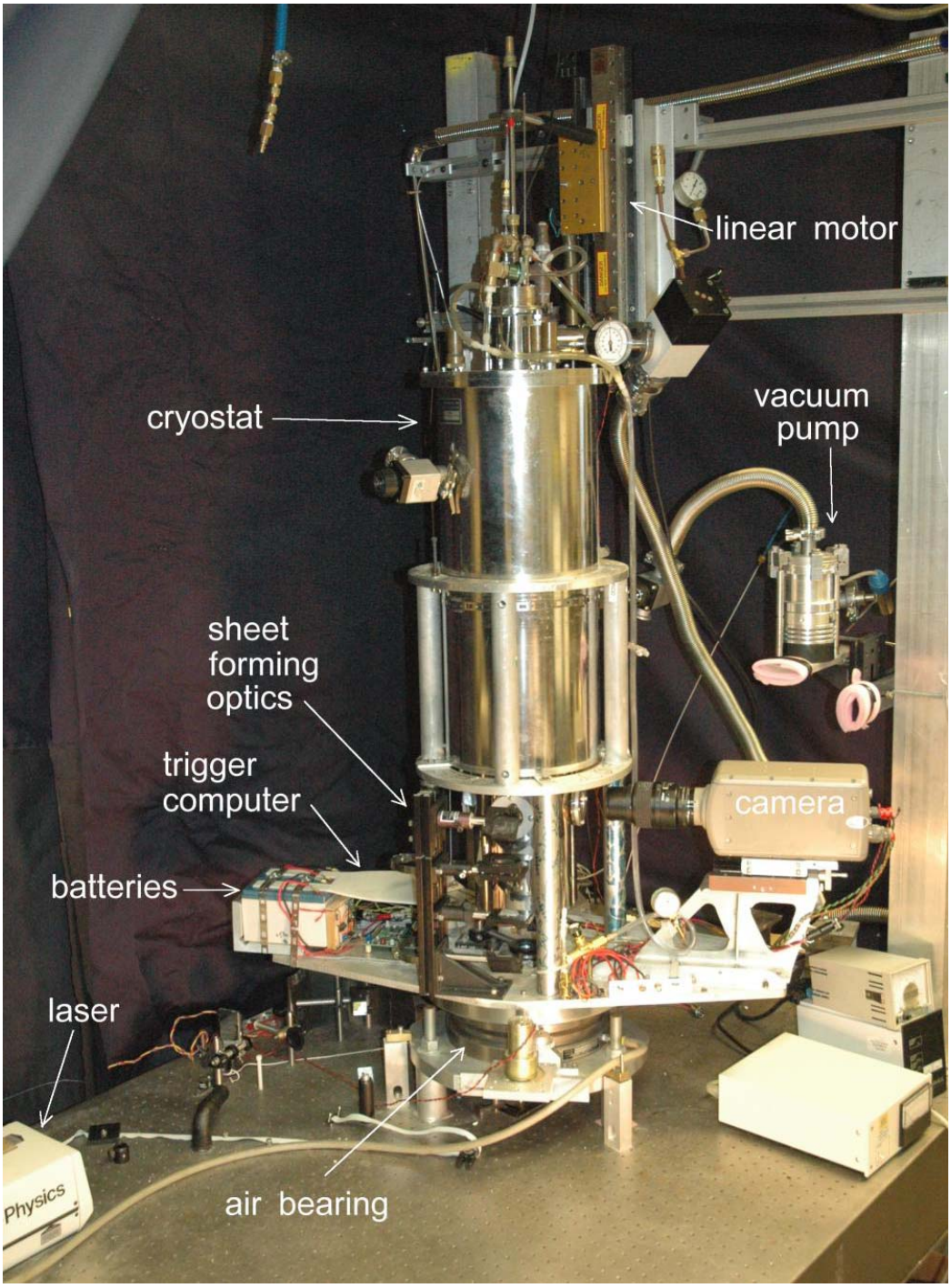


**Figure 2.1**: A picture of the apparatus showing the cryostat that rotates about the vertical axis on an air bearing, along with the camera and associated electronic equipment. Also shown are the linear motor that draws a grid through the channel inside the cryostat, and the optics used to illuminate particles suspended in the fluid. The cryostat is about one meter tall.

### 2.1.1 The cryostat

At the center of the experimental apparatus is a cryostat designed to hold liquid helium in a cell that can be accessed optically. The liquid helium can be maintained at pressures from slightly above atmospheric to vacuum and at temperatures from 4.2 K down to around 1.5 K. The cryostat, whose vertical cross section is shown in figure 2.2, is modified from a standard Janis product. The Janis cryostat has a 6 L reservoir at its core, and is jacketed by a 7 L annular reservoir for holding liquid nitrogen. The inner-most helium reservoir and the liquid nitrogen jacket are not mechanically joined, except where each is fixed along its upper perimeter to the top plate of the cryostat. The vessels are suspended in a vacuum of about $10^{-5}$ Torr, in order to minimize heat transfer from the lab. The vacuum is thought substantially to improve with the introduction of liquid helium to the cryostat, by the action of cryo-pumping (O'Hanlon 2003).

### 2.1.2 The cooling protocol

In order to perform an experiment, the vacuum jacket is first evacuated for up to a week using a mechanical vane-type pump and a turbo pump in series. Concurrently, the helium reservoir of the cryostat is evacuated using a separate pump, and refilled with helium gas. The process of evacuating and flushing the central reservoir is repeated several times to ensure that foreign gases will not condense and obscure the optical windows upon cooling of the cryostat. Subsequently, the nitrogen jacket is filled with liquid nitrogen from a storage Dewar. The helium reservoir cools for 24 hours through the vacuum space separating it from the liquid nitrogen jacket, and is supplied with helium gas to replenish the contracting gas. Using liquid nitrogen in this way to cool the

cryostat conserves liquid helium, which is much more expensive. Pumping of the cryostat's vacuum jacket may continue until the cryostat is cooled with liquid helium, then the insulating vacuum space must be sealed. Finally, liquid helium is introduced into the central reservoir from a storage Dewar. The process of cooling the cryostat to liquid helium temperature expends about 20 L of liquid. An additional 10 L are consumed each day to replenish the reservoir. The cryostat may also be used with liquid nitrogen at its core. In this case, liquid nitrogen is poured directly into the central reservoir, instead of liquid helium, all other steps being performed in the same manner.

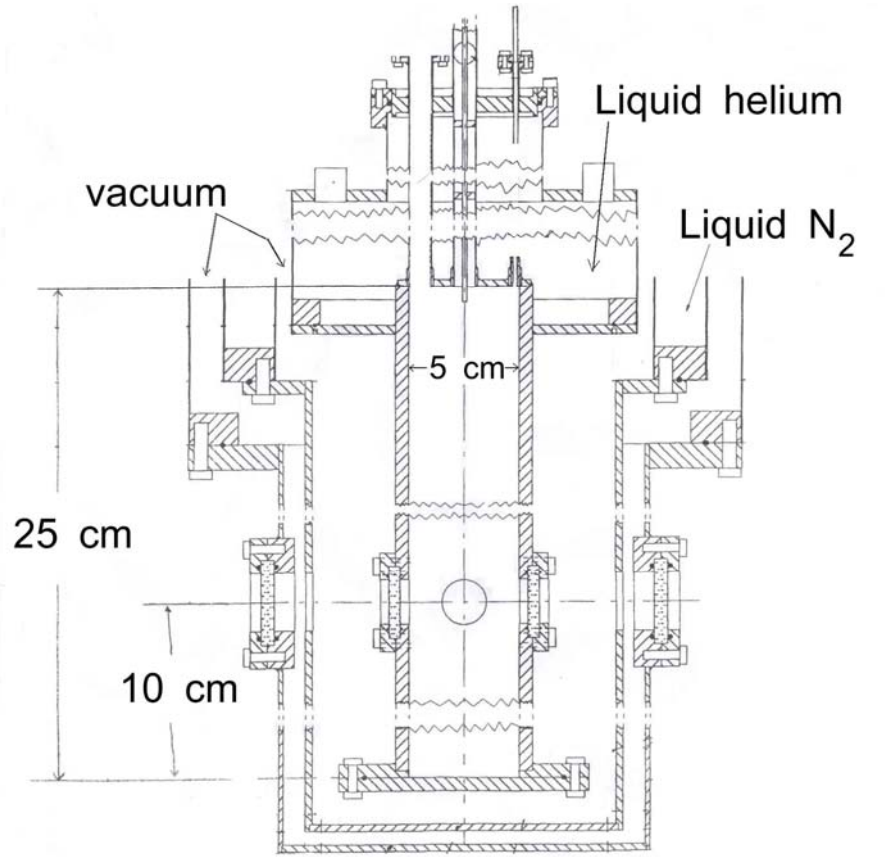


**Figure 2.2**: The drawing shows the interior of the cryostat. At the core is the 5 cm square channel through which we draw a grid. The main helium reservoir above it, as well as the annular liquid nitrogen jacket and outer wall of the cryostat each have circular horizontal cross sections. Between each concentric vessel is a common vacuum space.

### 2.1.3 The channel

To the bottom of the helium reservoir is fixed a custom sample cell that was designed by Joe Vinen and Joe Niemela and built by Steve Predko at the University of Oregon for studying grid-generated turbulence. As shown in figure 2.2, the cryostat is fitted at its core with a 25 cm long channel with a 5 cm by 5 cm square cross section. This channel communicates with the main liquid reservoir through a 1.5 mm tube, which allows it to remain full of liquid, as long as the reservoir liquid level is high enough. Windows on each face, 10 cm from the bottom of the channel, have an optical aperture of 2.5 cm. To generate turbulence, a grid is drawn along the length of the channel by means of a long stem exiting to the lab. Two additional long tubes, parallel to the one containing the grid stem, provide access to the experimental chamber.

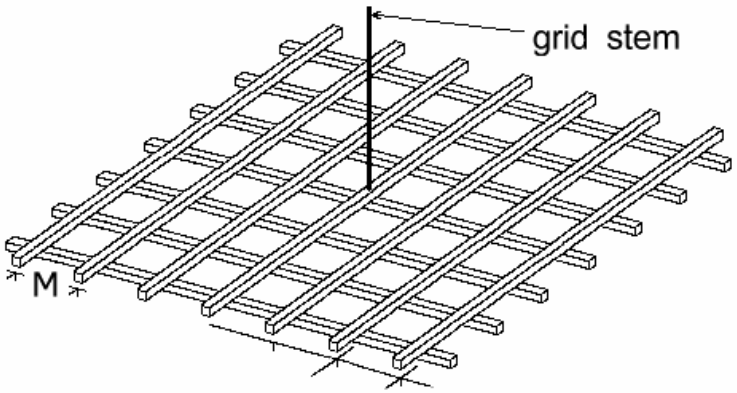


**Figure 2.3**: An illustration of the grid shows its mesh spacing, *M*, and the grid stem by which it is pulled through the channel.

### 2.1.4 The grid

The grid we used for the bulk of our experiments is made of bars with square cross section. The grid is of biplane construction with orthogonal sets of bars lying on

top of each other in two layers. The spacing between the centerlines of bars, $M$, is 7.15 mm. The width of the bars is such that the solidity of the grid, or the ratio of area occluded by the grid to the total cross sectional area of the channel, is 0.37. This ratio was chosen to be similar to the solidity of grids used in historical experiments. The distance from the centerline of the first bar from each edge is one half of the mesh spacing, $\frac{1}{2}M$.

### 2.1.5 The linear motor

We actuate grid motion with a linear motor built by Trilogy Systems that is driven by a programmable computer manufactured by Parker Automation. The linear motor is capable of large accelerations and velocities of several meters per second. We typically initiate the grid motion using an acceleration of 4 g, followed by a period at a constant velocity up to 2 m/s, and ending in a 4 g deceleration. In this way, the grid moves at a constant velocity for about 80% of its 10 to 15 cm trajectory along the channel. The grid moves above the window by the same distance that it was initially below the window.

The linear motor controller is also responsible for the timing of the experiment. This typically includes actuating an agitation of the particle suspension or stirring of the fluid, followed by a period of time to allow the flow to relax, executing the grid motion described above, and sending a signal to the camera controller to record the decay of turbulent motions.

### 2.1.6 Air bearing

The cryostat and camera are mounted on an air bearing manufactured by Pneumo

Precision, Inc. Using 200 to 350 kPa (gauge) of air pressure, the equipment is suspended and confined to rotate about an axis fixed to within microns with very little friction or vibration. The cryostat rotates freely about its symmetry axis along with other equipment including a camera. Rotation rates of up to 2 Hz are achieved by limiting the voltage applied to a 24 VDC motor. All of the rotating equipment is electronically self-contained, and operates without a tether to the lab, without slip rings.

### 2.1.7 Camera

We use a Phantom v5.0 camera with 1 GB of onboard memory and a square, one megapixel CMOS sensor. Pixels are 16 μm across, and we use a 105 mm Nikon macro lens with a magnification of one. The camera observes an area of dimension 1.6 ×1.6 cm, representing about one third of the width of the channel, and more than twice the grid's mesh spacing.

The camera collects and stores 1012 image frames at up to 1000 frames per second. The camera can also be slaved to an external trigger, with time between triggers varying from 1 ms to 50 ms. Using a single board computer and a program that triggers the camera, we are able to choose arbitrarily the time between each movie frame and the next, and vary this inter-frame time continuously over the course of an individual movie. In this way, we can tailor the inter-frame time to the instantaneous time dynamics of the flow. This, in turn, optimizes the quality of the resultant PIV data, and maximizes the total length of time a limited number of frames will span. In the rotating frame, the signal for the computer to start triggering the camera is delivered by a phototransistor aimed at a ring of infrared light emitting diodes (LEDs) fixed in the lab frame. The LEDs

are illuminated according to a signal provided by the programmable linear motor controller described in section 2.1.5; the linear motor controls the timing of the experiment.

### 2.1.8 Laser and optics

An argon ion laser illuminates suspended particles. The laser can deliver up to 6 W of polychromatic light, with two dominant wavelengths in the blue and green colors. The illuminating volume of light is shaped by lenses that expand the 2 mm beam in the vertical direction and focusing it in the horizontal direction, forming a thin sheet with almost constant intensity across its height of 1.5 cm. The camera is aimed at the thinnest portion of the sheet. The beam from an argon ion laser, such as the one we are using, is nearly Gaussian in profile and can be focused tightly. According to Gaussian optics, the width of the waist of a focused beam is

$$d_o = 2\lambda f / \pi w, \tag{2.1.1}$$

for $\lambda$, the wavelength of the light, $f$, the focal length of the optics, and $w$, the radius of the input beam. For our laser and optics, $d_o = 100$ μm, though we expect imperfections in the beam and lenses to yield a slightly larger width in practice.

In order to provide illumination that is stationary in the rotating frame, we transfer the beam to optics on the rotating table by passing it vertically along the axis of rotation, as depicted in figure 2.4. A mirror on the rotating table collects the beam, and the sheet is formed in the rotating frame. The beam is carefully aligned with the axis of rotation using two pinholes in the rotating frame, until we observe by eye that the beam does not wander when the table is rotated. In practice, the alignment can be accomplished to

within about 100 μm. Because the reflectivity of mirrors depends on the angle of its surface relative to the polarization of the reflected light, we circularly polarize the laser beam with a quarter-wave plate. This ensures that the beam intensity remains constant as the apparatus rotates.

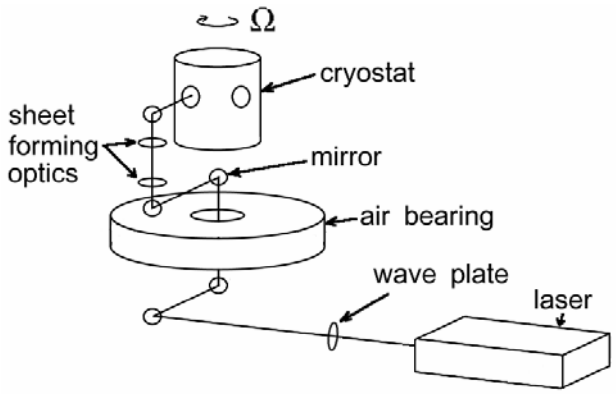


**Figure 2.4**: The line traces the path of the laser beam, and the circles represent mirrors. All fixtures below the air bearing are fixed to a table; everything above the air bearing rotates together, including the beam when it is carefully aligned with the axis of rotation.

## 2.2 Particle image velocimetry

### 2.2.1 Brief description

Particle image velocimetry (PIV) is a technique for extracting the velocities of particle ensembles from images of particles captured at successive times; see Raffel et al. (1998). Typically, velocity vectors are computed for each of a set of small sub-regions of a larger image. The method is widely used, because of the relative simplicity of its implementation and the analysis of the resultant data.

In our realization, separate images of particles in a fixed volume are made at successive times. As illustrated in figure 2.5, the images are broken into smaller square regions, which we call interrogation areas. Two interrogation areas at a particular

location in space, from images taken at successive times, are compared to find how the particles have moved in the time between the acquisitions of each image. In this way, PIV yields a velocity vector, $\boldsymbol{u}(x,y) = u(x,y)\hat{\mathbf{e}}_x + v(x,y)\hat{\mathbf{e}}_y$, for a series of points located at some value of $x$ in the horizontal direction, $\hat{\mathbf{e}}_x$, and $y$ in the vertical direction, $\hat{\mathbf{e}}_y$.

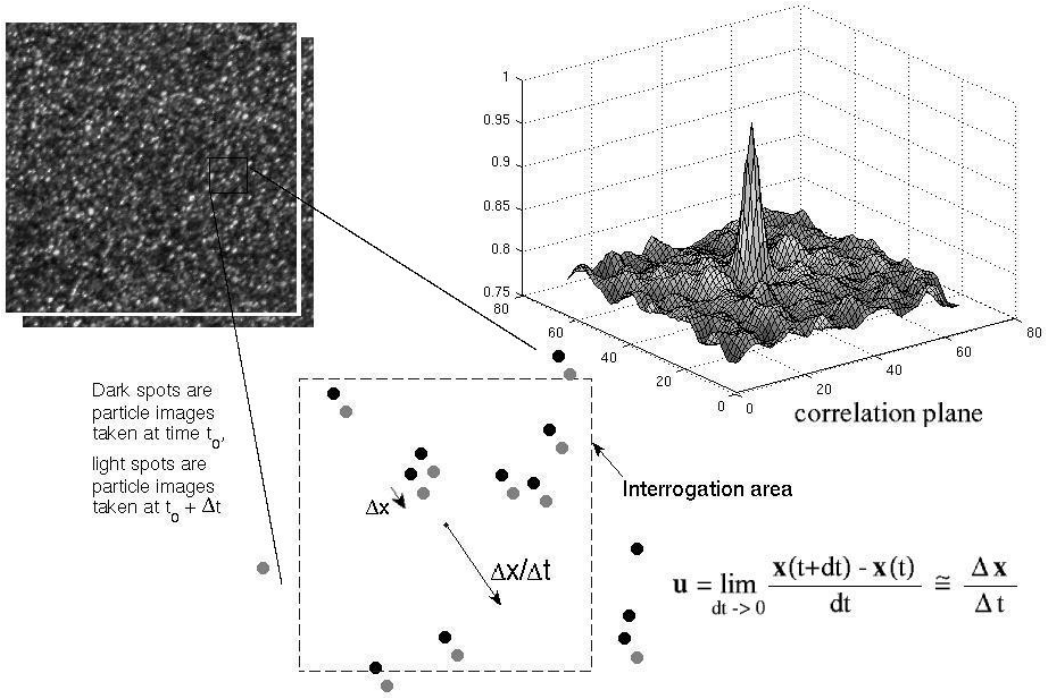


**Figure 2.5**: Examples of two images taken at successive times are shown at the top left. Small regions are taken from the images, called interrogation areas. The cross-correlation of the interrogation areas is computed, shown in the top right. The location of the peak gives the relative offset, $\Delta\boldsymbol{x}$, of the particles between the two interrogation areas. A vector is assigned to the center of the interrogation area, whose magnitude and direction are given by $\Delta\boldsymbol{x}/\Delta t$. This calculation is repeated for a chosen set of pairs of interrogation areas in the two images.

The comparison of two interrogation areas is done by cross correlation. That is, one interrogation area is shifted with respect to the other, in the plane, and the correlation coefficient is computed. The correlation coefficient is computed for all possible relative

shifts of the interrogation areas. In practice, this operation is done in Fourier space, where it can be done more efficiently. The assumption is that for a large enough collection of particles, the maximum correlation will occur when the interrogation area is shifted by the opposite of the mean particle displacement in the area, $-\Delta\boldsymbol{x}$. This maximum presents itself as a peak in the cross-correlation plane. A further refinement of the peak's location can be made by fitting the peak with some model function, and using the peak of the model function. The velocity assigned to the center of the interrogation area is $\Delta\boldsymbol{x}/\Delta t$, where $\Delta t$ is the time between the two images. Velocity vectors are found for every interrogation area pair in the pair of images.

### 2.2.2 PIV data processing

Several special characteristics of our implementation are noted here. We have employed additional refinements to the basic PIV algorithm. These include multiplying adjacent correlation planes, and writing our code to exploit the multithreading capability of a 128 processor computer.

The multiplication of correlation planes adjacent in space enhances signal to noise by accentuating the peak we seek relative to spurious correlations. The displacement of particles in adjacent interrogation areas is highly correlated, because the interrogation areas are much smaller than the energetic scales of turbulent motion, whereas the spurious correlations between mismatched particles are random. We use the position of the peak in the product plane to localize our search for a peak in the correlation planes of the individual interrogation areas. The peak location, and $\Delta\boldsymbol{x}$, are then computed from these individual (un-multiplied) correlation planes, as in normal PIV.

A multi-pass algorithm is used, where successive passes shift one of the pair of interrogation areas by the expected particle displacement, predicted by the previous pass. This minimizes the number of unpaired particle images that appear in the interrogation areas, and strengthens the correlation peak. Successive passes are made at higher resolutions, with the first pass's interrogation area being a 96 pixel square, the subsequent one having 48 pixels on a side, and the last, 24 pixels, for example.

Because of the large number of images we produce with the high speed camera, we require that data processing be done at high speed. A typical day of data collection results in 20 to 30 GB of image data. We wrote a flexible multithreaded PIV algorithm that runs on an in-house 128 processor SGI/Cray supercomputer. The code was written using OpenMP in the C programming language, and distributes the task of performing correlations among the processors. The code performs multi-pass PIV with several error checking schemes and a noise filter at a rate of about 5 image pairs per second on 24 processors, or about 3.5 min/GB. This compares with 12 hrs/GB on a desktop PC. This speedup is also crucial for improving data quality, since we can adjust the conditions of the experiment using the quick quantitative feedback of the PIV analysis.

### 2.2.3 Limitation of the PIV technique at high Reynolds numbers

The effective probe size, or resolution, inherent in PIV is better stated as the interrogation area size, rather than the particle size. We have suggested that the particle itself should be smaller than all fluid length scales in order to be able to trace it accurately, an idea that is discussed in detail in chapter 3. In order for our PIV measurement to be a faithful representation of the fluid motion, we may also require that

the volume of fluid and particles used to construct each vector be smaller than the smallest length scales in the flow, the Kolmogorov scale, $\eta$, see (1.4.1). We do not meet this condition in the present measurements, but we can obtain useful data as we shall illustrate subsequently. In addition to the constraints on the particles discussed in chapter 3, we require that the particle volume fraction be low enough that it does not affect the fluid's physical properties. However, we must introduce enough particles that the PIV algorithm finds a sufficient number in each small patch of an image to assess their displacement. A typically accepted upper bound for the volume fraction of particles is $10^{-5}$. In order to resolve $\eta$ by using an interrogation area with linear dimension $\eta/5$, we must find five particles therein, and the particles' maximum diameter can easily be found to be limited at about 20 nm. Such a particle is difficult to detect optically, since it scatters very little light. For this reason, PIV may in principle not be the appropriate technique for making accurate measurements of highly turbulent flows in liquid helium. However, the particles we introduce in chapter 3, while not small enough to allow resolution of the Kolmogorov scale, are useful for other techniques, such as individual particle tracking.

# Chapter 3

# Particle selection

Here we discuss the selection of particles suitable for turbulence measurements in liquid helium. We outline a method for judging a particle in terms of its ability accurately to trace a fluid flow. According to these conditions, we survey and evaluate commercial particles and previous work to establish that we must develop a new particle that is satisfactory for use as a tracer in liquid helium. Although a parallel effort at Florida State University (Zhang et al. 2004) has recently produced a similar review, we answer several important questions in more detail including particle characterization and behavior in a cryogenic fluid. In addition to specific guidelines useful for future researchers, we offer what we believe is the first practical solution to the problem of quantitatively tracing the motion of liquid helium using particles. In order to do so, we develop a method to generate a mist of solid hydrogen particles.

## 3.1 Tracer particle fidelity

### 3.1.1 A method to evaluate a particle as a fluid tracer

The dynamics of a particle in an unsteady flow and its evaluation as a faithful fluid flow tracer have been studied extensively (e.g., Mei 1996). As has been suggested

before (White 2001), we consider the fidelity with which a particle follows the fluid flow to be measured by two parameters, the Stokes number and the Froude number. These follow from an approximation to the equation of motion of the particle, whose full form is proposed by Maxey and Riley (1983).

Consider that a particle's inertia is balanced by the sum of the buoyancy force and the drag proportional to the velocity difference between the particle and the fluid. This simple description yields the following equation for the change in momentum of a particle, with velocities and time normalized to characteristic scales of the flow, $u_{\text{fluid}}$ and $\tau_{\text{fluid}}$ respectively:

$$\tau_{\text{particle}} / \tau_{\text{fluid}} \, \partial v/\partial t = u_{\text{settle}} / u_{\text{fluid}} - (u - v). \tag{3.1.1}$$

For the velocity difference between fluid and particle, $u - v$, this equation may be written as

$$u - v = Fr - St \, \partial v/\partial t,$$

$$\text{with } St = \tau_{\text{particle}} / \tau_{\text{fluid}}, \tag{3.1.2}$$

$$\text{and } Fr = u_{\text{settle}} / u_{\text{fluid}},$$

where $St$ is the Stokes number, measuring the importance of the particle inertia, and $Fr$ is the Froude number, measuring the importance of the particle settling velocity. We infer from the above relation that the fractional error in measurement of the fluid velocity, $u - v$, is roughly the value of the Stokes or Froude number, whichever is larger.

We can evaluate the Stokes and Froude numbers for candidate particles by using the particle response time and settling velocity,

$$\tau_{\text{particle}} = d^2 \rho_{\text{particle}} / 18\mu, \tag{3.1.3}$$

$$\text{and } u_{\text{settle}} = d^2 \Delta\rho g / 18\mu, \tag{3.1.4}$$

where $d$ is the particle diameter, $\rho_{particle}$ is the particle density, $\mu$ is the fluid's dynamic viscosity, $\Delta\rho$ is the difference in density between the particle and the fluid, and $g$ is the acceleration of gravity. These expressions follow directly from the equations of motion using Stokes' formula for drag (Batchelor 1967) and the particle density times its volume for its inertia. For the rotating experiments in this thesis, centrifugal acceleration due to rotation is at most 6 % of the gravitational acceleration, and we neglect it. We choose the fluid time and velocity scales to be the Kolmogorov scales in the flow

$$\tau_{fluid} = (\nu/\varepsilon)^{1/2}, \tag{3.1.5}$$

$$\text{and } u_{fluid} = (\nu\varepsilon)^{1/4}, \tag{3.1.6}$$

which measure the finest scales of flow (Frisch 1995). If a particle is able to respond to these motions, it will also trace the range of motions present in a turbulent flow.

Although including additional terms in the particle equation of motion, (3.1.1), given by Maxey and Riley (1983) will result in additional parameters, we suggest that minimizing the Stokes and Froude numbers alone will minimize all contributions to deviations of the particle motion from the fluid motion. For example, inclusion of the 'added mass' term results in an additional parameter that is equal to $\frac{1}{2}St$ when the particle density and fluid density are comparable.

Let us note in addition that the above results are derived for a spherical particle. A particle with a more complex geometry is likely to perform better than predicted by our model, in the sense that it will behave more like a fluid particle due to its increased drag. Finally, evaluating a particle according to the parameters $St$ and $Fr$ is cumbersome, because in an evolving flow, they are functions of both time and the initial conditions. We propose an alternative below.

### 3.1.2 Suggested alternate formulation

We survey and study particle candidates in section 3.4 and would like our conclusions to be useful in a more general setting than our own application. With this goal in mind, we recast the Stokes and Froude numbers in terms of the Reynolds number, $Re = ul/\nu$. We then find bounds in the Reynolds number for which a particular particle can be considered to represent a fluid parcel. Here, we take $u$ as the root-mean-square (RMS) velocity of the flow, and $l$ as the integral of the normalized longitudinal two-point velocity correlation function, or the integral length scale.

Consider that for a particular combination of the particle, the fluid, and the flow, there are some $St_{max}$ and $Fr_{max}$, above which deviation of the motion of a particle from the motion of the fluid is too large, in a sense that we will propose in section 3.2. Using Kolmogorov's relation for homogeneous and isotropic turbulence, $\varepsilon \cong u^3/l$, we regroup the definitions of $St$ and $Fr$, and find that

$$18\, St_{max} > (d/l)^2\, (\rho_{particle}/\rho_{fluid})\, Re^{3/2}, \tag{3.1.7}$$

$$\text{and } 18\, Fr_{max} > (d^2 gl/\nu^2)\, (\Delta\rho/\rho_{fluid})\, Re^{-3/4}. \tag{3.1.8}$$

We have chosen, in our introduction of $Re$, to remove the explicit appearance of the characteristic velocity, $u$, since it changes rapidly with time in the flows we present in chapters 4 and 5, though other choices are possible. In our flows, and in many other flows of interest, the Reynolds number and the integral length scale do not change quickly, making our result easier to generalize. Regardless of these considerations, we write our expressions equivalently in terms of limits on the Reynolds number:

$$Re_{max}^{3/2} = 18\, St_{max}\, (l/d)^2\, (\rho_{fluid}/\rho_{particle}) \tag{3.1.9}$$

$$Re_{min}^{3/4} = (18\, Fr_{max})^{-1}\, (d^2 gl/\nu^2)\, (\Delta\rho/\rho_{fluid}). \tag{3.1.10}$$

The minimum Reynolds number reflects the fact that turbulent intensity is required to keep the particle's settling velocity from dominating its motion. The maximum Reynolds number is due to the inertia of the particle resisting the large accelerations of an intensely turbulent flow. Note that a neutrally buoyant particle can be used at arbitrarily low Reynolds numbers, and in this case $Re_{max}$ is the appropriate parameter.

In order for there to be a range of Reynolds numbers for which the particle is useful according to these criteria, the ratio

$$B = \frac{Re_{max}}{Re_{min}} = \frac{\rho_f^2}{\rho_p^{2/3}\Delta\rho^{4/3}} \frac{\nu^{8/3}}{g^{4/3}d^4} \tag{3.1.11}$$

must be larger than one. The ratio, $B$, does not depend on the integral scale, and is therefore independent of the flow. The ratio depends only on the physical properties of the fluid and particle, and is particularly sensitive to the particle size.

For clarity, we presented the argument above using a Reynolds number based on the large scales of the flow, but there are other Reynolds numbers more often employed in the literature. The most useful Reynolds number for comparison to a wide variety of theoretical and experimental efforts is based on the Taylor scale, $\lambda$,

$$Re_\lambda = \lambda u / \nu. \tag{3.1.12}$$

An intuitive way to understand $Re_\lambda$ is through the relation $Re_\lambda \approx (15\, Re)^{1/2}$ (Frisch 1995). This is the Reynolds number we will use for comparison in the following sections. Finally, we remind the reader that these results are strictly valid only for high Reynolds number homogeneous and isotropic turbulence, and in the limit of vanishing particle Reynolds number.

## 3.2 Large Froude and Stokes effects

### 3.2.1 Vibrated particles

In the case of a regularly oscillating velocity field, one might readily anticipate that a large Stokes number (or, particle inertia) will yield a measurement that is out of phase with the fluid velocity, but with the right frequency components. Indeed, if we replace the nondimensional fluid velocity, $u$, in equation (3.1.1) by a simple oscillation with frequency ω, normalized by the Kolmogorov time scale, we find that the harmonic part of the solution for $v$, the particle velocity, has the same frequency. In addition, the particle velocity exhibits a phase that is different from that of the imposed fluid velocity by $\tan^{-1}(St\,\omega)$. The importance of this result will become evident in chapter 5, in our discussion of rotating flows, where in some cases we observe the regular oscillation of particles with Stokes numbers of order one.

### 3.2.2 Measurement of large scale flow properties

In liquid helium, almost any choice of particle will yield Stokes and Froude numbers near unity in easily obtainable flow conditions. As shown in section 3.1, a given particle type places restrictions on the experimental parameter space we can explore with acceptable error in measurement. In order to find the limits in Stokes and Froude numbers for which measurement error is tolerable, we consider the case where the Stokes number, or the Froude number, is not infinitesimal. Several research groups have studied these limits, both directly and indirectly. We now provide a brief review of the literature while keeping in mind accurate measurement of the basic large-scale flow characteristics, the fluid's kinetic energy and integral length scale.

Wells and Stock (1983) vary the settling velocity, and thus Froude number, by applying an electric field to charged particles in a wind tunnel. The Stokes number is varied by using two different particle sizes. They find no change in the decay of turbulent kinetic energy behind a grid for $St = 0.023$, when compared with hot wire measurements. However, for $St = 3.0$, the kinetic energy of particles is about 30% smaller than that of the fluid, and they observe a possible change in the slope of the energy decay. In addition, Wells and Stock (1983) find that a large Froude number tends to increase the rate of de-correlation of velocities in space and time. We estimate from their results that as $Fr$ approaches one, the integral time scale measured by the particles is about 25% smaller than that of the flow. Finally, they find that the Stokes number has only a small effect on correlations, and the Froude number has only a small effect on the energy decay law.

Mei et al. (1990) analyze particles in isotropic turbulence, and confirm Wells and Stock's (1983) finding that particle inertia has only a small effect on velocity correlation functions. They also observe that a large settling velocity, and thus large $Fr$, sharply reduces the integral length scale. We estimate from their charts that the integral length is 15% smaller at $Fr = 1$, and 40% smaller at $Fr = 2$, when measured using tracer particles.

Reeks (1977) defines an inverse Stokes number, although the scales used for normalization are unfamiliar from the standpoint of usual turbulence phenomenology. If we take Reeks' measure of particle inertia to be equivalent to our own, one should require that the Stokes number be less than 0.35 to measure within 10% of the fluid kinetic energy, and less than 0.25 to be within 5%.

Voth et al. (2002) describe using particles with diameters comparable to the dissipation scale. The range of particle sizes reported correspond to Stokes numbers ranging from 0.13 to about 40. They find no change in the acceleration variance up to approximately $St = 0.4$. They also have some evidence, based on varying fluid density, which suggests substantial settling velocity effects for Froude numbers as small as 0.1. Because these data correspond only to the largest Stokes number particles ($St = 40$), it is difficult to draw a strong conclusion.

The collection of results suggests that using particles with Stokes and Froude numbers in the range 0.3 to 0.5 result in measurements that are within 5 to 10% of the fluid kinetic energy and integral length scale. The evaluation of the large scale quantities is apparently robust, forgiving of large deviations of the particle's motion from the fluid's motion. However, for negligible errors in velocity measurements due to particle dynamics, we target values that are an order of magnitude smaller. We use

$$St_{max}, Fr_{max} = 0.05. \tag{3.2.1}$$

This, in turn, imposes constraints on our observable Reynolds numbers, as discussed in section 3.1.2.

## 3.3 Particle clumping

An additional problem complicating the use of particles as tracers in liquid helium is that particles stick to each other, and there are no readily available devices to counter this tendency. In water, a surfactant will stabilize a suspension, but this technique is inapplicable in cryogenic fluids. Here, we discuss the mechanism for particle aggregation and ways to mitigate the process. Particles attract each other through the van

der Waals force. In addition, particles in a turbulent flow may be both brought into contact and shorn apart by motions of the fluid. We consider the balance of these interactions, and find that since the attractive van der Waals force is stronger than any other, particles aggregate into ever-larger clusters at a predictable rate.

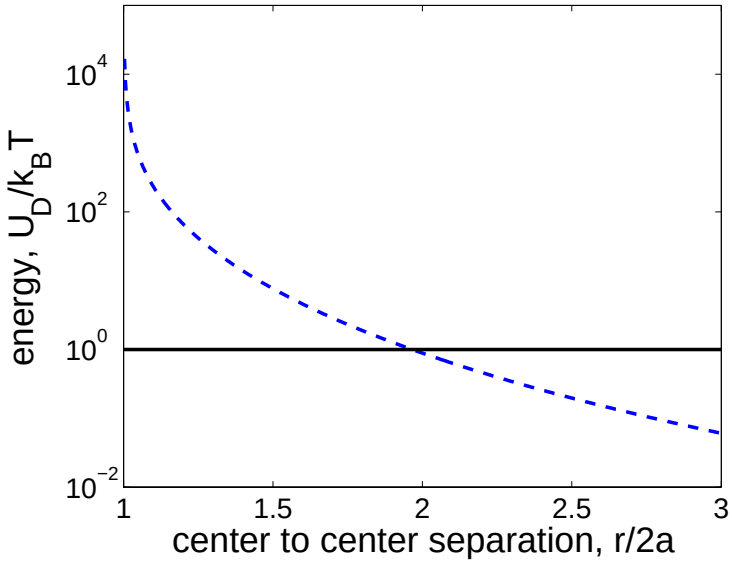


**Figure 3.1**: The van der Waals potential as a function of sphere separation is the dashed line. We use Hamaker's constant for polystyrene, $A = 8 \times 10^{-20}$ J, but the Hamaker constant for most materials is of the same order. An exception is liquid helium, and since Hamaker's constant for liquid helium is much smaller (Paalanen and Iye 1985), we do not need to account for it as the intervening fluid (Heimenz and Rajagoplan 1997).

### 3.3.1 Comparison of forces

First, we consider the consequence of two particles coming close to each other, or colliding. The force that draws particles together is the same as the one that binds each particle's constituent molecules together to form a solid. These intermolecular forces include ionic interactions, hydrogen bonds, dipole-dipole interactions, and London

dispersion forces. These are sometimes known collectively as van der Waals forces. Once particles are in contact, the force binding two particles overwhelms both the thermal energy of the particles, and separation due to fluid shear.

The attractive potential between two spheres with center to center separation $r$ and with radius $a$ is

$$U_{\mathrm{D}} = \frac{-A}{6}\left[\frac{2a^2}{r^2-4a^2} + \frac{2a^2}{r^2} + \ln\left(\frac{r^2-4a^2}{r^2}\right)\right], \tag{3.3.1}$$

and is a function of Hamaker's constant, $A$ (Vold and Vold 1983). Thermal energy is measured by $E_{\mathrm{T}} = k_{\mathrm{B}}T$, where $k_{\mathrm{B}}$ is Boltzmann's constant, and $T$ is the temperature. At 4.2 K, the thermal energy is

$$E_{\mathrm{T}} = k_{\mathrm{B}}T \approx 6 \times 10^{-23}\ \mathrm{J}. \tag{3.3.2}$$

It is evident from figure 3.1 that for separations less than 2 diameters, it is unlikely that thermal fluctuations will separate particles under the influence of the van der Waals potential.

We estimate the turbulent contribution to particle dispersion by considering the effect of a shear flow on a pair of particles in contact. Note that at distances smaller than the Kolmogorov dissipation scale, velocity gradients are linear. For particle separations much smaller than the dissipation scale, the difference in fluid velocities across a distance $r$ are approximated by

$$\Delta u \approx (r/\eta)\, u_{\mathrm{fluid}} = r\,(\varepsilon/\nu)^{1/2} \approx r\,(\nu/l^2)\, Re^{3/2}, \tag{3.3.3}$$

where $\eta$ is the dissipation scale defined in (1.3.1), $u_{\mathrm{fluid}}$ is the velocity scale defined in (3.1.6), and we have rewritten the expression in terms of a Reynolds number as in section 3.1.2. We propose that an upper bound on the force the fluid can exert to separate

particles is the drag force given by Stokes for a sphere in a uniform flow (Batchelor 1967) with velocity $\Delta u$. We take the velocity difference to be that between the centers of two touching particles, such that $r = 2a$. In this case, the drag force is

$$F_S = 12\pi a^2 (\mu^2/\rho l^2) Re^{3/2}, \tag{3.3.4}$$

where $\mu$ and $\rho$ are the dynamic viscosity and density of the fluid. The largest Reynolds number we can reach in our apparatus is about 10,000, giving a force of about 20 pN between 2 μm particles in liquid helium.

The attractive force is calculated from the gradient of the potential given in (3.3.2). For small sphere surface separations, the expression for the force reduces to

$$F_D = \nabla U_D = Aa/12s^2, \tag{3.3.5}$$

where $s = r - 2a$ and $0 < s << a$. Since the preceeding expression diverges for small $s$, we are faced with the problem of choosing a reasonable value for the separation of contacting particles. If the particles were perfect spheres, the separation would be on the order of the dimension of its constituent molecules. In fact, remarkably uniform polystyrene spheres are commercially available from Bang's Laboratories or Polymer Microspheres. Assume that some surface roughness separates the particles, and that this roughness is of the order of one percent of the particle diameter. This distance is 20 nm for a 0.8 μm sphere. Figure 3.2 depicts the ratio of the attractive force to the drag force for several values of the surface roughness. It is apparent that the binding force is unlikely to be overcome by turbulent shear for particles with diameters less than 5 μm, even for larger values of the surface roughness.

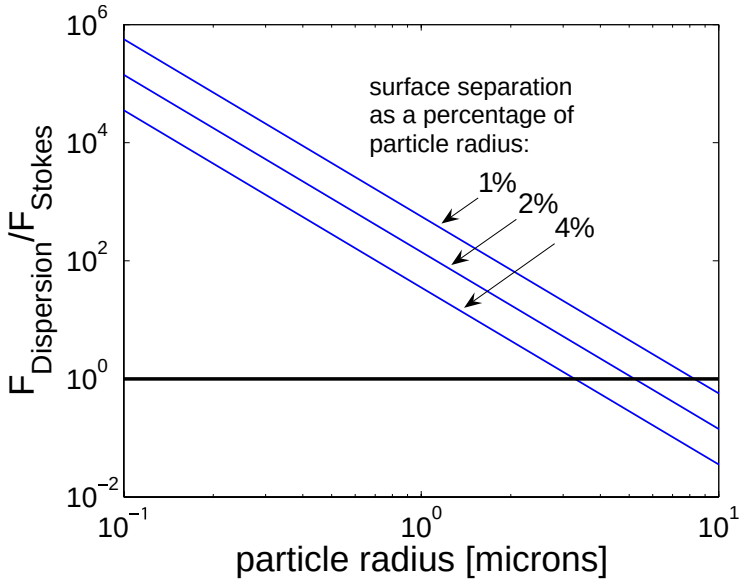


**Figure 3.2**: The ratio of the attractive van der Waals force to the fluid shear induced separation force for polystyrene spheres in a turbulent flow at $Re_\lambda = 400$. The ratio is given as a function of the sphere's radius for several surface separations. The surface separation is expressed as a fraction of the sphere radius, imagining that some surface roughness keeps the spheres further apart than if they were perfect spheres. For particles smaller than a few microns, the van der Waals force is much larger than our estimated upper bound for the separation force.

### 3.3.2 Rate of coagulation

We show in the previous section that particles brought together are unlikely to separate. Here, we estimate how often the combination of particles happens. Fluid shear is a mechanism for breaking up particle aggregates, but the same mechanism causes particles to collide, and the two processes may reach equilibrium. Vold and Vold (1983) give Smoluchowski's differential equation controlling the process of shear coagulation, assuming that combined particles are inseparable:

$$dN/dt = -(16/3)N_0 a^3 (du/dz)N. \tag{3.3.6}$$

$N$ is the total number of particles per unit volume, with initial value $N_0$, and $du/dz$ is the shear rate that we estimate in (3.3.3). The solution to this equation is an exponential decay, with the time for the particle number to halve being given by

$$\tau_{½} = (\pi l^2 \log(2)) / (4\Phi\nu Re^{3/2}), \tag{3.3.7}$$

where $\Phi$ is the volume fraction of particles relative to the fluid, and is $3N_0/(4\pi a^3)$.

For typical conditions after the fluid is agitated with a grid, the time constant given by (3.3.7) is about 1 min. This result indicates that if particles of the desired initial size were somehow dispersed, there is a useful period of time during which we may use them as fluid tracers. Notice, however, that $\tau_{½}$ is inversely proportional to the particle volume fraction. Consider that the particles must be injected into the sample volume of fluid as a concentrated solution, and that this injection process is necessarily turbulent. At the time of injection and in the vicinity of the injector, the volume fraction of particles is larger than in the fully dispersed solution, perhaps by many orders of magnitude. If the initial volume fraction is roughly 0.1, and we show in section 3.7.1 that this is a typical value, $\tau_{½}$ is reduced to a small fraction of a second. This leaves us very little time to disperse the particles in the full volume before they have irreversibly clumped into effectively larger particles.

### 3.3.3 Suspension stabilization

There are two methods at our disposal for keeping particles from coalescing. The first is to coat the particles with long chain molecules, a method known as steric stabilization. This can be accomplished by manufacturing particles with a surface coating of a certain polymer, or by adding a surfactant that finds its way to the particle-

solvent interface. A surfactant is typically used in aqueous solutions. The second method is to charge the particles, and rely on electrostatic repulsion. In order to do this, one can permanently coat the surface of the particles with polar groups, or force the particles to accumulate free ions on their surfaces. We briefly discuss each of these methods.

The effectiveness of the solutions exploiting polymers depends on the flexibility of the polymer molecules (Vold and Vold 1983). In cryogenic fluids, this mechanism is excluded, because the temperature of a cryogenic fluid is below the glass transition temperature of all polymers. One can, however, strive to minimize the attraction by coating the particle with a layer of a fluorinated polymer. Fluorinated compounds are highly non-reactive and the coating would alleviate the tendency to aggregate for the same reason that makes Teflon useful. There would, however, still be a net attractive force between particles.

The dissociation of an ion that allows the formation of a polar group in a solution requires a polar solvent, such as water. Liquid nitrogen and liquid helium, the fluids of interest to us here, are non-polar. Therefore, this solution is inapplicable. The other technique of adding an electrostatic charge to particles in solution has been implemented successfully (Huber and Wirth 2003). Experimentalists mixing spherical polymer particles using what is essentially a blender in liquid nitrogen found that the particles collected a net charge. The result is potentially useful for dispersing solid tracer particles in cryogenic fluids, though long-range inter-particle forces may complicate the analysis of particle motion relative to the fluid.

### 3.3.4 Methods for dispersing particles

We have sought methods for temporarily dispersing aggregated particles in cryogenic fluids. The methods include ultrasound induced cavitation and fluid shearing, which we realized in various ways in our cryostat. Ultrasonic cleaning baths use the first technique to remove debris from items immersed in water, and we found it effective at dispersing aqueous suspensions. We attached the ultrasound transducer from such a cleaning bath to the channel inside our cryostat, but observed no effect on suspensions in liquid nitrogen. We tried exploiting the second mechanism by vigorously agitating the grid, as well as constructing various kinds of high-speed mixers and propellers. Again, we observed no effect on the size of particle aggregates. It is possible that either method could work with a more concerted engineering effort. We suggest that further attempts concentrate on pressurizing the fluid, in order to bring it temporarily away from its boiling point, as a first step in implementing either technique.

## 3.4 Evaluation of available seeding techniques

A careful review of products and previous work is required, since a quick review of the literature might lead the reader to conclude that particles that meet our specifications are readily available. For example, hollow glass particles are referred to as being in the 1 to 5 μm diameter range (White et al. 2002, or Donnelly et al. 2002), and velocity measurements of micron-sized solid polymer particles are suggested as being of the individual particles rather than the velocities of particle aggregates (Zhang and Van Sciver 2005, or Zhang et al. 2004). We shall see that these particles would indeed make suitable tracers but cannot be made to work well for technical reasons.

### 3.4.1 Commercially available particles – hollow glass spheres

Hollow shells made of glass are manufactured by at least two companies, PQCorp and 3M. The companies specify that a sample of particles include hollow glass spheres in a wide range of sizes, from around 10 μm to several hundred microns, and with a range of densities close to that of liquid helium, typically 0.14 to 0.19 g/cc (e.g., Potters 2006). The opportunity presented to the experimentalist stems from the possible existence of suitably small particles at one end of the size distribution. They are not revealed in data supplied by the manufacturers. According to our analysis, we require a particle smaller than 5 μm in diameter, and with a density of less than 0.14 g/cc. Although the companies' ability to make small particles with an almost perfect density match to helium is remarkable, we find that even the smallest particles are too large to trace a turbulent flow in liquid helium with the desirable level of fidelity. We show a suspension of these spheres in liquid helium in figure 3.3.

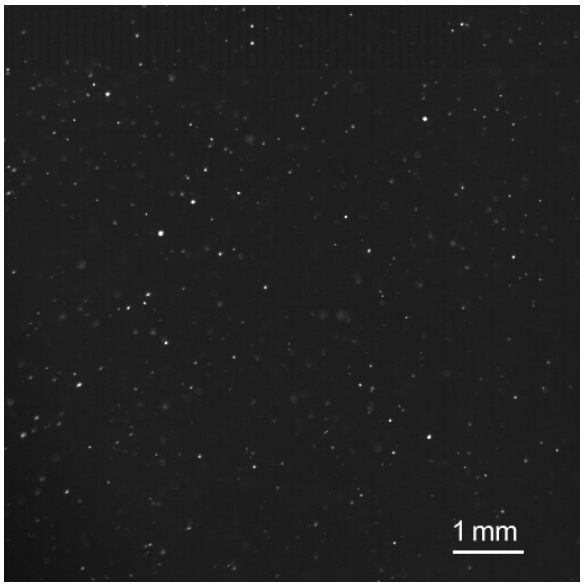


**Figure 3.3**: An image of a suspension of hollow glass spheres in liquid helium.

A good example of the use of hollow glass particles as a tracer particle in liquid helium is provided by my predecessor's admirable work. White (2001) refined a technique for segregating small glass particles that resulted in the first PIV data taken in liquid helium. At a first glance through a microscope, one can see particles that range in size from 1 to 30 μm. Previous studies have used this observation as evidence that there exist small, hollow spheres. However, a simple test reveals that even the smallest hollow particles are close to 10 μm across. We introduce particles at the bottom of a graduated cylinder filled with methanol, and collect what rises to the surface after different periods of time from the time of injection. The smallest particles that float range in diameter from 9 to 16 μm, and are mixed with a particles up to 35 μm. At the bottom of the methanol column lie the smaller particles, between 1 and 15 μm in diameter. These particles are either solid glass or incomplete shells. As revealed in figure 3.4, the difference from the required size specification, though only a factor of two, is crucial since both the Stokes and Froude numbers depend on the square of the particle size.

The great advantage of the hollow glass spheres is that they are apparently immune to the clumping problems that plague solid particles. This may be because the attractive force between solid particles depends on the integral of the attractive forces between all the molecules in each particle. However, for the hollow sphere at small separation distances, we find that the problem reduces to the attraction between only those parts of the thin shells that are closest to each other. This allows for the possibility that a small hollow particle may in the future be manufactured that would be an accurate tracer of liquid helium flows.

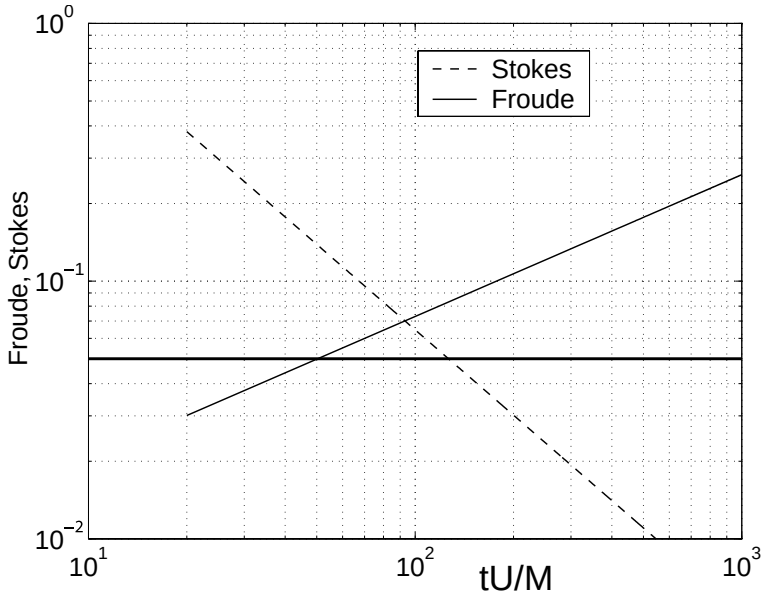


**Figure 3.4**: The chart shows the Stokes and Froude numbers as they evolve in a turbulent flow generated by a grid with 7.2 mm mesh spacing, $M$, drawn at $U$ = 2.0 m/s in liquid helium. The parameters are calculated for a 9 μm hollow glass sphere. The horizontal line is the maximum value for either parameter determined in section 3.2, and that either one parameter or the other is larger at any moment indicates that the particle does not trace fluid motions accurately.

### 3.4.2 Commercially available particles – solid beads

Several manufacturers produce solid spherical particles that are available in a wide range of tightly controlled sizes, from nanometers to millimeters. Experimentalists seeking tracers for water often use particles of this type. Particle densities range from just over that of water, 1.06 g/cc for polystyrene micro-spheres, to several g/cc for solid glass micro-spheres. In a turbulent liquid helium flow, a solid particle with such a relatively large density needs to be considerably smaller than a hollow one in order not to sink. For typical turbulent flow conditions, we seek a solid particle that is smaller than 1 μm. Zhang and Van Sciver (2005) used such polystyrene particles to observe thermally

driven flows in liquid helium. We have also tried making velocity measurements using particles of this type, made from a variety of materials.

We find that the problem with using solid particles is that they are found in a cryogenic fluid only as tightly bound clusters. We have tried several techniques for injecting and agitating them, as well as using particles made of different materials. Nonetheless, the particle images appear with a wide range of intensities typical of a polydisperse distribution (see figure 3.5, left), rather than the uniform appearance of monodisperse particles suspended in water (see figure 3.5, right), for example. As suggested in our brief discussion of the physics of clumping in section 3.3, the particles probably encounter and bind to each other during injection, when they are necessarily highly concentrated. Once they bind together, it is difficult to separate them.

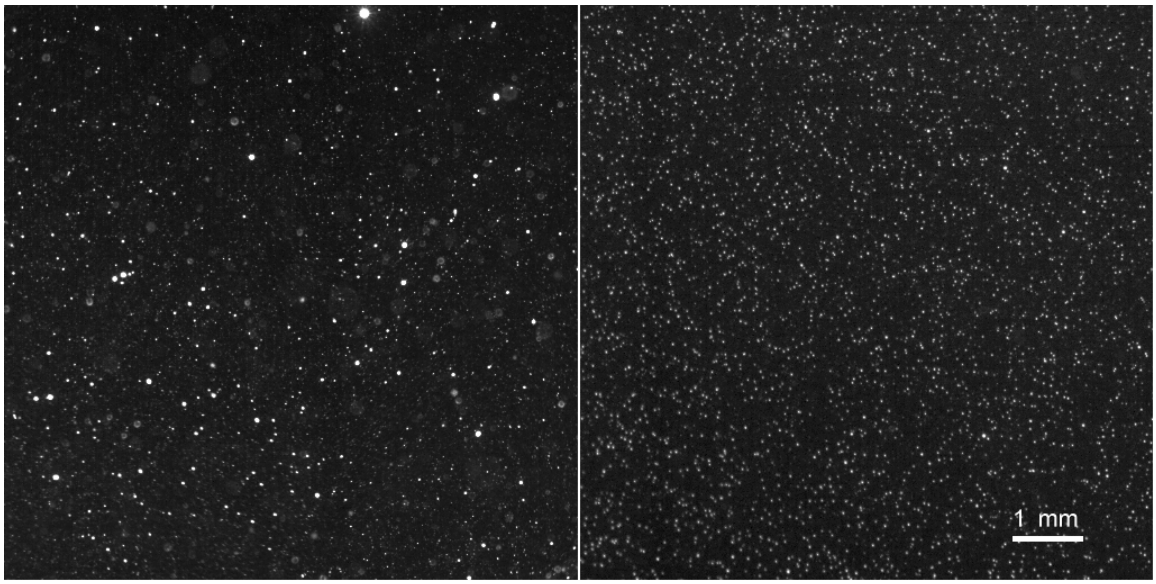


**Figure 3.5**: On the left are clumps of 2 μm polystyrene particles in liquid helium. On the right are identical particles in water, using a surfactant to disperse them.

The Stokes and Froude numbers for a clump of particles will be larger than those for an individual particle. We estimate based on the intensity of light scattered by the

particle clusters that the aggregates are roughly at least 3 particle diameters across. However, we emphasize that such a technique for measuring particle size cannot be relied on, except to say that the particle clumps must be larger than individual particles. As suggested in figure 3.6, a three particle diameter clump is unsuitable for making quantitative measurements of flow velocities.

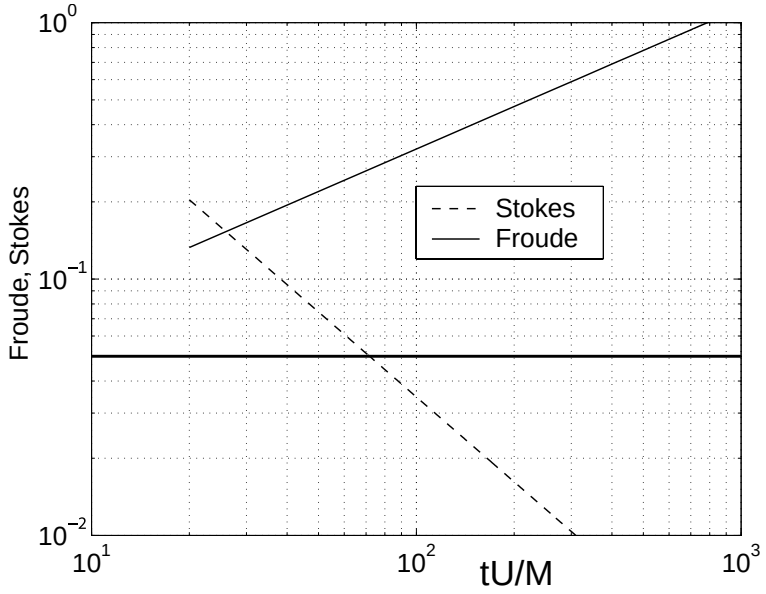


**Figure 3.6**: The chart shows the Stokes and Froude numbers as they evolve in a turbulent flow generated by a grid with 7.2 mm mesh spacing, $M$, drawn at $U$ = 2.0 m/s in liquid helium. The parameters are calculated for a clump of polystyrene particles with a characteristic diameter of 2.4 μm. The horizontal line is the maximum value for either parameter determined in section 3.2, and that either one parameter or both is larger at any moment indicates that the particle clump does not trace fluid motions accurately.

In closing, we note that Zhang and Van Sciver (2005) report measuring the settling velocity of 0.8 μm polystyrene particles in liquid helium as 6 mm/s. However, the settling velocity of individual 0.8 μm polystyrene spheres is predicted to be about

160 μm/s in liquid helium. Their reported settling velocity is closer to that of a 5 μm particle, presumably a large cluster of the smaller spheres.

### 3.4.3 Commercially available particles – other types of particles

We have also considered the suitability of other commercially available particles and powders, and experimented with them. These include silica aerogels, polymer micro-balloons, carbonized micro-balloons, Teflon powders, porous ceramic powders, frozen electrosprays, and pollen. We determined that they could not be useful, usually because of particle diameter, although we will not rule out the possibility that any of these products could be made to work with greater effort.

### 3.4.4 Review of previous work to make frozen particles

The effort to seed liquid helium with a tracer particle dates back 50 years, when Chopra and Brown (1957) injected a mixture of hydrogen and deuterium into liquid helium through a heated nozzle. They were able to make millimeter size particles, and noted that the particles tended to stick to each other and to the walls of the container. Subsequent efforts refined the procedure and reduced the size of the resultant particles. In each of the following cases, hydrogen gas was injected into the cryostat through a large nozzle of order 1 mm in diameter. Chung and Critchlow (1965) report particles with sizes of several hundred microns and Kitchens et al. (1965) report 20 to 100 μm particles, each of the groups working in superfluid helium. More recently, Murakami and Ichikawa (1989) and Nakano and Murakami (1992) report creating 1 μm hydrogen particles in superfluid helium, although they offer no evidence to support their claim on

the particle diameter. Based on the experiments we describe below, we consider it unlikely that the particles they observed were in fact as small as they report.

Celik et al. (2000) have undertaken an effort to make a hydrogen atomizer to generate smaller particles, though they do not estimate the resulting particles size. Celik and van Sciver (2002) report the generation of 10 μm neon particles using a similar apparatus.

A crucial breakthrough was made independently by several groups, including our own. Boltnev et al. (2002) describe the dilution, at room temperature, of hydrogen with large amounts of helium gas. This dilute mixture was then passed through a nozzle above the liquid helium bath, forming a jet that impinged on the free surface. Boltnev et al. (2002) report the possible existence of submicron particles generated in this fashion. Their goal, however, is quite different from ours, since they had no interest in tracing fluid motions. Our discovery was made without any knowledge of this work while observing the peculiar behavior of a liquid hydrogen nozzle of our own design, described below.

## 3.5 The first hydrogen injector

We attempted to produce a fine mist of hydrogen droplets by pushing pure liquid hydrogen through a tiny orifice at high pressure. We were not able to do so, though the injector worked in a different way from that intended. We found in an interesting accident that it is possible to produce a particle mist by diluting hydrogen with helium gas, and we used the nozzle in this way to obtain the results presented in chapters 4 and 5.

An improved injector, designed specifically for use with helium-diluted hydrogen, is described in section 3.6 and used to generate the data presented in chapter 6.

### 3.5.1 The basic properties of hydrogen

Hydrogen is a diatomic gas at room temperature. As it is cooled, it liquefies and solidifies at temperatures above that of liquid helium, despite its smaller molecular weight than liquid helium. This solidification occurs because the broken symmetry in the shape of its constituent molecules leads to stronger intermolecular forces. Hydrogen condenses at 22 K and freezes at 14 K at atmospheric pressure, whereas helium liquefies at 4.2 K.

### 3.5.2 First attempts to make hydrogen particles

Our design for a liquid hydrogen injector is shown in figure 3.7. The constraints on the design are that the injector must pass from the lab into the helium-filled channel through one of its access ports, which are 1 cm tubes that are 1 m long, and that the injector should allow free movement of the grid. The injector is small enough to fit through an opening in the grid.

We introduce gaseous hydrogen at the top of the injector, and it cools during its passage into the cryostat through the injector. We arranged empirically for the hydrogen to exit the nozzle as a liquid by controlling heaters along the injector and at the nozzle. The mechanism of formation of small droplets from liquid exiting a nozzle is an active area of research that is applied, for example, in the optimization of diesel fuel injectors (e.g., Tanner 1997). For our purposes here, it suffices to say that it is known that droplets

much smaller than the nozzle diameter can be formed by jet flow instabilities.

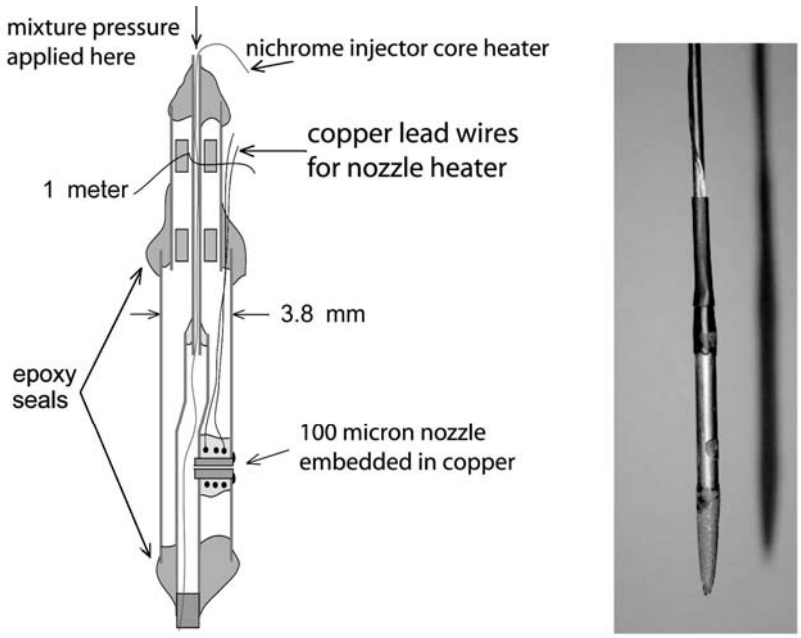


**Figure 3.7**: The liquid hydrogen injector consists of concentric stainless steel tubes that are kept from touching each other with Teflon spacers every 6 cm. A vacuum develops between them when the injector is cooled. Hydrogen gas is introduced at the top. A wire along the length of the core and a wire wrapped around the nozzle can separately be heated to keep the interior of the injector above the freezing point of hydrogen.

The nozzle itself is made from a commercial stainless steel tube with a 100 μm inner diameter. This tube is embedded in copper, and wrapped with a heater wire embedded in thermally conductive epoxy. These measures are taken to ensure that the entire length of the nozzle can be brought above the freezing temperature of hydrogen. The injector nozzle sprays sideways, because our first attempts with a simple downward facing nozzle failed. The reason the downward facing nozzle failed was probably that the newly formed buoyant hydrogen droplets impeded the jet emanating from the nozzle. Finally, the entire passage of hydrogen from the laboratory to the nozzle is through tubes

that are insulated from the outside of the injector by an air-filled space. The thought is that when the injector is placed in liquid helium, the air in this space freezes and leaves a vacuum in its place. The resulting vacuum provides the hydrogen line with insulation, allowing the hydrogen to flow freely through the injector without freezing.

The injector is used by first warming its core with varying amounts of current applied to its heaters, and then flowing hydrogen gas through it using varying amounts of pressure. We use up to 15 W of heat along the length of the core, 1 W at the nozzle, and 400 kPa of pressure. As shown in figure 3.8, we observe vigorous jets of liquid hydrogen emanating into liquid helium, and the formation of hydrogen "snow" of all shapes and sizes. Regardless of the combination of heat and pressure, the snow-like particles that result are about 50 μm in size, often much larger.

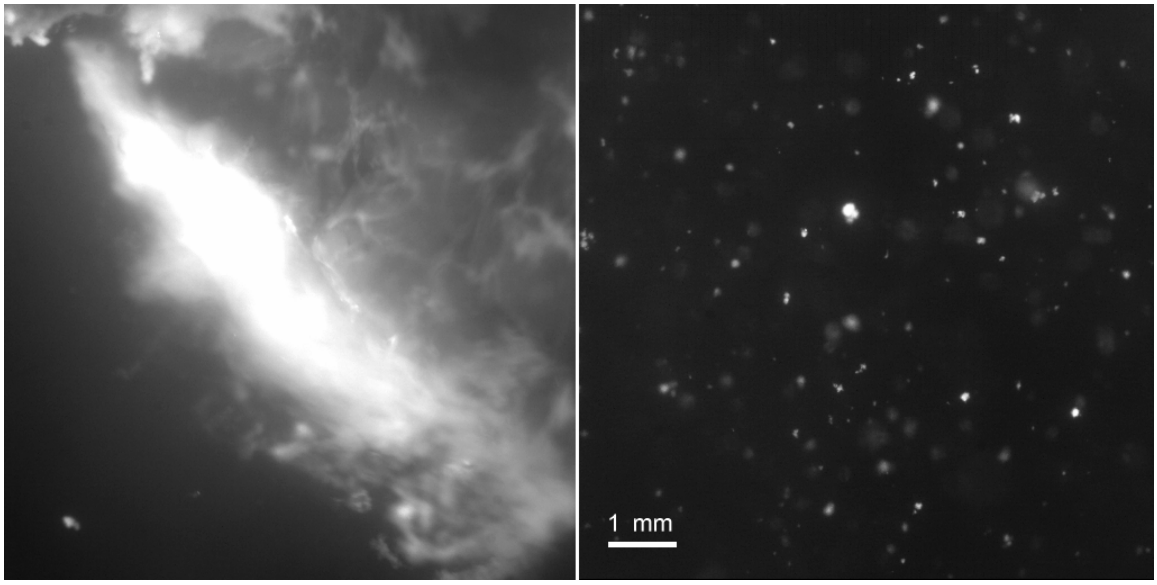


**Figure 3.8**: On the left is a liquid hydrogen jet in liquid helium. On the right are the resultant solid hydrogen "snow flakes" that we estimate are typically about 50 μm in diameter.

Unfortunately, we were never able to produce a hydrogen mist using this technique. However, we observed that the injector produces a mist if it can be made to ingest liquid helium from the cryostat prior to the injection of hydrogen. The subsequent application of hydrogen pressure and heat to the injector expels a dilute gaseous solution of hydrogen and helium that condenses and forms countless tiny particles. We explore this mechanism in section 3.6, below.

## 3.6 The improved hydrogen injector

We produce small hydrogen particles by strongly diluting hydrogen gas with helium at room temperature, and passing the mixture through a nozzle directly into the liquid. Below, we describe how the injector works. Most importantly, our procedure is performed with helium near its boiling point at atmospheric pressure – that is, in a classical fluid. Previous experimenters making hydrogen particles have focused on their production below the transition temperature of helium to a state showing superfluidity. We believe our injector works differently because of this distinction.

### 3.6.1 The injector

The injector is shown in figure 3.9. It is a straight tube extending from the lab to the channel filled with liquid helium through one of the cryostat's access ports. The inner diameter of the injector is 3 mm, and opens to the fluid at its full diameter – there is no nozzle. The length of the inner tube is sheathed by a concentric tube of larger diameter, and the space between the tubes is sealed. Atmospheric gases in this annular space condense and freeze when the injector is cold, forming an insulating vacuum jacket.

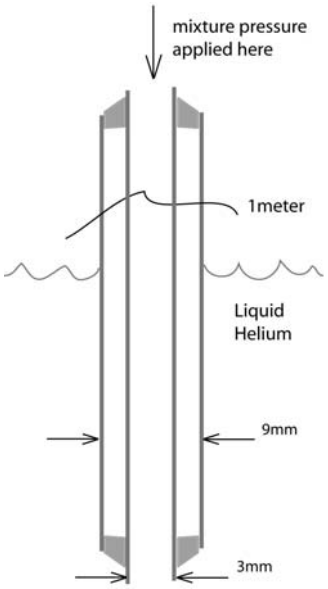


**Figure 3.9**: The schematic shows the design of our diluted hydrogen injector. Hydrogen gas diluted with helium is introduced at the top, and enters the cryostat through the inner of two concentric stainless steel tubes. The mixture cools on passage through the injector and exits below the free surface of liquid helium.

### 3.6.2 Procedure

A mixture of hydrogen and helium gas is prepared in a bottle at room temperature. Typically, the bottle is flushed with hydrogen gas, allowed to vent to atmospheric pressure, and helium gas is added to a pressure yielding the desired mixture ratio. The ratio was most often nearly 1 $H_2$ : 10 He by volume, although we also used other mixture ratios.

The mixture is introduced into the injector through a regulator supplying a small amount of pressure, about 30 kPa, which is further reduced through a needle valve. The valve is opened slowly until the formation of particles is observed through the cryostat windows. Valve position is maintained at this setting for one or two seconds, until it appears that the liquid helium is fully seeded with particles.

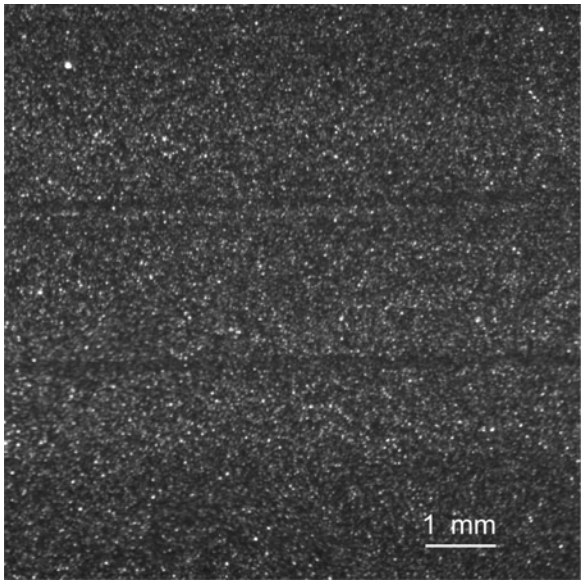


**Figure 3.10**: Hydrogen particles generated by diluting hydrogen gas with helium in a 1 : 10 ratio are shown. The particle size distribution appears polydisperse, but overall the particles appear smaller and more numerous than those shown in figures 3.3, 3.5, or 3.8.

### 3.6.3 Results

An example of particles produced using the hydrogen mixture injector is shown in figure 3.10. We find that the number of aggregates larger than 30 μm rises sharply for mixtures more concentrated than 1 $H_2$ : 5 He by volume, and that particles become vanishingly small for mixtures more dilute than 1 $H_2$ : 500 He. In the dilute limit, we do not resolve individual particles by eye, or with a camera, but only observe diffuse scattered light from a beam traversing the liquid. The liquid, prior to injection, does not visibly scatter light at the intensities we use (~100 W/cm$^2$). We find that a mixture ratio of 1 $H_2$ : 200 He is the best compromise between particle size and number, although the majority of our data was collected before this optimization was accomplished, using 1 $H_2$ : 10 He.

## 3.7 Discussion

### 3.7.1 Particle volume fraction

We estimate, based on the rate at which our bottled mixture is consumed, that a typical injection introduces about 200 cc of gas at standard temperature and pressure into the cryostat. This corresponds to about 0.2 cc of liquid helium and solid hydrogen inside the cryostat. Using our most commonly used dilution ratio of 1 $H_2$ : 10 He, the volume of solid hydrogen introduced to the channel, $V_p$, is about $10^5$ times smaller than the volume of the channel, $V_f = 625$ cc. If we assume that all of the introduced hydrogen ends up in the suspension of particles, the volume fraction of particles that results is

$$\Phi = V_p / V_f \approx 3 \times 10^{-5}, \tag{3.7.1}$$

which is small enough that the particles have a completely negligible effect on the fluid viscosity (Batchelor 1967).

### 3.7.2 Particle size

We can use the particle volume fraction, defined in section 3.7.1, to make a rough estimate of the size of the particles by counting how many particles we see in an image:

$$4\pi N_p r_c^3 / 3 = V_o \Phi, \tag{3.7.2}$$

where $N_p$ is the number of particles of characteristic radius $r_c$ in the image volume, $V_o$. If most of the volume of hydrogen injected is carried by the largest particles, which are the ones we can see and count, then our estimate is reasonable. By examining images of particles, we use $N_p = 50{,}000$, corresponding to a mean particle separation of about 4 pixels in the image, and believe this to be a conservative guess. We estimate the image volume using the image dimensions given in section 2.1.7, and the illuminating sheet

thickness given by (2.1.1). For a sheet thickness of 100 μm we find that the characteristic particle diameter is

$$2r_c = 3\ \mu\text{m}. \tag{3.7.3}$$

There could, however, be many particles of smaller size. For example, 1,000,000 invisible and uncounted 200 nm particles in the image would amount to only one-tenth the total volume of the counted particles. This is not important for PIV in general, but may be relevant to the results presented in chapter 6.

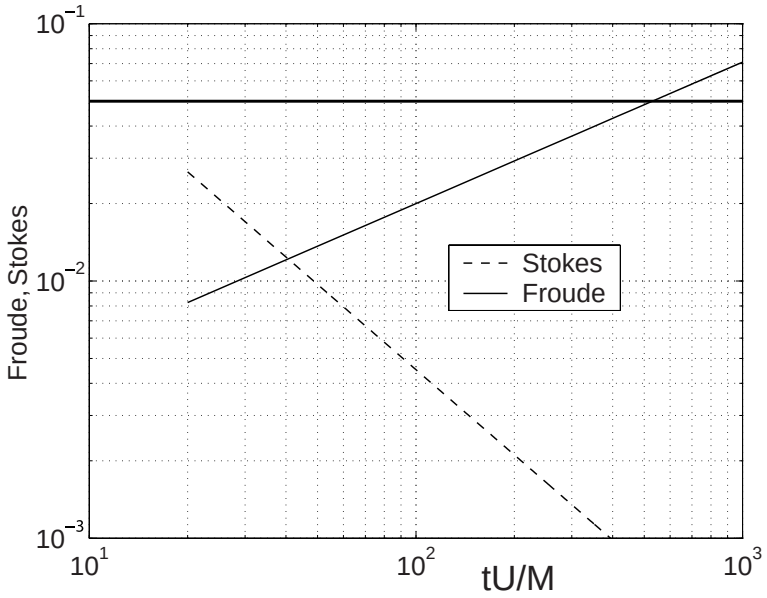


**Figure 3.11**: The chart shows the Stokes and Froude numbers as they evolve in a turbulent flow generated by a grid with 7.2 mm mesh spacing, $M$, drawn at $U$ = 2.0 m/s in liquid helium. The parameters are calculated for hydrogen particles with a diameter of 3 μm. The horizontal line is the maximum value for either parameter determined in section 3.2; note that the scale in this chart is different from in the comparable figures 3.3 and 3.6. In this example, the hydrogen particles are suitable for making quantitative measurements of local fluid velocities in the turbulent flow.

We have also obtained particle images with a long-range microscope, whose resolution is 2.7 μm/pixel. The bulk of the particles in the images cannot be distinguished from point sources of light, suggesting they are smaller than the resolution of the optical system. We show in figure 3.11 that 3 μm hydrogen particles make suitable tracers for a turbulent flow up to about 500 normalized time units.

### 3.7.3 Model of injector function

The mechanism we present by which the particles are produced is primarily conjectural, as we do not yet have a way to observe their formation, nor have we tested the conjecture. The mixture of hydrogen and helium gas cools as it descends through the injector into the cryostat. Heat is carried away through the injector walls by the cold helium gas in the cryostat, and by liquid helium at low enough levels in the injector. The mixture supercools below the condensation temperature of hydrogen until hydrogen begins to precipitate from the gaseous mixture.

The mechanism for the precipitation and freezing of hydrogen from the dilute mixture is unknown, but may, on general principle, be the result of either homogeneous nucleation, or condensation onto impurities that serve as nucleation sites. Homogeneous nucleation of binary mixtures is known to occur (Wegener & Sreenivasan 1981). At low enough temperatures, quantum tunneling may be responsible for crystallization (see Levi and Mazzarello 2001). The freezing of hydrogen is an active area of research, as some scientists hope that supercooled hydrogen droplets will remain in a metastable liquid state at low enough temperature to show superfluidity (Seidel et al. 1986). However, we

consider this outcome unlikely, as it is also possible that hydrogen forms a glass without overcoming the energy barrier associated with crystallization.

We expect a wide distribution of particle sizes since the formation of nuclei and the growth and aggregation of existing nuclei can occur simultaneously. The rate of aggregation of nuclei may be described as in section 3.3.2, and we expect that the characteristic size of particles depends inversely on the hydrogen concentration. The process of precipitation continues until the mixture reaches thermal equilibrium with the liquid helium in the bath, and the particles are dispersed in the liquid. Aggregation continues in the liquid, but under different conditions.

### 3.7.4 Practical considerations

A significant advantage of hydrogen particles is that we form them as an already dispersed suspension of small particles, so that we do not need to find a way to disperse them in the helium liquid. Any other solid particle must be introduced as a concentrated solution with the attendant problems with aggregation.

In addition, since the settling velocity of a particle is proportional to the square of its size (as shown in section 3.1), once the hydrogen particles have aggregated into particles too big to be useful, their buoyancy rapidly brings them to the free surface of the liquid, effectively removing them from the system. In this way, aggregation and buoyancy act to clean the system of particles, and we can periodically generate a fresh batch of small particles. The process of creating hydrogen particles is simple and swift, requiring little of the preparation required for other types of particles (see White 2001, Zhang et al. 2004).

Finally, aside from accurately tracing the smallest scales of the flow, the smaller particle allows us to increase the spatial resolution of our PIV processing. We can introduce a large number of particles into the fluid, and thus find a sufficient number of particles in a smaller volume to construct a velocity vector. In this way, we can acquire data at a spatial resolution two times better than previously achieved.

### 3.7.5 A note on the injection of particles into superfluid helium

In chapter 6, we describe observations of superfluid helium. We have found, however, that we cannot use our injector in the superfluid. The injector produces a vigorous jet, whose velocity cannot be accounted for by the mass flux emanating from the injector. The vigorous jet persists even as we reduce the flow rate, and the hydrogen forms large clumps rather than a fine mist. We explain in chapter 6 that the only way we find of observing the superfluid with a suspension of small particles is to generate the suspension at higher temperatures in normal helium, and then cool the helium to the desired superfluid state.

### 3.7.6 Final analysis

In table 3.1 we summarize the utility of the particles surveyed in this chapter, including the hydrogen particles we have produced. We stress that we have used what we believe is the upper bound in size for the hydrogen particles. Smaller particles will perform better. In addition, individual polystyrene particles evidently will work, provided they can be suspended in liquid helium long enough. We have not found a way to do this.

A $B$ number greater than one, listed in table 3.1, indicates that there exists a range of Reynolds numbers for which the particles will trace the flow with adequate fidelity, as described in section 3.1.2. In order to determine this range, one must specify some detail of the flow the particles must trace. The integral length scale, $l$, of the flows we observe evolves, but is typically about 0.5 cm. For a 3 μm hydrogen particle in liquid helium, the acceptable Taylor scale-based Reynolds numbers range from 145 to 590, according to (3.1.9) and (3.1.10). For 1 μm hydrogen particles, the range is from 30 to 1230. We show in chapters 4 and 5 that the Reynolds numbers of the flows we generate with a grid fall within this range.

**Table 3.1**: We list the $B$ numbers, defined in section 3.1.2, for a variety of particles in liquid helium near its boiling point. Particles that satisfy our condition that $B > 1$ are marked by a bold font. The 4 μm hollow glass particles are hypothetical – we do not know of any that are manufactured. As discussed in the text, it is unlikely that polystyrene particles can be suspended as individual particles, since they have a strong tendency to aggregate into larger clumps. Therefore, the hydrogen particles are the only particles we know of that we can use to accurately trace the motions of liquid helium.

| Particle material | diameter (μm) | density (g/cc) | $B$ |
|---|---|---|---|
| **Hollow Glass** | **4** | **0.14** | **13** |
| Hollow Glass | 9 | 0.14 | 0.5 |
| **Polystyrene sphere** | **0.8** | **1.06** | **8.5** |
| Polystyrene clump | 2.4 | 1.06 | 0.1 |
| **Hydrogen** | **3** | **0.088** | **17** |

## 3.8 Conclusions

We have shown that commercially available particles as well as those developed by our predecessors are inadequate for making precise measurements of turbulent velocities in liquid helium. We have presented a simple way of making small hydrogen particles that are likely to be small enough to make such measurements. We estimate that the particles are typically smaller than about 3 μm in diameter; further estimates of the particle size are made in chapter 6. Along the way, we find that particles have a tendency to clump that is probably insurmountable in cryogenic fluids, and that this problem is most severe at the moment of particle injection. We establish well defined limits in terms of fluid and flow properties for which particles of particular characteristics can be used.

# Chapter 4

# Decaying grid turbulence

Here we describe experiments providing an assessment of the utility of our new particles. We motivate the study of decaying grid generated turbulence without any system rotation, and describe our methods for realizing and observing the flow. Finally, we present data showing that the hydrogen tracer particles described in chapter 3 produce reliable results. We generate turbulence at $R_\lambda = 260$, which is moderate in comparison to the full range of results found in the turbulence literature, but large for grid turbulence. The turbulence decays according to expectations for high Reynolds number homogeneous and isotropic turbulence.

## 4.1 Background

### 4.1.1 Homogeneous and Isotropic Turbulence

The difficulties of predicting turbulence dynamics from the Navier-Stokes equations are well known (L'vov and Procaccia 1996). Many theoretical results were arrived at using the assumption of scale invariance for homogeneous and isotropic turbulence (e.g., Kolmogorov 1941), that is, that the statistical properties of the flow are invariant to translations and rotations of space. The assumption is usually made in

conjunction with the condition of large Reynolds number (Frisch 1995). In turbulence research, both experimental and theoretical, freely decaying homogeneous and isotropic turbulence is used as a benchmark (Batchelor 1953).

### 4.1.2 Grid Turbulence

The closest experimental approximation to homogeneous and isotropic turbulence is the disturbance caused in a fluid by the passage of a grid. Since Taylor (1935), there is a long tradition of studying grid generated turbulence, where the grid is usually constructed from crossed bars of square or round cross section (Dickey and Mellor 1980, give some examples). The flow is characterized by the grid (or flow) velocity, $U_g$, and the grid's mesh spacing, $M$. The mesh Reynolds number is defined as

$$Re_M = U_g M/\nu. \tag{4.1.1}$$

The scales $U_g$ and $M$ define the initial conditions. That is, though there is some variation in results between trials in a particular apparatus, and between those obtained using different apparatuses, most data acquired using different grids or grid velocities are seen to follow common curves when using the grid parameters to normalize measurements.

A grid will agitate a fluid in either of two basic configurations, one can move the fluid, or the grid. In the first case, the fluid is circulated with a pump, steadied, and passed through a grid. The flow evolves downstream from the grid, and measurements of the flow properties are made at different distances from the grid. At any point in space the flow is steady, measurements are made for arbitrary lengths of time, and large data sets can be easily collected. However, attempts to characterize turbulence far downstream of the grid are limited by the physical length of the test section. The second

case, the towed grid, is realized by mechanically drawing a grid through a sample of quiescent fluid. The flow is observed at varying times after the passage of the grid, and this time can be made arbitrarily large. Such an experiment has the disadvantage of requiring many trials (many repetitions of the grid movement) in order to achieve convergence in the ensemble statistics of typical flow properties.

We choose the towed grid configuration because it requires less space. It is possible to build a channel with larger cross section within the confines of a cryostat, and a larger test section translates to larger Reynolds numbers. We collect data using the PIV technique described in section 2.2, taking particle images in a plane that contains the direction of the grid motion. Velocities are measured either parallel to the grid motion, the streamwise direction, or normal to the grid motion, the transverse direction, in reference to the geometry and motion of the grid. The two components of velocity normal to the grid are expected to be indistinguishable, though it is known that there is some anisotropy in the stationary grid case when comparing streamwise and transverse statistics (Comte-Bellot and Corrsin 1966). White (2001) found that in our apparatus, using more than 20 trials yields sufficiently converged mean square velocities.

### 4.1.3 Theoretical predictions of the decay rate

Though we know of no solutions that follow directly from the Navier-Stokes equations, several models for describing the decay rate of homogeneous and isotropic turbulence are outlined below. In most cases, the kinetic energy is predicted to decay in time as a power law,

$$\boldsymbol{u}^2 \sim t^{-n}. \tag{4.1.2}$$

All theories presented here are intended to describe the decay of turbulence when the energy containing scales of motion are much smaller than the system size. Once the large scales sense boundaries, other decay rates will occur (Batchelor 1953).

Kolmogorov suggested a law for the kinetic energy in a homogeneous and isotropic flow that is allowed to decay freely from a high-Reynolds-number turbulent state (see Frisch 1995). The derivation of the law is based on Kolmogorov's vision of the energy spectrum in the inertial range, the intermediate range of scales, whose spectral intensity is proportional to $\varepsilon^{2/3}k^{-5/3}$, where $k$ is the inverse of the flow scale, or the wavenumber. The energy in the smallest wavenumbers, those between zero and the dominant energy containing scales, is assumed not to change with time. Kolmogorov used a form for the spectrum in this regime proportional to $k^4$. The total kinetic energy is found by integrating the energy spectrum over all scales, resulting in a differential equation whose solution gives the time dependence for the energy, with $n = 10/7 \approx 1.4$. However, the $k^4$ behavior has since been thought to be incorrect.

Versions of Kolmogorov's calculation are still widely used (e.g., Stalp et al. 1999), and all show sensitivity to the behavior of the largest length scales. For example, a popular derivation uses a $k^2$ spectrum at low wavenumbers (Saffman 1967), yielding a decay exponent $n = 6/5$. According to the assumptions of this derivation, energy decaying as the inverse of time implies a linear small wavenumber spectrum. However, we consider the dependence of the decay rate on the small wavenumbers to be an indication that the decay law may depend on initial and boundary conditions in any experiment, even when the energy containing scales are much smaller than the domain

size. This is because the largest scales of motion will be constrained in their evolution by the size and shape of the container, dictating the form of the small wavenumber spectrum.

It is enticing to seek a solution that is independent of initial and boundary conditions and is asymptotically approached in the limit of large Reynolds number. A result is derived from von Kármán and Howarth's (1938) expression for the propagation of the correlation function in homogeneous and isotropic turbulence, into which Lin (1948) substitutes Kolmogorov's expressions for the correlation functions at high Reynolds numbers. The resulting solution for the kinetic energy, $u^2$,

$$u^2 - \beta \sim (t - t_0)^{-1}, \tag{4.1.3}$$

is seen to decay inversely with time when $u^2$ and $t$ are each bigger than certain unknown constants, $\beta$ and $t_0$, respectively. We explore this limit in section 4.3.5.

### 4.1.4 Experimental observations

A large number of experiments have been performed to study the decay of grid-generated turbulence. Many of these results are collected by Mohamed and LaRue (1990), who find that the average decay exponent for all experiments is $n = 1.3$, with deviations in either direction of 0.1. However, these results are for low values of the mesh Reynolds numbers of between 6,000 and 68,000. We know of no experiments at high Reynolds numbers comparable to the ones we reach (290,000) where the decay exponent was definitively established. Kistler and Vrebalovich (1966) collect data at $Re_M = 10^6$, but do not examine a large enough range of the energy decay to estimate the exponent of a power law fit, as in (4.1.2).

## 4.2 Methods

### 4.2.1 Protocol

Data are typically gathered in the following manner. The grid is initially placed in the lower part of the channel, below the windows, and the laser beam is blocked from entering the cryostat by a pivoting mirror which directs the beam into a beam dump. Hydrogen particles are introduced, as in chapter 3. The liquid helium reservoir and channel are sealed by closing a valve, and over the course of each trial, evaporation of the helium inside raises the internal pressure by 7 to 30 kPa. After particle injection, the experiment is controlled by the programmable linear motor controller, which directs the following actions. The particles are allowed to disperse and the fluid is allowed to settle for one minute. Just after the grid is drawn vertically through the liquid, the pivoting mirror moves and gives the laser beam free passage into the cryostat, illuminating the camera's image plane. The camera trigger control computer is instructed to begin triggering the camera according to a programmed timing sequence, as discussed in section 4.2.2. Once the camera's memory is full, the laser beam is again blocked from entering the cryostat, and the grid is brought to its original position. This completes the action of the linear motor program. The pressure in the cryostat is allowed to vent, and the movie is downloaded from the camera to a computer where it is analyzed with a PIV algorithm reviewed in chapter 2. During this time, the hydrogen particles float to the surface of the channel over a period of tens of minutes, as discussed in section 3.7.4. Once the volume of the channel is free of particles, the procedure is repeated from the beginning.

### 4.2.2 Image timing

In each trial, images are taken with the high speed camera at a series of times, in packets. In other words, we force the camera to acquire frames irregularly by driving its frame trigger with a computer, as described in section 2.1.7. As illustrated in figure 4.1, a small number of images, usually five, are recorded with enough time between each frame to allow the particles to move just a few pixels in the image, this being a packet. Then the camera waits, and captures another packet of five closely spaced images. Within each packet, images are taken with a period between them roughly five times smaller than the Kolmogorov time scale defined by (3.1.5). The inter-packet time is usually about equal to the Kolmogorov time scale. Both of these times are set by empirical optimization. These time scales are found to grow with time after the grid has passed, which is consistent with the nature of decaying turbulence. The triggering procedure is designed to maximize the time span of the energy decay we observe using as few frames as possible, and also to maximize the quality of the data. Within each packet, PIV analysis is performed on pairs of temporally adjacent images.

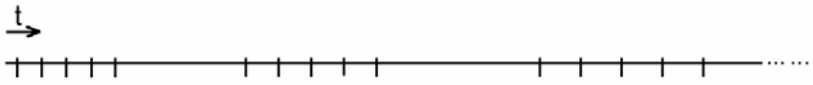


**Figure 4.1**: Images are taken at each tick mark. Each set of five ticks is called a packet, and the image frames are equispaced in time within each packet. We program the time between frames within each packet, and the time between packets, to grow larger as the turbulent velocities decay, such that the particles move a constant distance between images in a packet.

## 4.3 PIV measurements using hydrogen particles

As validation for the utility of our new hydrogen particles in liquid helium, we observe the decay of turbulence behind a towed grid, without system rotation, and compare the results to expectations. Data are collected for a series of times between 0.11 and 3.7 seconds after the grid has passed. The collection of trials, $N = 23$ in total, are for fixed grid velocity, $U_g = 1.0$ m/s, and for a single grid geometry with mesh spacing, $M = 7.2$ mm. These values correspond to non-dimensional times, $t_M = t\, U_g / M$, between 16 and 512, and to a mesh Reynolds number, $Re_M$, of 283,000.

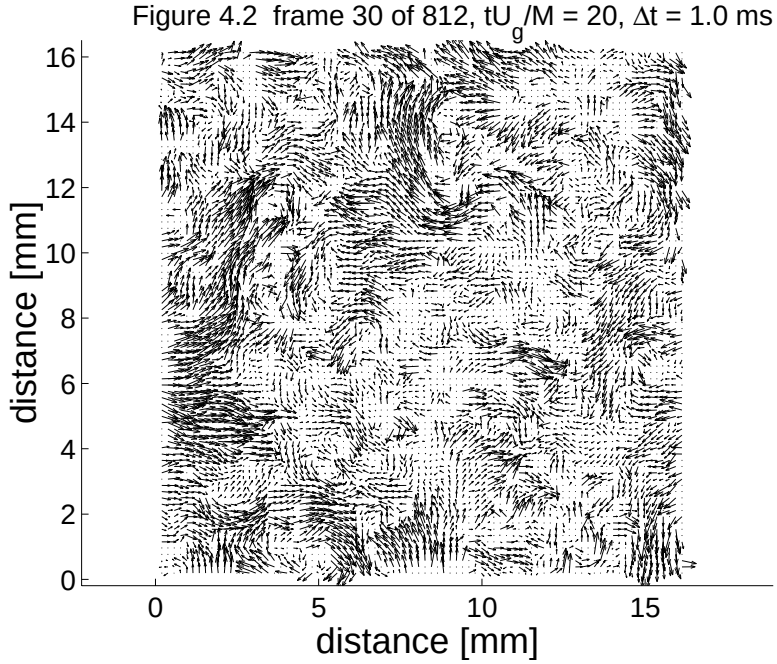


**Figure 4.2**: PIV vectors computed from two images taken 1 ms apart about 140 ms after the grid has passed the field of view at 1.0 m/s. Processing on images of hydrogen particles is done according to the description in section 2.2, with an interrogation area size of 24 × 24 pixels in the final pass.

### 4.3.1 PIV Data

We extract PIV vector fields with 84×84 vector resolution using 24×24 pixel interrogation windows from the 1024×1024 pixel images covering a region of the flow 1.6×1.6 cm in area. The images, after processing with our PIV algorithm (see section 2.2), usually yield a vector for 90% of the interrogation windows. In other words, 10% of the vectors either could not be extracted from the image data and are missing, or were judged spurious and removed.

### 4.3.2 Mean Flow

In addition to stochastic turbulent motions, a grid drawn through a channel invariably generates a repeatable large scale flow, of a form illustrated in figure 4.3. The energy in the container-sized flow must be small compared to that in the turbulent motions in order that the turbulence be approximately homogeneous and evolve locally and independently of the effects of the boundary. In our small sampling area in the center of the channel, the large scale flow displays itself roughly as a mean flow, where the mean is taken over the whole observed area at each point in time as follows:

$$\boldsymbol{u}_{\mathrm{mn}}(t) = \Sigma\langle \boldsymbol{u}(\boldsymbol{r}, t)\rangle / N. \qquad (4.3.1)$$

Here, the brackets indicate an ensemble average taken over all points in space at one particular instant in time, and the sum is taken over the $N$ independent realizations of the experiment.

We find that in the apparatus's initial configuration, the flow at the center of the channel is consistently in the direction of the grid motion, and bears energy comparable to the turbulent fluctuations. After testing several possible sources for this current, by

addressing each with a likely solution, we have succeeded in controlling the mean flow. We used liquid nitrogen in our optimization of the grid geometry, since each modification of the grid required disassembly of the cryostat. It is easier and faster to cycle liquid nitrogen, and we find that the solution also works in liquid helium.

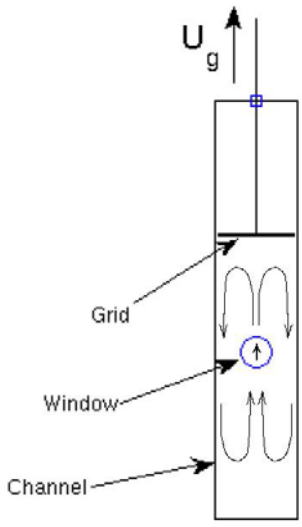


**Figure 4.3**: A cross section of the channel, and a sketch of the large scale flow the grid generates as it is towed along the length of the channel. In the area we observe through the window, the flow appears uniform, though it must recirculate down the sides of the channel.

We initially suspected that the wake of the grid stem, fixed to the center of the grid, caused the mean current. We therefore constructed a grid drawn from its corners, but found that the flow velocity was reduced by only 10 to 20%. We also tested whether the recessed cryostat windows interfered with the regular development of the wake of the grid in its progression up the channel. Vortices from fluids escaping around the grid are consistent with the observed current – the grid could conceivably form some channel-sized eddies as its edge temporarily passed an opening. We machined new windows from acrylic whose inside surfaces are within 0.6 mm of the channel wall, as shown in

figure 4.4. The original windows were simple flats and recessed by 5 mm. The grid was drawn by a rod from its center, as it was originally. The results of these trials are shown in figure 4.5.

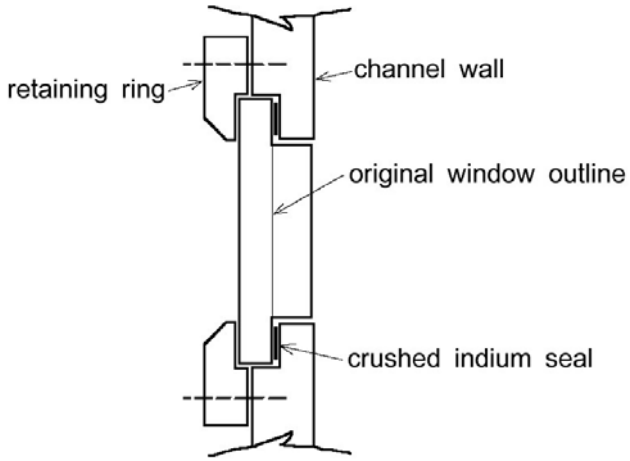


**Figure 4.4**: A sketch of one of four flush-fitting windows in the side walls of the channel. The window aperture is 2.5 cm. The fine line traces the outline of the original flat windows. The grid passes on the right in this drawing, and the vacuum space is on the left. The vacuum seal is formed by crushing an indium wire between the window and the channel wall.

We found that flush-fitting windows exacerbated the problem. The mean flow in the direction of the grid motion was initially of the same strength, but decayed more slowly than the mean flow in the original configuration. We conclude that the recessed windows have little to do with the generation of the mean flow. Although we seek to minimize the mean flow, the fact that recessed windows have an effect at all suggests that we should use flush-fitting windows. If the shape of the container is important, our goal is to collect data in the simplest geometry possible. We performed the remainder of our experiments in this thesis with flush-fitting windows, machined from sapphire according to the sketch shown in figure 4.4.

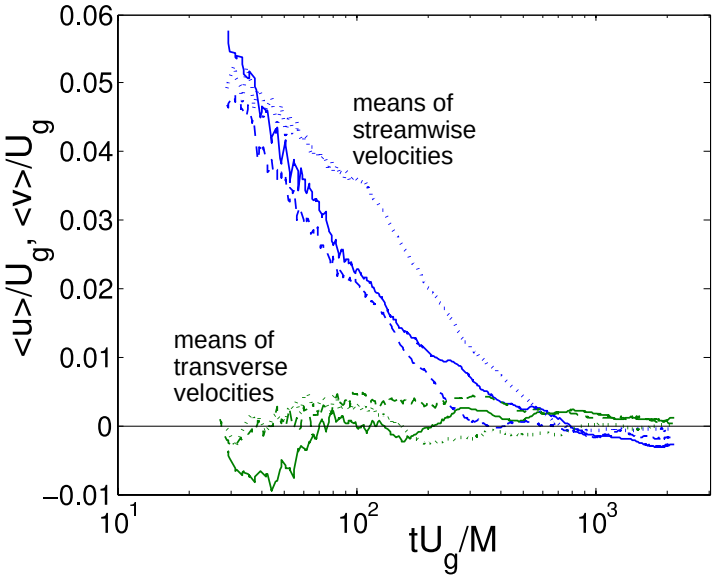


**Figure 4.5**: The mean flow as a fraction of the grid velocity, $U_g$, using liquid nitrogen in the channel, and using different grid designs. The solid lines are the for the grid in its original configuration, drawn from its center by a rod, the dashed lines are for the grid drawn from its corners, and the dotted lines are for the original configuration, but with flush fitting windows. The strength of the flows is comparable despite the modifications.

We discovered that the source of the current is at the interface between the edge of the grid and the wall. The wall and an associated boundary layer disrupt the translational symmetry of a grid, and the long range of the pressure force causes the disturbance to influence the flow across the whole channel. In other words, fluid leaks around the edge of the grid and rushes down near the wall, driving an upward recirculation in the center of the channel. We control the behavior, and minimize the flow, by placing a wire of the right diameter, 0.33 mm, around the perimeter of the grid. The minimized mean flow is shown in figure 4.6. We will see in section 4.3.3 that the mean flow is made significantly smaller than the RMS velocity of the turbulent fluctuations by this solution. An interesting way to interpret this is that an addition to the

frontal area of the grid has resulted in a decrease of its total drag. This type of counterintuitive phenomena is not uncommon in fluid dynamics (see, e.g., Strykowski and Sreenivasan 1990).

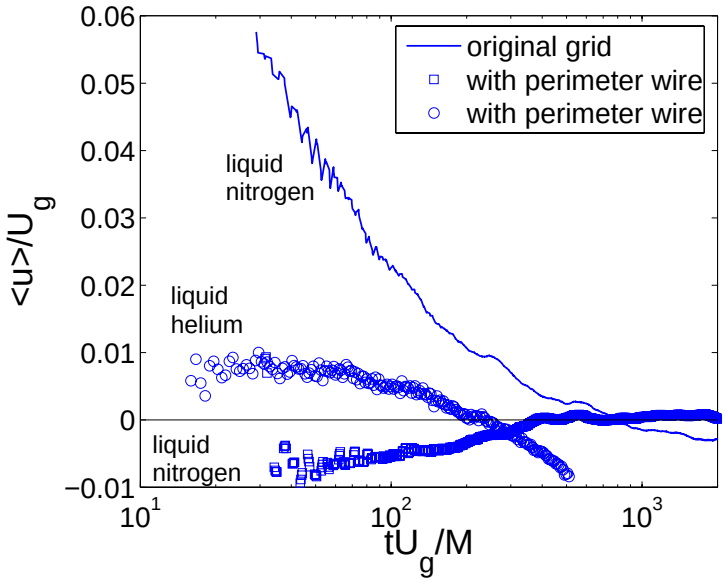


**Figure 4.6**: The streamwise mean flow with a 0.33 mm wire around the perimeter of the grid, in both liquid nitrogen and helium. The transverse mean flow remains largely unchanged, is always smaller than 1% of the grid velocity, and is not shown.

### 4.3.3 Turbulent energy decay

We find that the total kinetic energy in the turbulent fluctuations decays with time as a power law with exponent $n \approx 1$. The 5% difference between our exponent and 1.0 is probably attributable to lack of convergence of our data to the mean. The total kinetic energy per unit mass is computed for $N = 23$ trials as follows:

$$E(t) = \tfrac{1}{2}(u^2 + 2\,v^2) \tag{4.3.2}$$

$$u^2(t) = \Sigma\langle u^2(\boldsymbol{r}, t)\rangle / N \tag{4.3.3}$$

$$v^2(t) = \Sigma\langle v^2(\boldsymbol{r}, t)\rangle / N \tag{4.3.4}$$

Here, the notation is as in the previous section, and the data are plotted in figure 4.7.

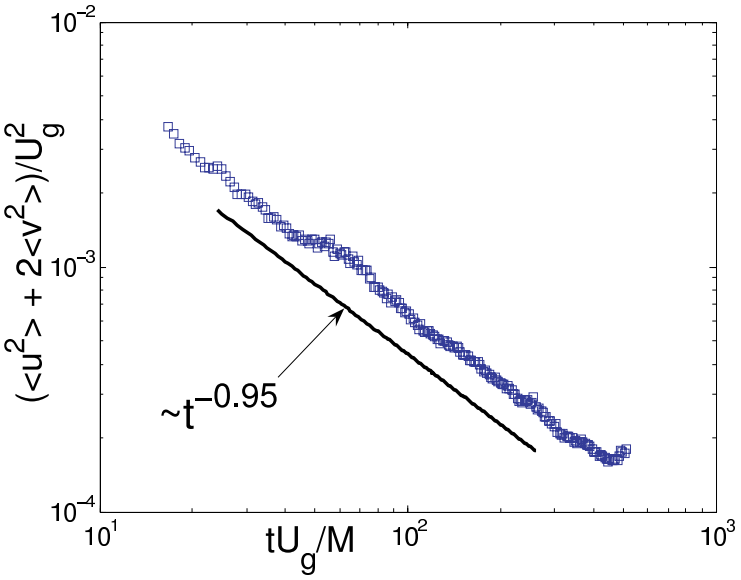


**Figure 4.7**: The decay of kinetic energy per unit mass in the flow generated by a grid passing through liquid helium as a function of time since the grid has passed. Variables are normalized by the grid parameters, the grid velocity, $U_g = 1.0$ m/s, and the mesh spacing, $M = 7.2$ mm. The fit is to a power law as in (4.1.3) with β and $t_0$ set to zero.

With this result, we calculate the Taylor based Reynolds number,

$$Re_\lambda = \lambda u/\nu = u^2 (15/\nu\varepsilon)^{1/2}, \tag{4.3.5}$$

where the energy dissipation rate, $\varepsilon = -dE/dt$, is computed from the derivative of a power law fit to the data for the decay of the total kinetic energy given by (4.3.2). We find that the average $Re_\lambda$ is 260, and does not show an increasing or decreasing trend with time as expected of a flow with energy decaying as $t^{-1}$. Its value fluctuates by about 10% over the observed time span.

### 4.3.4 The strength of the mean flow

We show that the energy of the mean flow is smaller than fluctuations by a factor of more than 10 for most of the decay (figure 4.8). This corresponds to a fluctuating

velocity about three times larger than the mean. Later in the decay, we begin to see the effect of convection caused by laser heating of the windows, as discussed in section 4.3.4.

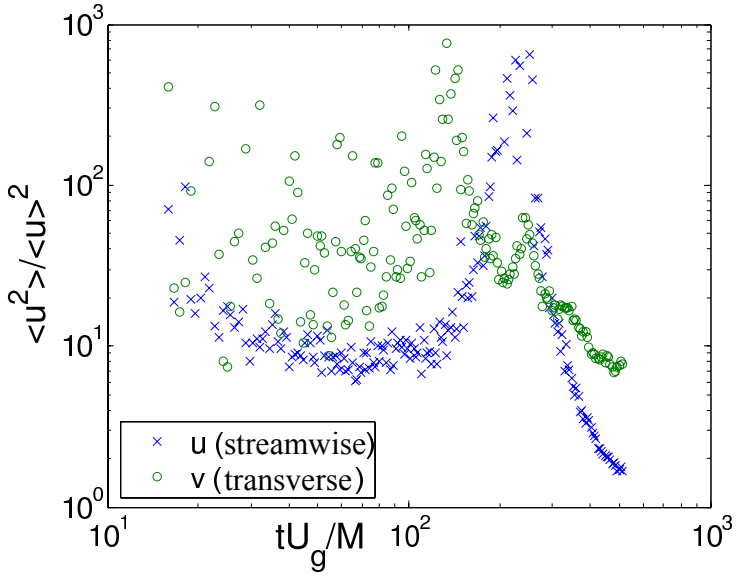


**Figure 4.8**: The fluctuating energy relative to the energy in the mean for the same flow as in figure 4.7. The streamwise fluctuations are compared to the streamwise mean, and the transverse fluctuations are compared to the transverse mean.

### 4.3.5 A comment on the magnitude of the observed variables

The constants β and $t_0$ in (4.1.3) are not constrained by Lin's theory, nor is it clear what they physically represent. In order for Lin's decay law to resemble the one we have found, $u$ and $t$ as observed in our experiment must be large relative to the constants. We offer here the suggestion that both $u$ and $t$ are indeed large when compared with physical scales.

As turbulence decays, $u^2$ is damped and approaches β while $t$ eventually grows larger than $t_0$. As long as our assumption of large Reynolds number holds, the relevant scales are the root mean square flow velocity, $u$, and the integral scale, comparable to $M$. The velocity $u$ scales with the grid velocity, $U_g$, so we can measure the distance from the

time origin in terms of the quantity $M/U_g$. We show above that we do observe turbulence at large times in this sense. Furthermore, as the turbulence evolves, the Reynolds number becomes smaller until viscosity affects the large scales, and a new decay law must be derived. The viscosity-dependent velocity scale is the Kolmogorov velocity, given by (3.1.6), and we may relate β to the square of this quantity. The degree to which the kinetic energy in the flow is larger than this value is then found to be the Taylor based Reynolds number given in (4.3.5):

$$u^2/u_{fluid}^2 = Re_\lambda/15^{1/2} \approx 67. \qquad (4.3.6)$$

This suggests that β may become unimportant for large enough $Re_\lambda$. We have assumed that both β and $t_0$ are equal to zero in finding that our data fit a power law.

### 4.3.6 A note on thermal input

The upturn in energy at the largest times seen in figure 4.7 is the beginning of a trend that continues at larger times than we have captured in this data set. The feature is related to a steadily decreasing streamwise mean flow, as shown in figure 4.6. The mean flow reverses direction at about $t_M = 200$, and continues growing in the opposite direction, which is downward against gravity. As can be seen in figure 4.8, this mean flow gains in strength relative to the turbulent fluctuations, and is comparable to them above $t_M = 400$. The mechanism driving the flow at late times is convection. The laser beam impinging on the windows adds a small amount of heat at their surfaces and causes fluid to rise along the boundaries. The fluid recirculates at the center of the channel, where we make our observations. This problem is inevitable when using liquid helium, since its thermal expansion coefficient is large, about 1000 times larger than that of

water, for example. The problem is exacerbated by using continuous illumination, as we do. However, we have confined our observations to the region before this convective flow is comparable in strength to the turbulence generated by the grid.

## 4.4 Conclusions

We find that the hydrogen particles introduced in chapter 3 produce PIV data of high quality. We observe that turbulence generated by a towed grid is sensitive to grid geometry. We find that turbulence kinetic energy decays with a power law, as predicted by theory about homogeneous and isotropic turbulence. In addition, the exponent of the decay we measure, −1, is comparable to the one found in previous experiments (surveyed in section 4.1.4). However, its slightly less rapid decay may be attributable to the larger Reynolds number of the flow; the decay rate is a special case of a prediction for high Reynolds number turbulence. We recognize, however, that further experiments are necessary for strong conclusions about turbulence.

# Chapter 5

# Turbulence in a rotating container

We attempt to generate homogeneous turbulence in a steadily rotating system. Our goal is to observe fully developed turbulence in a system that is rotating rapidly, in a sense that we clarify below. We cause turbulence using a grid in rotating channels with both square and round cross sections using liquid helium, liquid nitrogen, and water as test fluids. We are not able to approximate homogeneity in our rotating apparatus, and argue that it is difficult in any real system due to the presence of large scale inertial waves in the body of the fluid. These inertial waves quickly sense the boundaries, and resonate at frequencies characteristic of the shape of the volume.

## 5.1 Rotating flows

Rotating flows are common in engineering and planetary settings. Rotation controls the behavior of geophysical flows, such as in oceans and the molten outer core of the planet (Buffet 2000). Flows in rotating machinery, such as turbines, also experience effects of rotation. In these applications, as in most, the effect of rotation is compounded by other mechanisms, such as convection. Here, we study the effect of rotation alone. There has also been some interest in arriving at a better understanding of energy

dissipation in non-rotating turbulence through an understanding of how system rotation interferes with the mechanism of energy transfer among scales of motion (Cambon et al. 1997). Because of these two approaches, the effect of rotation on fluid dynamics has been studied in usually one of two contexts. The geophysics community, motivated by observations of large scale flows, such as the Gulf Stream, is usually interested in constructing steady state flows exhibiting some large scale phenomena (e.g., McEwan 1970). Taking the perspective of turbulence, other experimentalists have sought to generate a stochastic state comparable to the homogeneous one that was theoretically fruitful in an inertial frame of reference (e.g., Jacquin et al. 1990). We present an attempt to reconcile the efforts of these two branches of study.

### 5.1.1 The Coriolis acceleration and its effects

The Coriolis term appears when the momentum equation is written, for normalized variables, in a steadily rotating frame of reference, as

$$\partial \boldsymbol{u}/\partial t + \boldsymbol{u}\cdot\nabla\boldsymbol{u} + 2\hat{\boldsymbol{\Omega}} \times \boldsymbol{u} / Ro = -\nabla P + \nabla^2 \boldsymbol{u} / Re. \qquad (5.1.1)$$

Here, variables are normalized as in chapter 1, except for the additional steady system rotation vector, $\hat{\boldsymbol{\Omega}}$, which is normalized by its magnitude, $\Omega$. This normalization yields the definition for the Rossby number,

$$Ro = U/\Omega L, \qquad (5.1.2)$$

for some characteristic velocity and length scales of the flow, $U$ and $L$. Just as the Reynolds number measures the relative importance of inertial to viscous terms in the equation, so the Rossby number measures the relative importance of the inertial term to the Coriolis term. Specifically, the Coriolis force acts on each fluid parcel in a direction

normal to the plane containing the rotation axis and the direction of the parcel's motion. The reader can consult Batchelor (1967) for a more complete description of Coriolis effects. Our interest is in the opposite extremes of each parameter. That is, we seek to observe a flow with large Reynolds number, in which vigorous turbulence is the dominant characteristic, and small Rossby number where rotation strongly modifies the flow. Finally, we note that the action of the Coriolis can be characterized by the Ekman number, which is the ratio of the Rossby number to the Reynolds number, and indicates how long a disturbance will survive before being damped by viscosity.

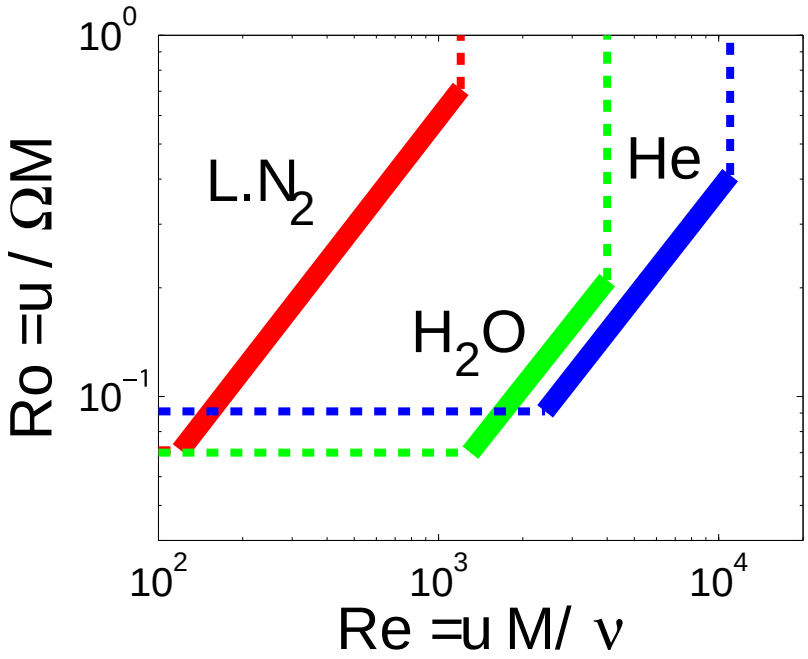


**Figure 5.1**: The Reynolds-Rossby number parameter plane using the large scales of the flow, such that $Ro = u/\Omega L$, and $Re = uL/\nu$, showing the limits in each parameter we can achieve simultaneously using our apparatus. Here, the variable $u$ is the root-mean-square flow velocity, and $L$ is the characteristic size of the energy-containing scales, which (for convenience) we take to be the mesh spacing of the grid, $M$. The bold lines are trajectories taken from data presented in this chapter, but any combination of larger Rossby number and smaller Reynolds number can be achieved by choosing appropriate initial conditions. Time progresses from the top right of each bold line to the bottom left.

### 5.1.2 The parameter space investigated

We chart the extremes in the dimensionless parameters attainable in our system in figure 5.1. Note that the Ekman number, defined in the previous section, is roughly constant with time in each experiment, and ranges from $8 \times 10^{-4}$ for liquid nitrogen to $4 \times 10^{-5}$ for liquid helium. The parameter space we explore is bounded by the rotation rate of the channel, and the maximum velocity of the grid. In addition, the system is defined by the geometry of the channel and the choice of fluid; these will be described in greater detail in section 5.3. In this section, it suffices to say that the vessels containing both the cryogenic fluids and water were designed to fit within the same outer diameter. However, because layers of thermal insulation surround the channel in the cryostat, the channel bearing cryogenic fluids is about 5 times smaller than the one containing water. In this way, we have a practical comparison of each fluid, and we argue that the contrasts are intrinsic in the choice of fluid.

We call attention to some of the advantages and disadvantages of using each fluid, as is evident in figure 5.1. Despite the smaller size of the channel containing the cryogenic fluids, we generate Reynolds numbers in liquid helium more than twice those in water. However, because the Rossby number does not depend on viscosity, flows in the larger water channel are more strongly affected by rotation.

### 5.1.3 Two-dimensional flows

In the limit of small Rossby number and large Reynolds number, one might choose to neglect most terms of the momentum equation (5.1.1), and balance the Coriolis term by pressure alone, as

$$2\hat{\boldsymbol{\Omega}} \times \boldsymbol{u} / Ro = -\nabla P. \qquad (5.1.3)$$

By taking the curl of this relation, we eliminate pressure, and the equation reduces to $\hat{\boldsymbol{\Omega}} \cdot \nabla \boldsymbol{u} = 0$, or for rotation about the vertical axis, $\hat{\boldsymbol{\Omega}} = \hat{\mathbf{e}}_z$, without loss of generality,

$$\partial \boldsymbol{u} / \partial z = 0. \tag{5.1.4}$$

The result is the Taylor-Proudman theorem (Chandrasekhar 1961) and confines spatial structure of the velocity field to the plane normal to the axis of rotation in the limit of rapid rotation. The theorem leads to the suggestion that turbulent flows tend to become two dimensional as the rotation rate is increased, as has been observed in several experiments (e.g., Baroud et al. 2003).

### 5.1.4 Inertial waves

According to Smith and Lee (2005), the tendency toward two-dimensionality is not the complete picture, even as a basic description of an unsteady rotating flow. We can see why if we retain the time dependence of velocity in the equations of motion, but again invoke a small Rossby number to justify abandonment of the inertial and viscous terms. As in section 5.1.2, we take the curl of the resultant inviscid and linear equation, and for un-normalized variables, we find that

$$\partial \boldsymbol{\omega} / \partial t + \boldsymbol{\Omega} \cdot \nabla \boldsymbol{u} = 0. \tag{5.1.5}$$

Here, $\boldsymbol{\omega} = \nabla \times \boldsymbol{u}$ is the vorticity. This equation admits plane wave solutions of the form $\boldsymbol{u} = \boldsymbol{u}_o e^{i(\boldsymbol{k} \cdot \boldsymbol{r} - \lambda t)}$. The scalar $\lambda$ is the frequency of the wave, which has the peculiar dispersion relation

$$\lambda = 2\boldsymbol{\Omega} \cdot \boldsymbol{k} / k, \tag{5.1.6}$$

where $\boldsymbol{k}$ is the wave-number vector with magnitude $k$. Note that the angular frequency of the wave is always less than twice the rotation rate, and approaches zero as the wave

vector is turned perpendicular to the rotation axis. The existence of a wave motion in the fluid's bulk implies that the Coriolis force can be thought of as a restoring force. The direction and speed of energy propagation by the wave is defined by the group velocity, which is the gradient of the frequency with respect to the wave vector:

$$\boldsymbol{c}_g = \nabla_k \lambda = 2\,\boldsymbol{k} \times (\boldsymbol{\Omega} \times \boldsymbol{k}) / k^3. \qquad (5.1.7)$$

Energy is propagated in the plane of the rotation axis and wave vector, but normal to the wave vector. No energy is propagated normal to the axis of rotation, since the direction of this wave is aligned with the axis of rotation and their cross product is zero. Conversely, energy is most rapidly transmitted along the axis. These waves are transverse, circularly polarized, dispersive, anisotropic, and in general also dissipative. More general introductions to rotating flows and inertial waves can be found in Greenspan (1968), Chandrasekhar (1961) and Batchelor (1967).

### 5.1.5 Inertial wave modes of a container

We expect from systems such as a vibrating string, that if we excite inertial waves in a fluid confined by some boundary, we will find that their wavelengths are commensurate with the size of the boundary. These resonances have been derived analytically only for an inviscid fluid confined in simple geometries, such as a sphere. Lord Kelvin found, in 1880, the modes of a cylinder with circular cross section, which are the closest analytical solutions to our own square cylinder geometry. The modes for a channel with radius $b$ and length $h$ are described in Batchelor (1967), who shows that the natural frequencies for small oscillations are:

$$\beta(m, n) = 2\Omega / (1 + (\gamma_n h / \pi m b)^2)^{1/2} \qquad (5.1.8)$$

Here, $m$ is the axial wave number, $n$ is the radial wave number, and $\gamma_n$ is the location of the $n$th zero of the Bessel function of the first kind.

For a square channel, such as the one in our cryostat, there exist no analytical solutions. However, Maas (2003) devised a computer solution to the problem. The frequencies of standing waves modes in a channel with our aspect ratio were communicated to us privately by Maas (2005), and are presented in table 5.1.

**Table 5.1**: Numerical results from Maas (2005) for the modes in a square channel with aspect ratio $h/2b = 5$. The numbers are the frequencies of the modes relative to the inertial frequency, or $\omega_M/2\Omega$. The first pair of rows is the symmetric and asymmetric modes, as defined by Maas (2003), with varying axial wavenumber, and transverse wavenumber equal to one. The second pair of rows is for modes with the same axial wavenumbers and a transverse wavenumber of two.

| axial wavenumber: | 1 | 2 | 3 | 4 | 5 | 6 | 7 | 8 |
|---|---|---|---|---|---|---|---|---|
| transverse wavenumber = 1: | | | | | | | | |
| symmetric mode: | 0.0921 | 0.182 | 0.267 | 0.346 | 0.418 | 0.483 | 0.540 | 0.590 |
| asymmetric mode: | 0.0988 | 0.215 | 0.336 | 0.450 | 0.547 | 0.626 | 0.689 | 0.740 |
| transverse wavenumber = 2: | | | | | | | | |
| symmetric mode: | 0.0713 | 0.145 | 0.221 | 0.296 | 0.369 | 0.437 | 0.450 | 0.556 |
| asymmetric mode: | 0.0821 | 0.154 | 0.220 | 0.283 | 0.341 | 0.396 | 0.447 | 0.495 |

### 5.1.6 Reflecting inertial waves

An alternate view of inertial waves confined in a volume is adopted by most experimentalists and theorists. It is imagined that scattered inertial waves of arbitrary frequency bounce off the container's walls and reverberate, like sound in a large room. This view originates with Phillips (1963), who finds that the reflection of an inertial wave from a surface changes the wavenumber of the wave, depending on the reflection angle

and angle of the surface relative to the rotation axis. Inertial wave reflections then have the effect of redistributing energy amongst the scales of motion. In addition, some energy is dissipated in boundary layers.

### 5.1.7 Rotating, decaying homogeneous turbulence

The nonlinear term in the Navier Stokes equation is responsible for redistributing energy among different scales of motion, and it is this redistribution that eventually causes energy to be dissipated by the small scales (Frisch 1995). Because a small Rossby number implies that the nonlinear term is less dominant than the (linear) Coriolis term, it is thought that strong rotation diminishes the dissipation rate. In addition, it is found that in two-dimensional turbulence, which is treated as a limiting case, energy can be transferred to increasingly large scales of motion (Kraichnan 1967). At progressively larger scales, viscosity dissipates energy less and less effectively. For these reasons, it is thought that rotating turbulence will decay less rapidly than stationary turbulence, whose decay rate we discussed in chapter 4. Rotating turbulence can also be viewed as the superposition of inertial waves interacting through the weak nonlinear term (Smith et al. 1996). These features have incited efforts to observe and understand the effect of rotation on the rate of decay of turbulence.

## 5.2 Previous experimental work

Although the effects of rotation have been investigated extensively by geophysicists, comparatively little experimental work has been done in a general setting of turbulence research. We present two examples of experiments guided by

geophysicists in which standing inertial waves were studied, followed by a review of all experiments that we know of conducted in the tradition of turbulence studies.

Fultz (1959) experimentally demonstrated the existence of resonant modes with the frequencies found by Kelvin (5.1.8) in a cylindrical tank periodically forced at a series of specific frequencies. More recently, inertial wave behavior in containers with diverse geometries has been sought. An example is Manders and Maas (2003), who examine the focusing of inertial waves in a rectangular channel with one sloping wall.

An early attempt to study rotating turbulence was undertaken by Ibbetson and Tritton (1974). In an annulus rotating about its symmetry axis, they examined the turbulence generated by the separation of plates with holes in them, a sort of high solidity grid. Velocities were measured using a hot wire that was periodically sampled. The effect was to produce data at a small number of widely spaced times. They observed an increase in the decay rate of velocity fluctuations with increasing rotation rate, and proposed that this was due to the transmission of energy to dissipative boundary layer by inertial waves. They suggest the parameter

$$J = Wu / l(\Omega\nu)^{1/2}. \qquad (5.2.1)$$

When J >> 1, boundary dissipation is unimportant relative to dissipation in the bulk. The variable $W$ is the overall size of the container, and $l$ and $u$ are the large length and velocity scales of the flow. They find $J$ to be of order 10 in their flow, and suggest that future experiments should be designed for much larger values in order for boundary layer dissipation to be unimportant.

In the most notable experimental study of the effect of rotation on decaying grid turbulence, data were collected in a wind tunnel with a rotating section (Jacquin et al.

1990). The investigators sampled the fluctuating velocity, using a hot wire, at a series of points downstream of the grid, and examined quantities such as the kinetic energy and integral length scale. They found that the energy decay rate decreased with increasing rotation rate. Using Ibbetson and Tritton's rationale regarding inertial waves, they found that the parameter $J$ defined in (5.2.1) is of order 100 in their flow, 10 times larger than in Ibbetson and Triton's flow. They argued that the reason energy decayed more slowly in their rotating experiment, while Ibbetson and Tritton measured an increased decay rate, is due to the larger value of $J$ in their flow, and that their experiment is therefore better representative of decaying homogeneous turbulence.

Dalziel (1992) towed a grid through a channel filled with water with a free surface. The grid was towed along the channel, in a direction normal to the axis of rotation. He used PIV to observe that the energy decay was unchanged, but found signatures in the signal that he guessed were surface waves and inertial waves. This is the only experiment to measure the velocity continuously in a manner analogous to our own method.

Two experiments used a rotating cylindrical water tank, and reported the observation of vortices aligned with the axis of rotation. Hopfinger et al. (1982) generated a steady state flow with an oscillating grid and used streak photography to characterize it. Morize et al. (2005) tow the grid and take instantaneous snapshots of the transient flow using PIV in the plane normal to the axis of rotation.

Most recently, Moisy et al. (2006) present an experiment conceptually similar to our own, using PIV to study turbulence behind a towed grid in a rotating rectangular tank filled with water. They report a reduction in the energy decay rate as the rotation rate is

increased. However, their decay law for decreasing rotation rate appears to approach a $t^{-2}$ form markedly different than the one expected for non-rotating homogeneous and isotropic turbulence (see chapter 4) far from boundaries, indicating that their turbulence is probably evolving under different conditions than the ones we seek to achieve. They do not comment on the influence of inertial waves.

In summary, there is no clear consensus in the literature on the effect of rotation on the decay rate of turbulence in experiments. In addition, previous experimentalists have either considered inertial waves to be a problem that needs to be controlled, or have been concerned with energy dissipation at the boundaries due to inertial wave reflections. Our approach is to consider how the structure and evolution of the flow is altered by the discretization of available wave modes.

## 5.3 Apparatus and methods

We acquire the data presented in this chapter while rotating the channel about the same axis as that of the grid motion; for this reason we use the descriptions 'axial' and 'streamwise' interchangeably. In addition to the apparatus and methods described in chapters 2 and 3, we also use liquid nitrogen as a working fluid, and a new water apparatus. Much data are acquired using liquid nitrogen, because it requires much less attention than liquid helium, allowing us to concentrate on refining the rotating apparatus and understanding the flow. Water is used because a channel with circular cross section can more easily be constructed for this fluid than for the cryogenic fluids. For water, construction of the apparatus and collection of data were accomplished in several weeks, whereas the same process took years using the cryogenic fluids.

### 5.3.1 Experimental protocol for the cryogenic fluids

Data are acquired in the following manner. Initially, the cryostat is open, allowing the evaporating liquid to escape, and the laser beam is blocked from entering the cryostat. The channel and central reservoir are then sealed from the lab, and a small overpressure develops inside the cryostat as the liquid continues to evaporate. The air bearing is supplied with air pressure, and the apparatus rotated by applying a fixed voltage to the motor. The rotation rate is monitored, and we start a timer when the rotation rate reaches a steady state. The fluid spins up for a preset amount of time, as described in section 5.3.2. The laser beam is allowed to illuminate the fluid and particles. The linear motor controller pulls the grid and triggers the camera according to preset timing sequences. After the camera has finished acquiring its movie, usually a few seconds long, the laser beam is blocked and the rotation is stopped. The movie is downloaded from the camera, the pressure over the liquid in the cryostat is allowed to vent to the lab, and the process is repeated from the beginning to collect another movie. Movies are then transferred to the supercomputer for analysis as described in chapter 2.

### 5.3.2 Spinup of the fluid

Although the spinup of the fluid in a container can be estimated by different techniques, we choose our spinup time empirically in the following way. For each rotation rate and each fluid, the apparatus is allowed to spin for a certain amount of time as in section 5.3.1. A movie of particle motions is collected in the undisturbed flow (i.e., without pulling the grid). This procedure is repeated for varying spinup times until the

fluid is observed to be quiescent in the rotating frame. That is, until the fluctuating energy in the undisturbed rotating flow is approximately an order of magnitude lower than at any time during the observed period after the grid is drawn.

### 5.3.3 Liquid nitrogen

We perform several experiments with the cryostat containing liquid nitrogen at its boiling point of 77 K. Liquid nitrogen presents many of the same practical problems as liquid helium, such as low temperature, but to a lesser extent. For example, the thermal expansion coefficient of liquid nitrogen is about 100 times smaller than that of helium, so the flows we observe are less affected by heat input from the laser, as summarized in section 4.3.4. The kinematic viscosity of liquid nitrogen, $\nu \approx 2 \times 10^{-3}$ cm$^2$/sec, is intermediate between those of liquid helium and water. The experiments are performed using the same methods and apparatus described for liquid helium in chapter 2, with the exception of seeding particles.

In liquid nitrogen, we use 3.4 micron polymethyl-methacrylate particles, with a density of 1.2 g/cc. This density compares favorably with the density of liquid nitrogen, 0.8 g/cc. However, the particles clump, as discussed in section 3.3, and we observe a polydisperse suspension of aggregates that we estimate are typically 3 particle diameters across. Such clumps are inadequate for making quantitative velocity measurements due to their large inertia and settling velocity. However, we are interested in this chapter in the frequencies of velocity oscillations. We show in section 3.2.1 that the inertia of the particle may shift the phase of the observed oscillations, but not the frequency components of the motion.

### 5.3.4 Water channel

We also describe the results of experiments performed in a channel with circular cross section, shown in figure 5.2. These experiments used water as the working fluid, in an acrylic cylinder with a 24 cm inner diameter. The water was heated to about 85 °C, as a trial method of increasing the Reynolds number. The viscosity, ν, of water at this temperature is about 3 times smaller than that at room temperature, and is equal to $3.4 \times 10^{-3}$ cm$^2$/sec.

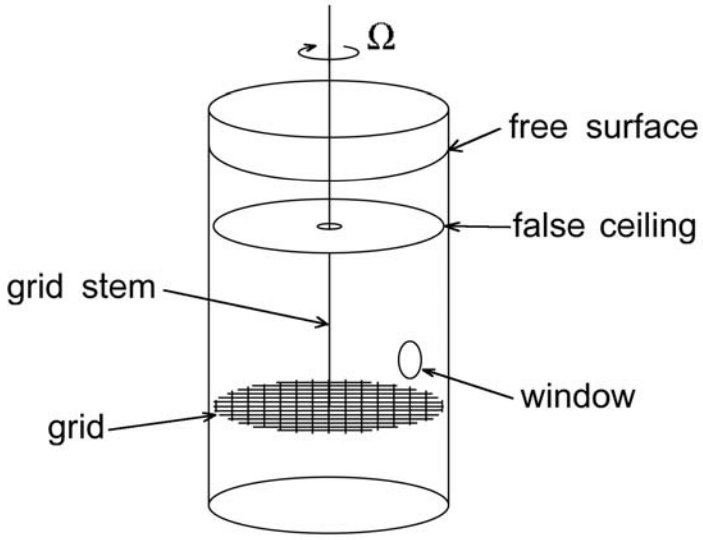


**Figure 5.2**: The circular cylindrical channel is put in place of the cryostat and is filled with water. The position of the false ceiling is adjustable. The indicated window faces the camera, while the laser passes through the curved wall of the channel.

The grid is constructed with the same biplane geometry and the same solidity as the grid used in the cryogenic channel, with a mesh spacing of 2.67 cm. The grid was adjusted in a similar way as described in section 4.3.2 for the cryogenic case in order to minimize the repeatable mean flow generated by drawing the grid. This tuning was done

by modifying the edge of the grid, where it contacted the inside of the channel. However, we found it impossible to shrink the magnitude of the mean flow such that its energy was smaller than that in the fluctuations, possibly because of the difference in symmetries between the square grid and circular perimeter.

The height of the column of water in which the grid is pulled is varied with a false ceiling. The false ceiling is constructed from sheet metal, with a 7 mm hole at its center to allow the free passage of the grid stem. The ceiling also has a gap between it and the wall around its perimeter of about 2 mm, and is suspended by four wires whose length is varied according the desired column height. The grid motion is not limited by the ceiling, and remains unchanged regardless of the position of the ceiling.

The particles used to trace the fluid motions in the case of water are 3.4 μm polymethyl-methacrylate particles with 1.2 g/cc density. The particles are suspended using a small amount of soap. We find that the particles remain suspended for long enough that a fresh injection of particles is needed only about twice per day. In addition, because of the difference between the indices of refraction of water and air, it is necessary to place the camera further from the axis of rotation than in experiments with nitrogen or helium. In order to keep the rotating camera from interfering with equipment fixed in the lab frame, we are forced to use a +2 diopter lens with the Nikon macro lens, allowing the camera to be brought back to its original location. The result is an increase in magnification, or a higher resolution of 12.6 μm per pixel instead of 16 μm per pixel.

The water channel is put in place of the cryostat, and in all other aspects, the experiments are performed as with the cryostat described in section 5.3.1.

## 5.4 Results

Here, we show that the flows generated in the rotating channels are distinguished by the presence of large scale inertial wave modes of the channels.

### 5.4.1 The energy decay

Using liquid nitrogen as a test fluid, we observe the evolution of turbulence at a steady system rotation of $\Omega = 0.98$ Hz. Turbulence is generated as described in section 5.3.3, with the grid drawn at $U_g = 1.0$ m/s, and with 7.2 mm mesh spacing, $M$. We compute the mean kinetic energy, $E$, in the volume of observation for all $N = 18$ realizations as in (4.3.2). As shown in figure 5.3, the energy decay shows unexpected behavior. It is seen to decrease initially almost as it did without rotation, but then to rise and fall after about 200 mesh times. The temporary increase in mean kinetic energy would be impossible if our data were from a region that was a representative volume of a homogenous flow, as it appears to be the case without rotation. It follows that there are important inhomogeneities and dynamics taking place on the scale of the container.

### 5.4.2 The mean flow

We compute the mean flow, given by (4.3.1), and find that the mean exhibits the same undulations characteristic of the total kinetic energy. This is shown in figure 5.4 over a period of about 15 system rotations. The mean is fairly repeatable from run to run, and in this regard is similar to the mean generated without rotation shown in figure 4.5. However, the mean shows repeated zero-crossings that are not seen without rotation.

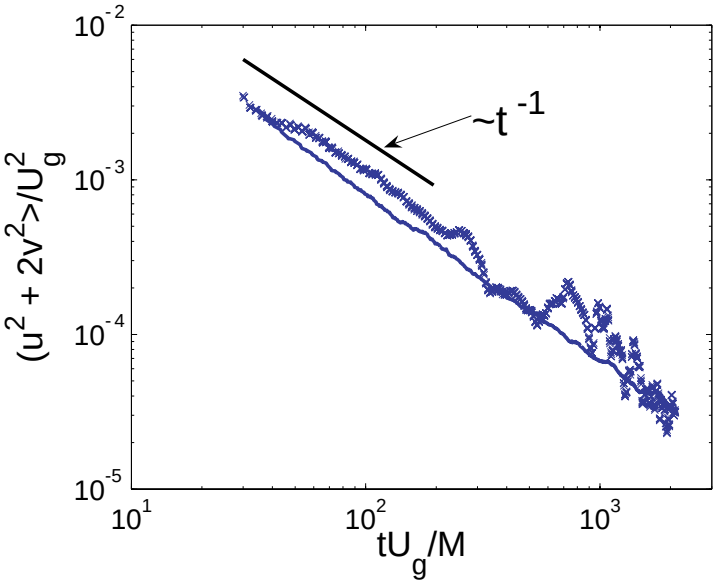


**Figure 5.3**: The crosses are the decay of kinetic energy in a channel rotating at about 1 Hz filled with liquid nitrogen, after being agitated with a grid. The solid line is from data acquired in the same way, but without system rotation, at a mesh Reynolds number of 72,000. In the stationary case, the decay of kinetic energy is slightly steeper than $t^{-1}$, which is expected of a lower Reynolds number flow, as described in chapter 4. The decay with rotation shows strong fluctuations in time.

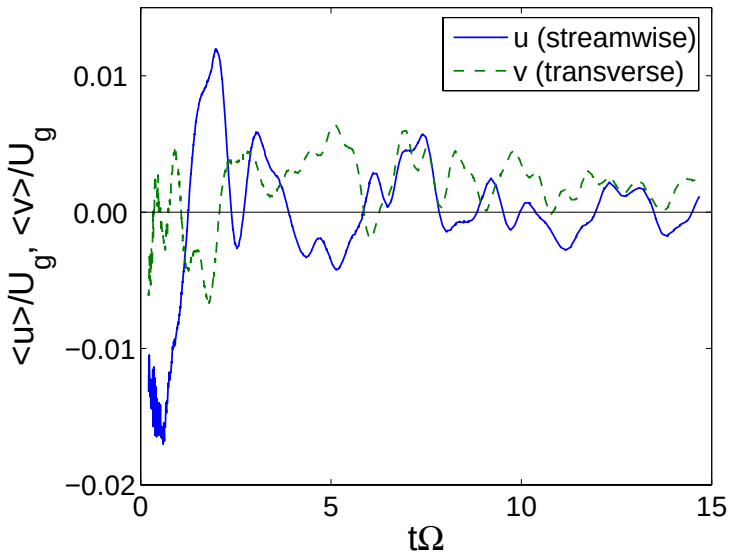


**Figure 5.4**: The mean flow for the same data as in figure 5.3. Streamwise flows are in the direction of grid motion.

In figure 5.5 we show that the mean flow accounts for a significant fraction of the velocity fluctuations. Over all of time, about 20% of the energy in the flow is carried in the mean in the root-mean-square sense. This occurs despite our efforts, described in chapter 4, to minimize the magnitude of the mean flow in the non-rotating system.

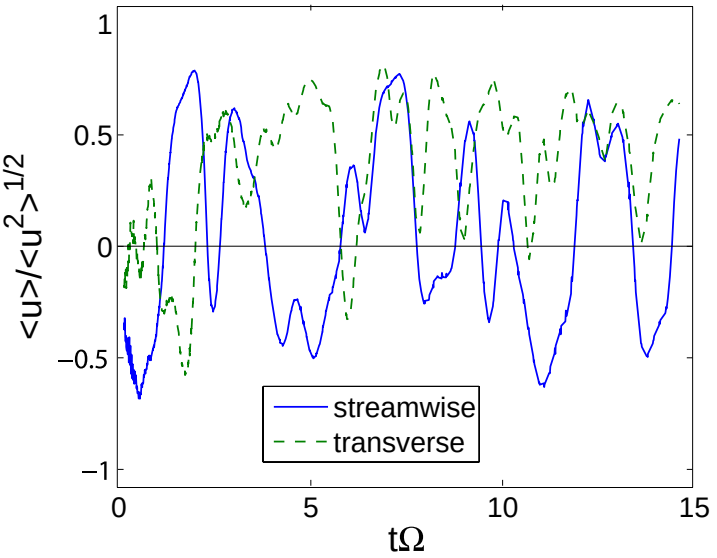


**Figure 5.5**: The mean flow shown in figure 5.4 relative to the stochastic fluctuations in the local velocity. The solid line is the streamwise velocity component; the dashed line is the transverse component. The oscillations are of comparable magnitude to the fluctuations throughout the decay.

### 5.4.3 Transform of the mean flow

We find the Fourier transform of the mean flow, in order to determine if the oscillations are comprised of a continuous spectrum of frequencies, as is the case in turbulence, or if they can be regarded primarily as the sum of discrete frequencies. Because the data are not evenly spaced in time, we cannot perform the transform in the

conventional way. We choose an arbitrary range of closely spaced frequencies, ω, and project our data onto each one. Figure 5.6 shows

$$|\mathcal{F}(u_{mn})(\omega)|^2 = |\Sigma u_{mn}\, e^{i\omega t}\, \Delta t\,|^2, \tag{5.4.5}$$

$$\text{and } |\mathcal{F}(v_{mn})(\omega)|^2 = |\Sigma v_{mn}\, e^{i\omega t}\, \Delta t\,|^2, \tag{5.4.6}$$

where the sum is taken over all time increments, and we plot the square of the magnitude of the complex function. The curves show well-defined peaks, each at a frequency less than twice the rotation rate. As described section 5.1.2, inertial waves are confined to oscillate at less than twice the rotation rate. The vast majority of the total energy in the mean flow, or of the area under the curve of the transform, evidently lies under the spectral peaks in this low frequency regime.

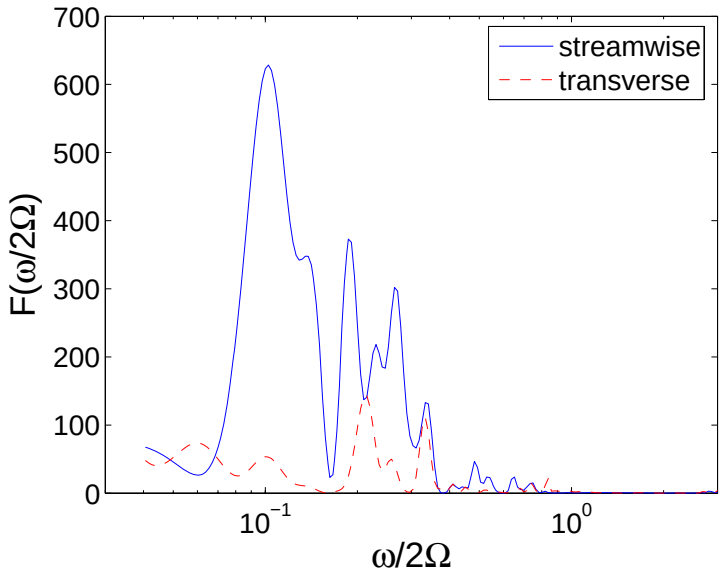


**Figure 5.6**: The transform of the repeatable mean flow shown in figure 5.4, generated by a grid drawn through liquid nitrogen in a square channel rotating at Ω = 0.98 Hz. The energy in each transform lies predominantly below a frequency that is twice the system rotation rate, as must be the case for inertial waves.

### 5.4.4 The circular apparatus

We repeat the above experiments using water in a channel with circular cross section, instead of a square cross section, as described in section 5.3.4. The grid is drawn at $U_g = 1.6$ m/s while the channel is steadily rotating at $\Omega = 1.7$ Hz. In the circular channel, we can predict the frequencies of inertial standing wave modes, reviewed in section 5.1.4. We find an oscillating mean flow, $\boldsymbol{u}_{mn}$, that is qualitatively similar to the one found in the square channel. The mean flow is shown in figure 5.7, and its transform taken as in section 5.4.3 is plotted in figure 5.8. Although we do not know what modes to expect, we find that the frequencies of the peaks are close to the three modes with the lowest wavenumbers. These modes are geometrically the simplest, with coherent structures nearly as large as the container itself.

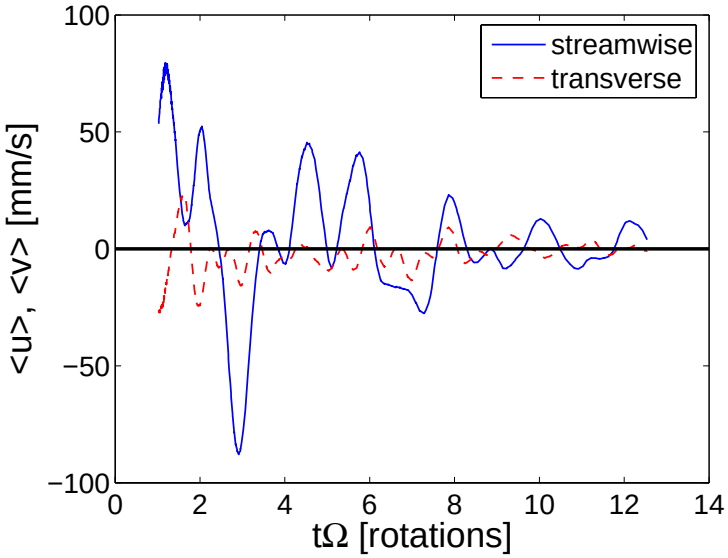


**Figure 5.7**: The mean flow in the water channel for $h = 80$ cm, comparable to figure 5.4 of the same measurement, but using liquid nitrogen in a square channel.

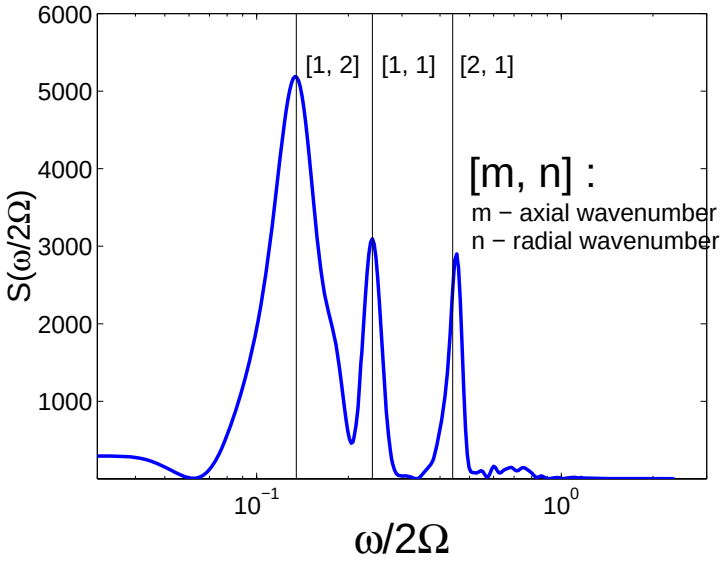


**Figure 5.8**: The transform of the streamwise, or axial, mean flow shown in figure 5.7. The vertical lines are the locations of inertial wave modes predicted by Kelvin's linear, inviscid theory given in section 5.1.4.

We repeat the experiment with different heights of the column of water, collecting data from about 25 to 30 realizations for each aspect ratio. We find that the locations of the peaks in the transform of the streamwise mean flow coincide in each case with the predicted location of a low wavenumber mode, as shown in figure 5.9. Peaks are identified as such if they are at least one fifth as tall as the dominant peak. The structure of the low wavenumber modes varies over distances much larger than the dimension of our window. Because of this, we cannot examine the spatial structure of the hypothetical waves in our data, and cannot definitively assign the peaks to modes of particular wavenumbers.

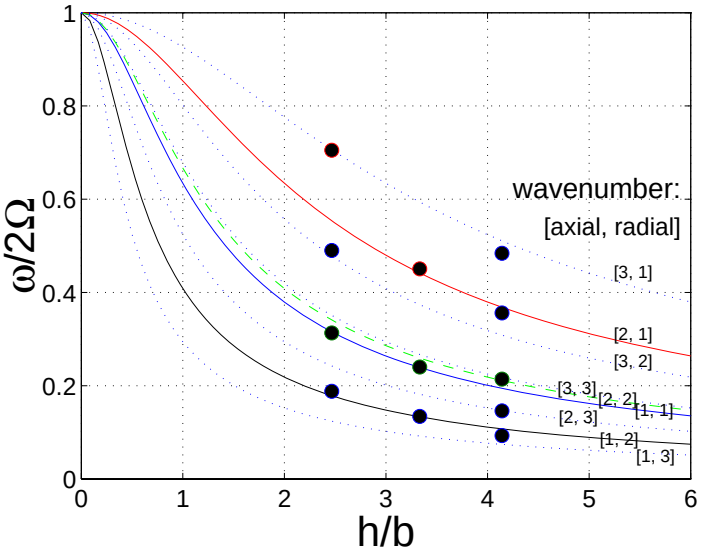


**Figure 5.9**: We plot as circles the frequencies of the dominant peaks in spectra, such as the one in figure 5.8, for a series of aspect ratios, $h/b$, where $h$ is the length of the channel along the axis of rotation, and $b$ is its radius. The curves are calculated according to (5.1.8) for different combinations of axial and transverse wavenumbers.

### 5.4.5 Revisiting the square channel data

We compare the natural frequencies predicted by Maas (2003) with the spectrum computed from the mean flow in liquid nitrogen given in figure 5.6, and find good agreement. However, we present here an alternative analysis, by computing frequency spectra from the velocity fields rather than from the mean flow. For each realization of the experiment, we take the transform of the time series of the mean velocity in a small sub-region of the whole velocity fields. The mean is taken in this way, over several spatially adjacent vectors, in order to avoid the complication of performing the Fourier transform on data that has drop-outs. This local mean is computed over the group of a vector's nearest neighbors that are available. This can be expressed as

$$|\mathcal{F}'(u)(\omega, \boldsymbol{x}, j)|^2 = |\Sigma u(\boldsymbol{x}, j)\, e^{i\omega t}\, \Delta t|^2, \tag{5.4.7}$$

$$\text{and } |\mathcal{F}'(v)(\omega, \boldsymbol{x}, j)|^2 = |\Sigma v(\boldsymbol{x}, j)\, e^{i\omega t}\, \Delta t|^2, \tag{5.4.8}$$

where the new $\mathcal{F}'$ is a function of the particular realization, $j$, and $\boldsymbol{x}$ points to the center of the sub-region where the local mean velocity, $u$ or $v$, is found. In this way, we account for the variation in phase of the excited inertial wave modes from run to run, as well as for frequency components with spatial structure smaller than the whole captured field. The mean of these spectra, taken over all points in space, and for all realizations, is plotted in figure 5.10, along with Maas's predictions given in table 5.1. Since the square channel is long in the axial direction, it is natural that the dominant inertial wave modes are found divided in the axial direction rather than in the radial direction. It is evident that, as in the circular cylindrical channel, most of the energy in the mean flow is represented by peaks corresponding to the frequencies of standing wave modes. In conclusion, a significant fraction of the energy of the whole flow is in its repeatable mean, and most of the energy in the mean flow is, in turn, accounted for by several spectral peaks at the characteristic frequencies of confined inertial waves.

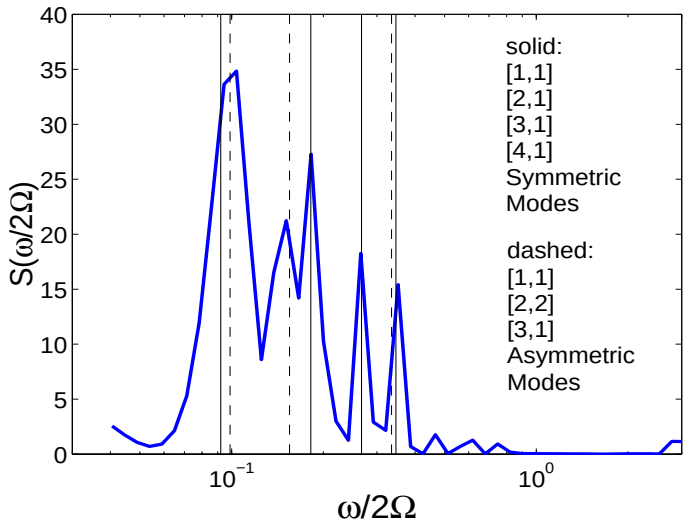


**Figure 5.10**: The frequency spectrum of velocity fluctuations in a rotating square channel filled with liquid nitrogen. The vertical lines are predictions made by Maas (2005), whose [axial, transverse] wavenumbers are given in the order of increasing frequency. Most of the peaks correspond to successively higher axial wavenumbers.

### 5.4.6 The square channel with liquid helium

We perform nearly the same experiments as in section 5.4.1, except with liquid helium in place of liquid nitrogen. We rotate the channel twice as fast, at $\Omega = 2.0$ Hz, and draw the grid at the same velocity, $U_g = 1.0$ m/s. We present data for $N = 13$ realizations. The decay of kinetic energy, shown in figure 5.11 shows the same characteristic features as described in section 5.4.1, although the undulations alter the energy decay in about one quarter of the time that it took when liquid nitrogen was used.

The mean flow, as computed in section 5.4.2, is qualitatively similar to that observed in liquid nitrogen, accounting for the same fraction of the total energy (see figure 5.12). Its transform, however, is more difficult to interpret, as seen in figure 5.13. It shows well defined peaks, as did the other transforms we have reviewed, but the peaks of the lowest frequencies do not obviously correspond to inertial wave modes, as do the peaks found using data acquired in liquid nitrogen.

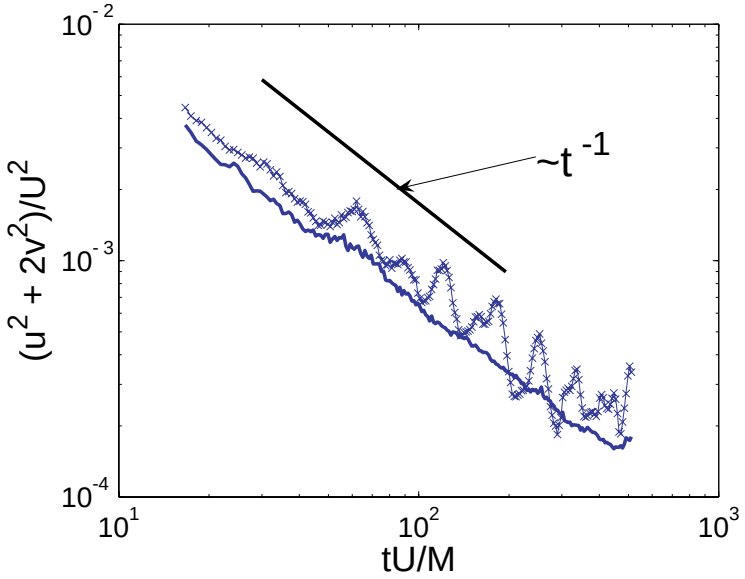


**Figure 5.11**: The decay of energy in liquid helium with and without rotation. The solid curve is from figure 4.6, for a mesh Reynolds number of 283,000. The crosses trace a curve similar to that observed in liquid nitrogen in figure 5.3.

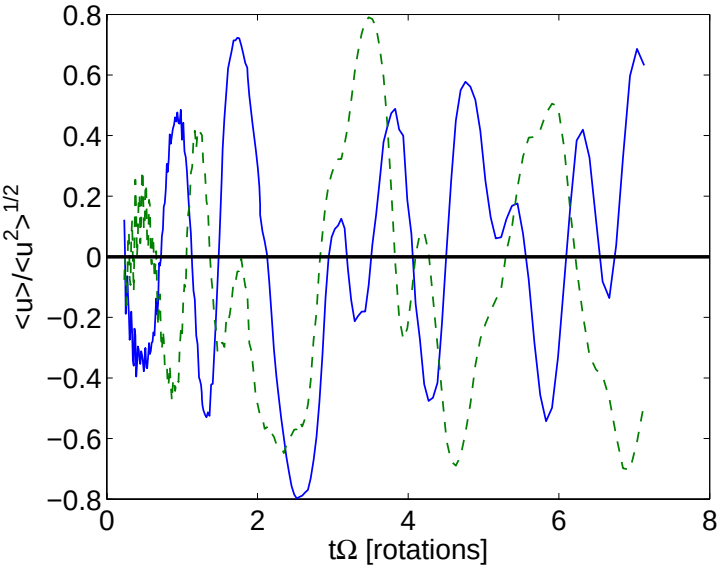


**Figure 5.12**: The mean flow in liquid helium, relative to the fluctuations. The solid line is the streamwise velocity component; the dashed line is the transverse component. The oscillations are of comparable magnitude to the fluctuations throughout the decay.

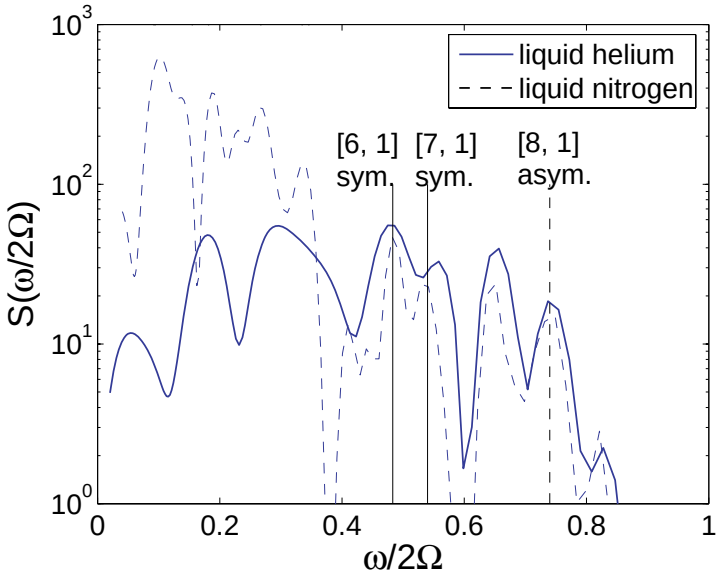


**Figure 5.13**: The solid curve is the transform of the streamwise mean flow in liquid helium. It shows well defined peaks, all lying below twice the rotation rate. We show the data from figure 5.6 using liquid nitrogen as a dashed curve. The peaks of the two curves coincide at high frequencies, but not below $\omega/2\Omega \approx 0.4$. We indicate the frequencies of some high axial wavenumber inertial wave modes as suggestions, but there are many other modes with frequencies that do not lie near peaks.

## 5.5 Discussion

### 5.5.1 The modes in liquid helium

We do not know the explanation for the differing behaviors of the mean flows in liquid nitrogen and liquid helium. One possibility is that we observe the liquid nitrogen flow for twice as many rotation periods as the liquid helium flow. The period of the simplest low frequency wave mode, the [1, 1] symmetric or asymmetric mode, is about 5 rotations. Although we observe the liquid helium flow for approximately 7 rotations, it is possible that our ability to resolve the low frequency modes is compromised to the extent that we cannot distinguish them from each other. The liquid helium transform begins to resemble the liquid nitrogen curve for oscillation periods shorter than about one rotation. In the liquid nitrogen flow, however, the transform appears to conform to predicted wave modes with periods as much as five times longer, although we only observe the flow for twice as many rotations as in liquid helium. Further experiments are probably required to understand this discrepancy.

### 5.5.2 The right experiment

We ask whether we can design an experiment in which inertial waves will not interact with the boundary during some period of observation. Let us consider the case that there is no energy transfer among different scales of motion, and the distribution of energy is set by initial conditions such as the drawing of the grid and purely turbulent dynamics. We monitor a region in the center of the volume, and wonder how long it takes for the fluid in this region to communicate with the boundaries. Energy is carried

by inertial waves at a rate defined in equation (5.1.6). It is readily shown that the first waves to arrive in our region from a boundary in a channel of size $W$ are carried by a wave-vector, $\boldsymbol{k}$, with magnitude, $k$, inclined at 45 degrees to the axis of rotation, and their transit time is

$$t_B = W / |\boldsymbol{c}_g| = Wk / \Omega. \tag{5.5.4}$$

Short waves travel slower, but for the large-scale waves we have observed, where $Wk$ nearly equals one, so that by the time the system has undergone one rotation the whole volume has sensed the boundaries.

As we show in chapter 4, it is difficult to force turbulence using a grid in such a way that energy input is confined to length scales in a range controlled by the grid spacing. A significant amount of energy is injected at larger scales, including scales that span the container. Let us imagine that it is possible, however, to construct a perfect grid and an experiment where the input energy is confined to scales of the order of the grid spacing, $M$. We will take our desire to study the effects of rotation to mean that the Rossby number is much smaller than one, say

$$Ro = u / \Omega M = 10^{-n}, \text{ for } n > 1, \tag{5.5.5}$$

where $u$ is characteristic of the energy containing eddies of size $M$. In addition, we take our desire to study the evolution of turbulence under rotation to mean that we observe the flow for many large-eddy turnover times:

$$t_E = 10^m M / u, \text{ for } m > 1. \tag{5.5.6}$$

Since we are interested in the period before communication with the walls, we require that $t_E > t_B$, with $k \sim 1/M$:

$$10^m > Wu / M^2 \Omega. \tag{5.5.7}$$

In this equation, we see the Rossby number, upon regrouping, for which we substitute $10^{-n}$ as in (5.5.5), such that:

$$W / M < 10^{m+n}. \tag{5.5.8}$$

This imposes a severe limitation on the mesh spacing of our grid, that it be at least 100 times smaller than the width of the channel. This is, of course, at odds with our other objective of generating high-Reynolds-number turbulence, since the Reynolds number is proportional to the same length scale.

### 5.5.3 The source of energy for the large scales

The assumption made in section 5.5.2 that energy is not redistributed to the largest scales of motion is, in fact, probably good for small times. Smith and Waleffe (1999) show that for $Ro \approx 0.1$ energy does not accumulate at large scales in a simulated rotating flow forced isotropically on the small. However, in order for the accumulated energy in the large scales to reach an appreciable fraction of the total kinetic energy, the flow must evolve for about 100 system rotations. In our system, it appears to that energy is present in container-sized scales within one rotation. This suggests that energy for the inertial waves is determined by the initial conditions, by direct action of the grid motion, rather than emerging by interaction of the more energetic scales that are comparable to the size of the mesh spacing.

### 5.5.4 The parameter *J*

We compute the parameter *J*, given by (5.2.1), for our experiments. For each fluid, *J* is larger than 100 throughout the observed range of times. At early times, or

within one system rotation, $J$ is larger than 1000 in liquid nitrogen, 350 for water, and 450 for helium. These values are sufficiently large, according to Jacquin et al. (1990), that dissipation of energy by inertial waves in boundary layers can be neglected.

### 5.5.5 Why the modes have not been previously observed in this context

It may be surprising that inertial wave modes have not been reported in previous studies of rotating turbulence analogous to our own. There are several possible reasons why this is so.

Although we have not discussed numerical simulation of rotating flows, such studies have been done (e.g., Yeung and Zhou 1998). The periodic boundary conditions typical of a numerical simulation are different than our own, but we expect a rule governing the discretization of wave modes analogous to the one found in a container. Since inertial waves only have a simple harmonic structure in time, it is probably true that they will only be discovered in Fourier transforms performed over time, rather than across space. It is generally true that the huge amounts of velocity data generated at each time step are not stored for longer than is needed for the subsequent iteration in time in numerical simulations. For this reason, frequency spectra are seldom computed in numerical studies, and so inertial wave modes have not been identified.

In experimental studies, only one scientist (Dalziel 1992) used continuous-time recording of the flow, and he does report undulations in the signal. In order to identify the inertial wave modes, we consider it essential to compute the time-transform of the flow, but this analysis was not reported in the aforementioned study or in any other.

### 5.5.6 A note on the decay rate

It appears from the data we have presented that rotation does not markedly affect the overall rate of decay of kinetic energy. Although we do not have data collected under diverse enough conditions to make statements about the dependence of the decay on the rate of rotation, we venture a hypothesis. In chapter 4, we argue that the decay exponent in stationary turbulence depends somewhat on the method of forcing turbulence, and in particular on the large scales of motion. If this is true, then we can expect the decay rate to change slightly with system rotation because the initial disturbance generated by the grid is affected. Thus, changes in the decay rate measured with rotation cannot be attributed solely to changes in the mechanism of energy transfer and dissipation caused by Coriolis forces during the evolution of turbulence.

## 5.6 Conclusions

We find, when trying to generate homogeneous turbulence in a rotating channel by towing a grid, that instead we generate standing inertial waves with frequencies at the modes of the container. This appears to be the first report of inertial wave modes created in this way. We believe that the generation of these modes may explain the differences in energy decay behavior in different experiments in stationary grid turbulence. That is, the differences may be caused by long-range correlations imposed by the initial conditions.

# Chapter 6

# Visualizing quantized vortex lines

Our technique for generating fine suspensions of particles in liquid helium also allows us to observe superfluid flows. Historically, experimental observations of superfluidity in He II, a distinct phase of liquid helium, have produced a wealth of data on the bulk properties of flows, but almost none revealing local velocities. As we show in chapters 3 and 4, our particles allow such local measurements, and we seek to extend these experiments to He II, using a grid to generate turbulence and PIV to measure velocities. Even before we draw the grid though, we find that the particles collect along slender filaments in He II, and we present evidence that these filaments are the cores of quantized vortices. With the vortices delineated by particles, we have recorded what are to our knowledge the first images of the outlines of quantized vortex cores, and directly observe their geometry and interactions in a three-dimensional stochastic environment (Bewley, Lathrop and Sreenivasan 2006).

## 6.1 Background

We begin with a brief introduction to liquid helium and superfluidity in order to provide some intuitive background for the discussion that follows. Although no

comprehensive microscopic description of superfluid helium exists, several ideas and models help interpret our observations. These include the ideal line vortex and the two-fluid model. We also use classical fluid dynamics to answer some questions that arise naturally when superfluidity is encountered. The information that follows can, for the most part, be found in the more thorough discussions on the superfluidity of helium and fluid dynamics by Feynman (1955) and Batchelor (1967), respectively. Other useful references are Schwartz (1988) and Tough (1982).

### 6.1.1 Basic physical properties of liquid helium

We use the most abundant isotope of helium, helium-4, and as a liquid it boils at 4.2 K at atmospheric pressure, as shown in figure 6.1. At this temperature and pressure, the liquid is known as He I, and behaves like a Newtonian fluid (Skrbek 2004); we have performed the experiments described in previous chapters at these conditions. At lower temperatures, a phase transition occurs across what is known as the lambda line in the phase diagram. At the saturated vapor pressure of liquid helium the transition occurs at 2.177 K, called the lambda point.

No latent heat is associated with the transformation between He I and the colder phase, named He II. The phase transition is, therefore, of the second order. The transition temperatures are so called because of the resemblance to the Greek letter λ of a curve of the specific heat against temperature near the transition, shown in figure 6.2. He II displays quantum mechanical behaviors at scales much larger than atomic dimensions. One of these macroscopic manifestations of quantum mechanics is superfluidity, the ability of a fluid to flow without friction, though He II is a true

superfluid only at absolute zero (Donnelly 1967). Superfluidity was discovered in 1938 by Kapitza and his associates (Dingle 1952). Another unusual feature of the new phase is the emergence of vortices with quantized circulation.

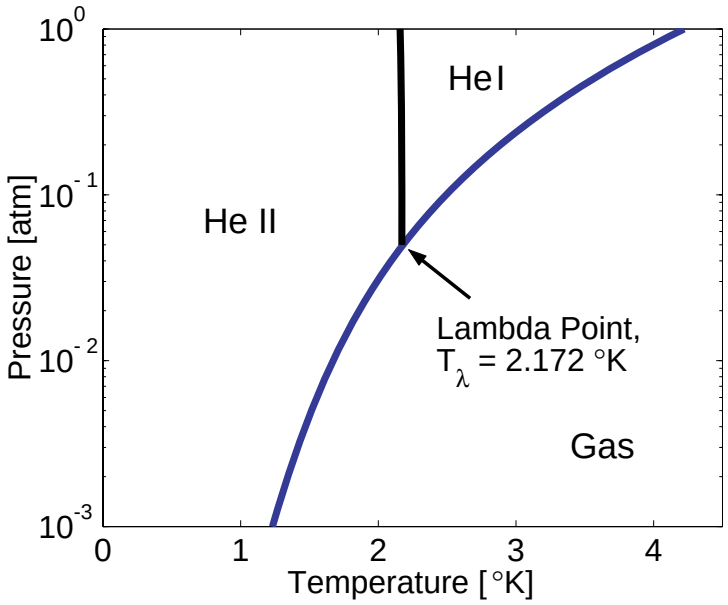


**Figure 6.1**: Phase diagram for helium near the lambda point, from Donnelly (1967).

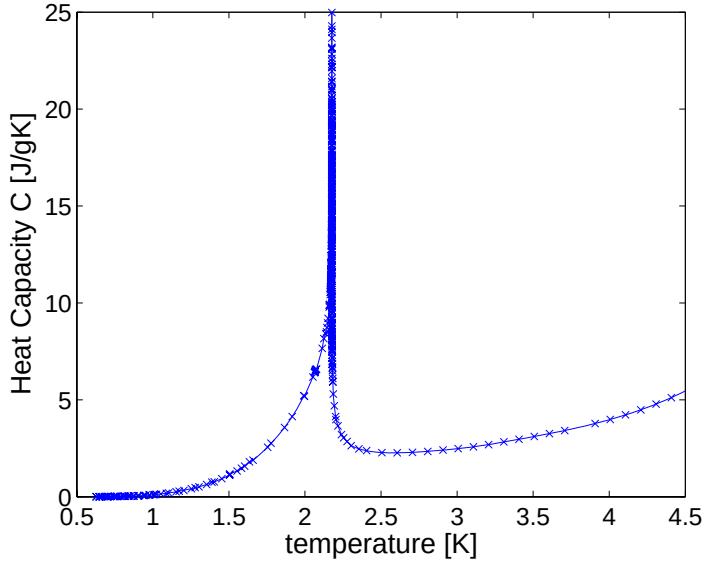


**Figure 6.2**: The specific heat of liquid helium as a function of temperature at the saturated vapor pressure, from data collected by Donnelly and Barenghi (1998).

### 6.1.2 Quantized vortices

We give some arguments illustrating the origin and nature of quantized vortices. Begin by thinking of a superfluid as a normal fluid with zero viscosity, and recall that an inviscid fluid that is initially irrotational will remain so for all later times (Batchelor 1967). If the fluid is initially irrotational, it follows that the integral of velocity around a reducible closed path is zero for all time. Note that the size of a loop can be made asymptotically to approach zero in any simply connected region. The integral of the fluid velocity, $\boldsymbol{u}$, around a loop is called the circulation, so that:

$$\Gamma = \int_C \boldsymbol{u} \cdot d\boldsymbol{s} = 0 \tag{6.1.1}$$

for all reducible closed curves, $C$, where $\Gamma$ is the circulation. An irrotational flow can be expressed in terms of a scalar potential function, $\phi$, such that

$$\boldsymbol{u} = \nabla\phi. \tag{6.1.2}$$

A flow with nonzero circulation can also be defined in terms of a potential function if the region in which the flow is defined is multiply connected, and we may form such a region by piercing space with a cylinder of infinite length. It is possible in the region outside the cylinder to define loops that ensnare the cylinder and cannot be made vanishingly small in the limit. For a flow that orbits the cylinder with an arbitrary circulation, $\kappa$, the expression defining the potential function can be written

$$\boldsymbol{u} = \kappa\nabla\phi'. \tag{6.1.3}$$

That is, the circulation around all trajectories that circle the cylinder is $\kappa$, but reducible loops elsewhere in space yield zero circulation. As the radius of the cylindrical hole in space approaches zero asymptotically, we obtain a classical line vortex that has a locally cylindrical flow with azimuthal velocity at radius $r$ given by:

$$u_\phi = \kappa/2\pi r. \tag{6.1.4}$$

The classical line vortex can be identified with a material element, and they must form closed curves, or terminate on fluid boundaries (Lamb 1879).

A superfluid is not, however, an inviscid fluid. Its behavior is closely associated with quantum mechanics, and this has several important consequences. According to Onsager's proposition (Feynman 1955), circulation in a superfluid is quantized; the integral of the fluid velocity around any closed circuit is constrained to be a multiple of Planck's constant, $h$. This proposition is valid because the whole fluid may be represented by a wave function of the form $f(\boldsymbol{r},t)e^{i\varphi(\boldsymbol{r},t)}$ that evolves according to a nonlinear form of Schrödinger's equation (Roberts and Berloff 2001). The wave function's phase, $\varphi$, is the flow field's potential function, that is,

$$\boldsymbol{u} = K\nabla\varphi, \tag{6.1.5}$$

where the constant of proportionality, $K$, equals $h/2\pi m$ and $m$ is the mass of a helium atom. If, as above, we consider the variation of the phase along closed curves that cannot be reduced to zero length, the phase must differ by integer multiples of $2\pi$ around the path, in order for the wave function to be continuous in space. It follows that circulation is proportional to the change in the phase as one goes around a loop, and is therefore quantized as

$$\kappa_n = \int_C \boldsymbol{u}\cdot d\boldsymbol{s} = K\int_C \nabla\varphi \cdot d\boldsymbol{s} = nh/m, \tag{6.1.6}$$

where $n$ is an integer.

A quantized vortex can be visualized as a hole in the superfluid somewhere inside the loop, $C$. The hole creates a multiply connected region and allows the construction of irreducible loops with nonzero circulation. In fact, the density of the superfluid is

thought to approach zero as the centerline of the vortex is approached (Donnelly 1991). One can imagine the fluid's centrifugal acceleration forming a hole balanced by surface tension. However, for this condition to be satisfied, the radius of the core must be so small that the notion of a continuous free surface may break down. Nonetheless, the radius of a core has been estimated experimentally to be about 1 angstrom (Glaberson and Steingart 1986).

The energy of aligned vortices, each with one quanta of circulation, is lower than that of a single vortex whose circulation is equal to the sum of the dispersed ones' circulations. Therefore, it is generally believed that such multiply quantized vortices are not present in real flows (Vinen 2006). There is evidence that multiply quantized vortices are unstable in Bose-Einstein condensates (Shin 2004, Möttönen 2003), although we do not know of similar work in He II.

As with the classical line vortex, the superfluid velocity away from the core is a potential flow with no vorticity; all the vorticity is concentrated along the vortex centerline. Even if vortices are separated by only a hundred microns, as they often are, their cores are $10^6$ smaller than their separation and the vortices likely interact as if they were close approximations to ideal line vortices.

### 6.1.3 Quantization and the evolution of vortices

Quantized vortices are often treated as ideal line vortices that have an unchanging, quantized circulation. Although it might be thought that this quantization constrains the dynamics of the vortices, it does not do so. In order to see why, notice that circulation is related to vorticity through Stokes' theorem. The expression for the evolution of

vorticity, $\boldsymbol{\omega} = \nabla \times \boldsymbol{u}$, in an inviscid fluid is found by taking the curl of the momentum equation, yielding:

$$D\boldsymbol{\omega}/Dt = \boldsymbol{\omega} \cdot \nabla \boldsymbol{u}. \tag{6.1.7}$$

By rewriting the gradient as a derivative along a small material line element, $\delta \boldsymbol{l}$, initially aligned with the local vorticity, (6.1.7) implies the startling rule that vorticity evolves in the same way as the material element,

$$1/|\boldsymbol{\omega}|\, D\boldsymbol{\omega}/Dt = 1/|\delta \boldsymbol{l}|\, d\delta \boldsymbol{l}/dt. \tag{6.1.8}$$

In words, if the line element in the fluid is stretched, so too will vorticity grow in proportion. This expression has important consequences in the classical theory of turbulence. For example, Taylor and Green (1937) argue that vortex deformation plays an important role in the redistribution of energy among the scales of motion. One is naturally led to wonder if similar processes are at work in the evolution of vortices in a superfluid, and if these processes are constrained by the quantization of circulation.

From Stokes' theorem, the expression relating vorticity and circulation around a single line vortex reduces to

$$\boldsymbol{\omega} \cdot \delta \boldsymbol{A} = \kappa. \tag{6.1.9}$$

Here, $\delta \boldsymbol{A}$ is the normal to a surface element that intersects the vortex core such that $\boldsymbol{\omega} \cdot \delta \boldsymbol{A} / |\boldsymbol{\omega}|$ is the cross sectional area of the core, and $\kappa$ is the circulation strength of the vortex. Everywhere else, the vorticity is zero, and (6.1.9) implies that the magnitude of vorticity in the core has no impact on the bulk flow if it changes in inverse proportion to $\delta \boldsymbol{A}$. In fact, we find just this relation when we take the time derivative of $\boldsymbol{\omega} \cdot \delta \boldsymbol{A}$, and substitute (6.1.8):

$$d(\boldsymbol{\omega} \cdot \delta \boldsymbol{A})/dt = (|\boldsymbol{\omega}|/|\delta \boldsymbol{l}|)\, (d\delta \boldsymbol{l}/dt \cdot \delta \boldsymbol{A} + \delta \boldsymbol{l} \cdot d\delta \boldsymbol{A}/dt) \tag{6.1.10}$$

The sum in this expression equals zero by the conservation of mass in an incompressible fluid. Equation (6.1.10) therefore implies that $d\kappa/dt = 0$ and the powerful statement that the circulation around a material curve in an inviscid fluid does not change with time. That is,

$$d\Gamma/dt = 0 \tag{6.1.11}$$

where $\Gamma$ is the circulation around a curve that may embrace several vortices so that $\Gamma$ equals the sum of their individual strengths. Since the circulation round any loop in the volume remains constant over time in an inviscid fluid containing ideal vortices, the further condition that circulation be quantized only confines the initial state of the vortex configuration. Thereafter, quantization does not impose an additional constraint on the evolution of the vortices.

### 6.1.4 The two-fluid model

He II is not entirely a superfluid for temperatures above absolute zero. According to the two-fluid model, He II consists of two interpenetrating fluids, a superfluid and a normal fluid, with different density and velocity fields, $\rho_s$ and $\boldsymbol{u}_s$, and $\rho_n$ and $\boldsymbol{u}_n$, respectively. As shown in figure 6.3, the fraction of the total fluid density that is the normal fluid falls rapidly as a function of temperature below the lambda point, and is zero at absolute zero. Tisza (1938) proposed the two-fluid model and it is presented in a review by Dingle (1952).

The two-fluid concept may be derived by considering thermal energy to be carried exclusively by discrete excitations, such as a density fluctuation propagating at the speed of sound. These excitations are in turn treated as particles propagating through the body

of helium atoms at their lowest energy state. Because the excitations interact and behave on the macroscopic scale like a normal fluid, they are called the normal fluid part. The background of helium through which the excitations propagate is the superfluid component of the fluid. The quantized vortices in this model reside entirely in the superfluid component, but experience a drag force with motions relative to the normal fluid. The expression for this drag force per unit length of line is given by Donnelly (1991), and its magnitude is

$$f_m = C\rho_s\kappa v_L, \tag{6.1.12}$$

where $C$ is a constant of order one between 1.4 K and 2.1 K, and $v_L$ is the velocity of the line relative to the normal fluid. The drag between the quantized vortex cores and the normal fluid is the only coupling between the motions of the two components. When there are no superfluid vortices, the motions of the two fluids are independent.

The fraction of the fluid density assigned to each component in the two-fluid model is found by construction (Feynman 1955), and neither of the fluid fractions in the model can be thought to represent tangible material, as can a classical fluid by the foundations of continuum mechanics. In practice, application of the model depends on the knowledge of several empirical constants that depend on temperature, fluid velocity, and frequency of flow oscillations. The model nevertheless gives intuitive explanations for some of the behavior of He II.

The fraction of the fluid density assigned to each component in the two-fluid model is found by construction (Feynman 1955), and neither of the fluid fractions in the model can be thought to represent tangible material, as can a classical fluid by the foundations of continuum mechanics. In practice, application of the model depends on

the knowledge of several empirical constants that depend on temperature, fluid velocity, and frequency of flow oscillations. The model nevertheless gives intuitive explanations for some of the behavior of He II.

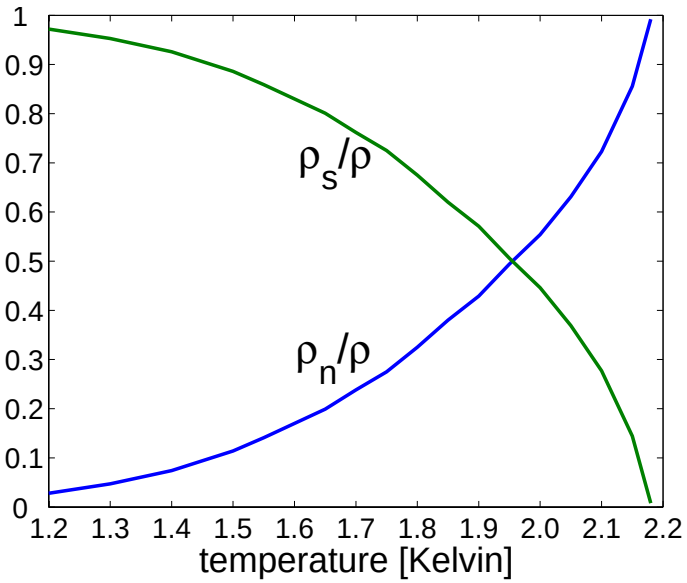


**Figure 6.3**: The two curves shown are the densities of the normal fluid and superfluid in the two fluid model of He II, at its saturated vapor pressure. The densities sum to the whole fluid's density, which is almost constant as a function of temperature and nearly equals 0.14 g/cc. At the lambda point, He II is entirely accounted for by the normal fluid part. At absolute zero, He II is a pure superfluid.

### 6.1.5 Residual vortices

Quantized vortices, and the holes at their cores, can be conceived as defects in the superfluid state, analogous to defects that arise in many other materials during phase transitions, such as grain boundaries in a polycrystalline solid. Similarly, vorticity in the form of vortex defects is created in the superfluid by the phase transition itself (see Zurek 1996). In the ensuing evolution and decay of the resulting tangle of vortices, some of them will ultimately span the volume, pinned at each end to some protruding feature of

the boundary (Schwartz 1985), and too far from other vortices to interact so as to reduce the total length of line present. Energy is imparted to these vortices during the phase transition and persists indefinitely in the fluid. Donnelly (1991) estimates that the line density, $L_r$, in a bounded volume of superfluid satisfies the inequality

$$L_r < 2 \ln (d/a) / d^2, \tag{6.1.13}$$

where $d$ is the characteristic size of the volume, and $a$ is the vortex core radius.

### 6.1.6 A rotating superfluid

Steady rotation of a superfluid ideally produces a roughly triangular array of quantized vortices, aligned with the axis of rotation. Feynman (1955) used such rotation to introduce theoretically the existence of quantized vortices, and rotating He II is also experimentally useful as a diagnostic tool. Feynman argued that the lowest energy state for a superfluid forced into rotation was a population of quantized vortices, each with the minimum strength of one quanta of circulation and aligned with the axis of rotation. With all the vorticity of the bulk rotation residing in the cores of the singly quantized vortices, the number density of the vortex lattice is proportional to the rotation rate, and is given by

$$n_o = 2 \Omega/\kappa \approx 2000 \Omega \text{ lines/cm}^2, \tag{6.1.14}$$

where $\Omega$ is the angular velocity of the container in rad/s. This expression has come to be known as Feynman's rule (Donnelly 1991). Tkachenko (1965) showed that when the number of vortices is large, they form a triangular lattice. The array itself rotates with the same frequency as the container, and may be distorted from the triangular ideal to conform to boundary conditions (Campbell and Ziff 1979).

### 6.1.7 Flows in He II

Above a certain critical velocity of the order of 1 mm/s in many flows, the flow of He II is energetic enough to sustain the generation of quantized vortices. In the context of the two-fluid model, the friction of the quantized vortices with the normal fluid introduces a mechanism for the damping of superfluid motions. An evolving system of interacting and reconnecting quantized vortices is described as a vortex tangle, from visualizations of numerical simulations (e.g., Schwartz 1988). The simulations show that the tangle can quickly become dense, with vortices spaced by a few tens of microns.

A common way to generate turbulence in He II experimentally, apart from mechanical agitation, is to drive it thermally. He II responds differently from a classical fluid to heat input as the resulting flow is not primarily driven by buoyancy. Briefly, heat is transported by opposing normal fluid and superfluid flows, generating a counterflow. Superfluid rushes toward a heat source where it is converted to normal fluid, and the normal fluid carries heat away to the sink. This mechanism is responsible for the immense effective thermal conductivity of He II, which under some conditions is 7 orders of magnitude larger than that of He I (Donnelly 1967). Vinen (1957b) showed experimentally that the counterflow can be characterized by $v_{ns}$, the difference in velocities between the superfluid and normal fluid components averaged over time and space. For the small channels and low temperatures typical of the results presented by Vinen (1957a) and others (see Tough 1982), the flow becomes unsteady at counterflow velocities of a few mm/s. Above this critical velocity, $v_c$, the formation of quantized vortices is detected experimentally, and their presence can be quantified by the line density, $L_o$, in units of length per unit volume. Tough (1982) finds that all data from

approximately homogeneous counterflows agree with the following relations for the critical velocity and line density. The critical counterflow velocity is reached when

$$v_c d\gamma_o > 4, \tag{6.1.15}$$

in a channel of characteristic width $d$. The expression resembles the condition for a classical fluid becoming turbulent, which is in terms of the Reynolds number. However, the constant $1/\gamma_o$ is typically more than 100 times larger than the viscosity of the normal fluid; $\gamma_o$ is strongly temperature dependent and is approximately 145 s/cm$^2$ at 2.1 K. The line density above the critical velocity, again given by Tough (1982), in terms of the counterflow velocity driving the turbulence is

$$L_o \approx (\gamma_o v_{ns} - 1.5/d)^2, \tag{6.1.16}$$

where we have left out some factors that are of order one and are geometry dependent.

### 6.1.8 Previous experimental observations

Williams and Packard (1974) succeeded in visualizing quantized vortices by using an ingenious method to record the points of intersection of the vortices with the free surface of the fluid. They introduced ions that were trapped by the vortices in a rotating sample of He II. An applied electric field caused the charged particles to travel along the vortices and exit through the free surface against a phosphorescent screen. Continuing this work, Yarmchuk et al. (1979) determined from the resulting images that steadily rotating He II supports a triangular array of vortices. Some examples are shown in figure 6.4. Although the number of vortices showed significant hysteresis upon acceleration and deceleration of the rotation rate, the number agreed with predictions, frequently to within about 5%. No one has produced images of vortices inside the body

of the fluid, or of vortex tangles, prior to those described in this dissertation.

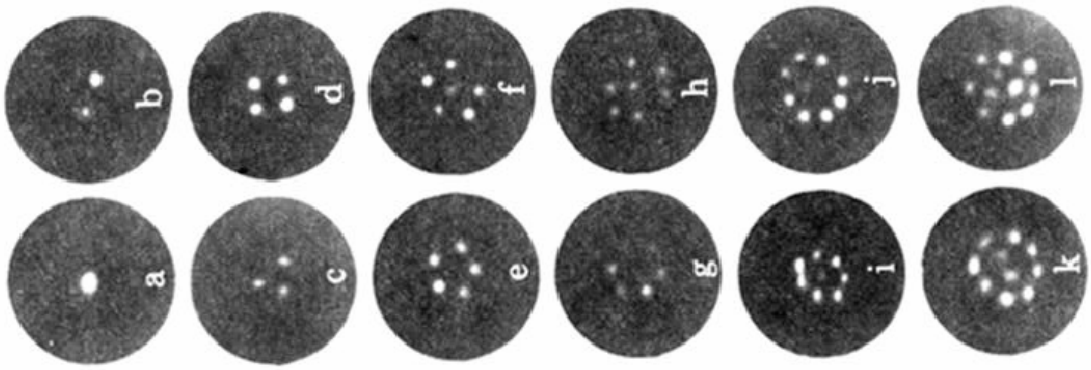


**Figure 6.4**: Data taken from Yarmchuk et al. (1979) is shown. The spots are the ends of quantized vortex cores in a steadily rotating bucket, where they intersect with the free surface. The rotation rate of the bucket generally increases from the left to the right in the sequence of images, as they are oriented here.

As discussed in chapter 3, Chopra and Brown (1957) were the first to seed liquid helium with frozen hydrogen in order to detect fluid motions. Since then, other researchers have made progress with seeding technology. Generally, this work has concentrated on observing fluid motions in He II (e.g., Kitchens et al. 1965), though more recent efforts have approached the problem from the standpoint of classical turbulence (Donnelly et al. 2002). Much of this work is reviewed in chapter 3. Although the efforts to generate particles by freezing substances have focused on doing so directly in He II, we believe this approach is incorrect, as discussed in chapter 3. Our innovation is to generate the particles in He I, as described below, rather than trying to do so immediately in He II. Although there are many reports of particle coagulation in the literature (e.g., Chopra and Brown, 1957), no one has previously reported observation of particles collecting along lines.

Recently, Zhang and Van Sciver (2005) have succeeded in recording images of polymer particles drifting past a cylinder in the midst of a thermal counterflow. Their results represent the first PIV data in He II, but the particle behavior in the fluid is difficult to interpret. These authors use a suspension of 1.7 μm polymer particles that are about 7 times denser than liquid helium. They do not, however, comment on whether the particles clump together or report seeing the particles collect along filaments. We suspect, based on our experiments described in chapter 3, that Zhang and Van Sciver (2005) are observing the motion of particle clumps that are larger than the individual particles.

## 6.2 Methods

A representation of the procedure used to acquire images of particles in He II is shown in figure 6.5. Each of the steps is described in the following sections.

### 6.2.1 The formation of a superfluid

In order to study He II, we cool liquid helium by evaporation. To accomplish this, the cryostat's central reservoir containing the liquid helium is sealed and connected to a vacuum pump through a valve. The grid is manipulated by a magnetic coupling, and all probes enter via feed-throughs sealed with O-rings. The vapor pressure and temperature of the liquid in the bath are lowered by slowly opening the reservoir to the vacuum provided by the pump. A substantial amount of the liquid is lost to evaporation because the process of cooling causes vigorous boiling. The transition temperature for helium, about 2 K below the boiling point at atmospheric pressure, is reached after about

90 minutes of evaporative cooling. Temperatures approaching 1.2 K can be reached using our apparatus, after a substantial amount of additional pumping time.

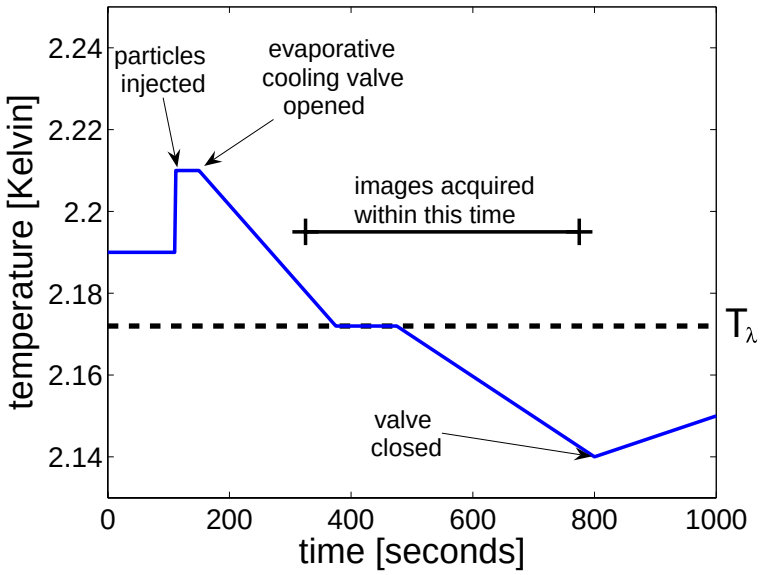


**Figure 6.5**: The time line of an experiment is portrayed in the figure. The relative times, temperatures, and the slopes of the curve are consistent with a typical experiment, though the temperature can be allowed to fall significantly further by leaving open the vacuum pumping valve for longer than indicated.

It is interesting that the work done to cool the system is dominated by cooling of the liquid helium itself. Despite the large mass (about 7 kg) of copper and stainless steel containing the fluid, the specific heat of metals at low temperatures is quite small (of order 0.1 J/(kg K)), and is in fact negligible relative to the comparatively small mass of liquid helium (close to 0.25 kg of liquid helium at about 5000 J/(kg K)).

### 6.2.2 Preparation of the particle suspension in He II

We prepare He II with a suspension of hydrogen particles by injecting a diluted

hydrogen mixture into He I, as described in chapter 3, yielding a fine mist of randomly distributed particles. The suspension of particles in He I is subsequently cooled through the transition temperature to a desired value below the lambda point. Because the particles are buoyant and rise in the fluid, we perform the injection into He I already cooled to a few tens of millikelvin above the lambda point. In this way, we reach low temperatures while the particles remain relatively un-coagulated and within the field of view. Our experience is that the observations described below are possible only if the particles are generated in the warmer state, namely He I.

### 6.2.3 Gathering data near the transition temperature

Temperature is measured using a calibrated semiconductor probe, whose resistance is sensitive to temperature in the range of interest near absolute zero. A current of 10 μA is applied, and the voltage drop recorded by hand from a digital voltmeter. The currents and voltages measured using the four-wire technique. Images of the particles are taken with a digital camera focused on a laser-illuminated sheet that is approximately 100 μm thick, in a manner identical to that described for the PIV technique in chapter 2. In a typical run, the particle suspension is created as in section 6.2.2 with the vacuum pumping line shut off. Subsequently cooling is done rapidly by opening the vacuum valve. This results in a cooling rate of approximately 7 mK/min, though the rate can vary by as much as 50% depending on the amount of liquid in the cryostat. Images are acquired during the cooling process, usually one every few seconds, and the time and temperature are recorded for each image. The times and temperatures recorded for images taken in several runs are collected in figure 6.6.

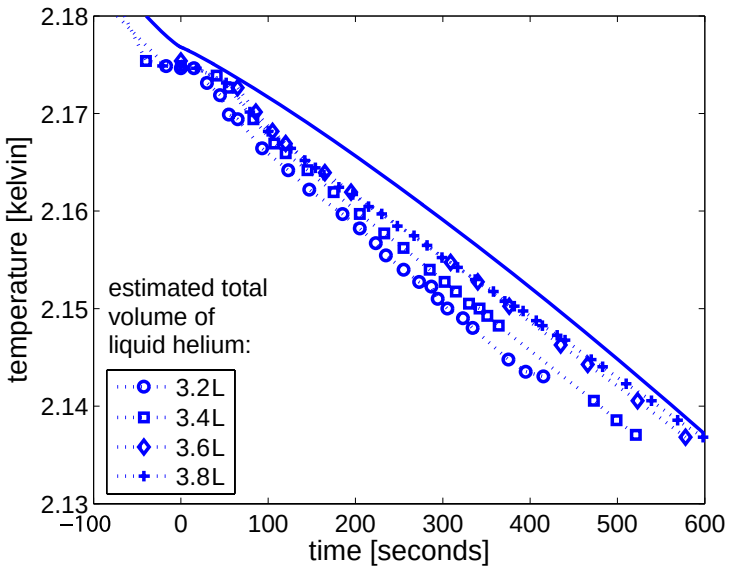


**Figure 6.6**: The times and temperatures for images taken during four selected, but typical, trials. The curves can be compared to the one in figure 6.5. We estimate the net cooling rate as 350 mW from the slope of the curves and the volume of liquid helium. Using this cooling rate, we integrate the heat capacity in figure 6.2 to produce the solid curve shown. The offset of this curve from the data can be attributed to systematic error in the thermometer. However, the origin of the differences of shape of the curves is unknown, and may be due to overturning of the fluid as its density changes near the lambda point.

### 6.2.4 Gathering data in the rotating frame

Observations of rotating flows are conducted in a similar way to those described for rotating grid turbulence in chapter 5. However, there are two important differences. As explained in section 6.2.1, the cryostat is tethered to a vacuum pump in order to cool the liquid helium. In the absence of active cooling, the temperature will rise due to heat leaking into the cryostat. Therefore, we cool the fluid to below the phase transition temperature before spinup, and then disconnect the vacuum pump in order to spin the

cryostat. We cool the fluid by an amount sufficient to keep the fluid below the transition temperature throughout the spinup of the cryostat and fluid, and for the period thereafter during which the measurements are made. We measure the rate of temperature rise in our cryostat to be about 10 mK/min while the cryostat is spinning. The steady state behavior of He II at a fixed rotation rate does not depend on temperature (Donnelly 1967).

Some care is taken in spinning up the fluid, as it is found that the acceleration affects the quality of the data. Greater rotational acceleration tends to result in fewer and larger particles once a steady state is reached. This effect may be due to the more vigorous turbulence caused by rapid spinup, whose effect on the particles is conjectured in section 6.4.4. The size of particles in the resultant rotating superfluid is therefore the product of two competing processes. The first is aggregation in the sense discussed in chapter 3, which progresses steadily with time, and the second is superfluid turbulence induced clumping that is exacerbated as the spinup time is reduced. We find that in order to achieve good results, the final rotation rate is best arrived at over a period of at least five minutes. Once steady rotation of the container is achieved, the total time needed for the fluid to spin up is also found empirically. We increase the spinup time incrementally, until the particles are observed with the movie camera to rotate at the same rate as the container. For the range of rotation rates observed, ten to fifteen minutes are sufficient, and this time is used. Thereafter, image data of the rotating state are captured for about 200 s. This procedure requires cooling the liquid to about 2.0 K before spinup. Finally, we note that the total spinup time is comparable to the time during which we observe a moderate particle aggregation without rotation.

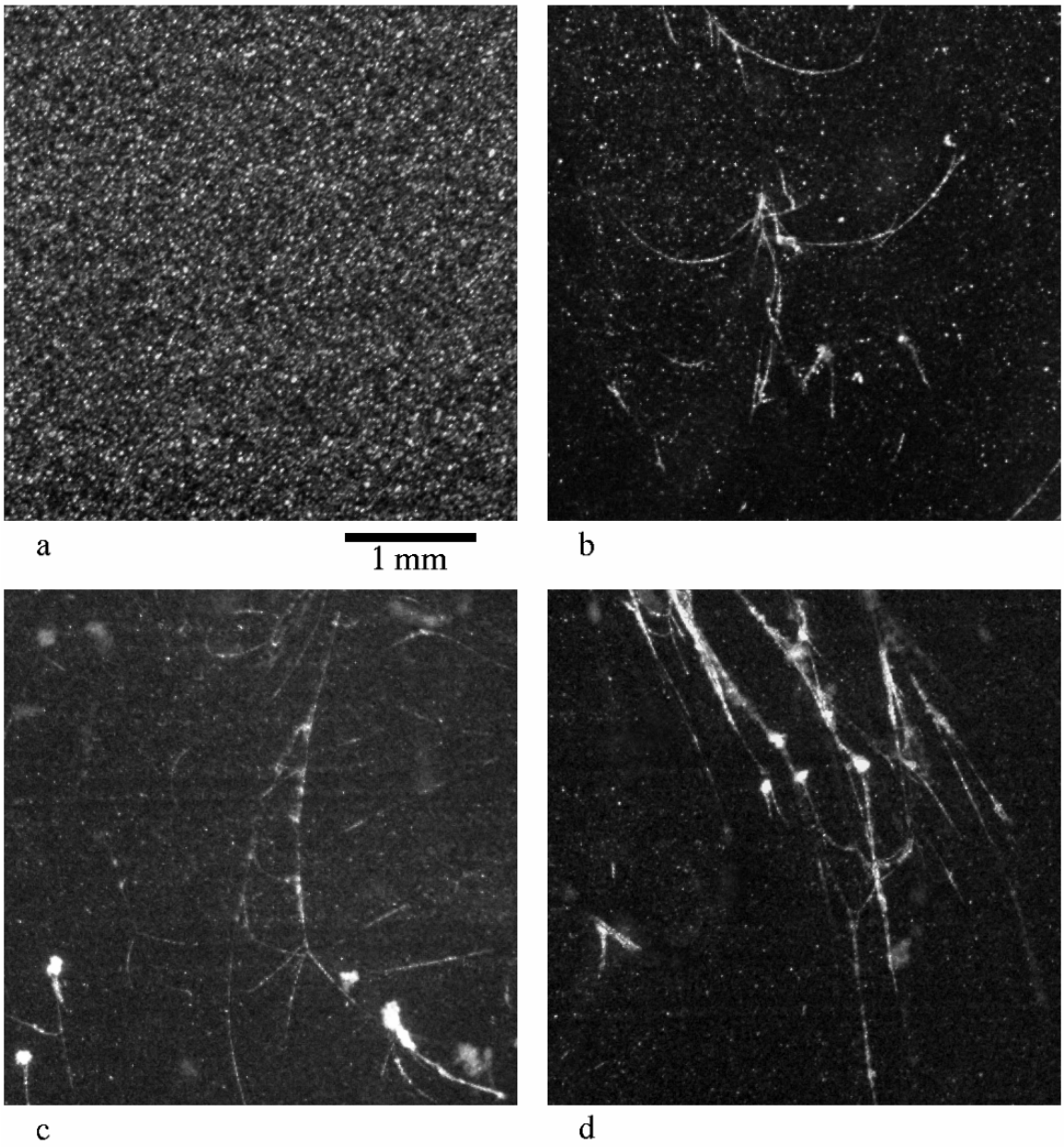


**Figure 6.7**: Panel (a) shows a suspension of hydrogen particles just above the transition temperature. Panels (b), (c), and (d) show similar hydrogen particles after the fluid is cooled below the lambda point. Some particles have collected along branching filaments, while other are randomly distributed as before. Fewer free particles are apparent in (b), (c), and (d) only because the light intensity is reduced to highlight the brighter filaments in the image. The nature of the branching filaments is discussed in section 6.4.

## 6.3 Results

Images show that in He II, a fraction of the particles suspended in the fluid collect onto slender filaments, often several millimeters in length, as in figure 6.7. The remaining particles are randomly distributed, as obtained in He I. We find the filaments at temperatures from a few millikelvin below lambda point down to 1.9 K, and they appear within tens of seconds after the transition temperature is crossed. The filaments evolve slowly as they drift upward through the observation volume at a rate of roughly 1 mm/s. For the results we present below, we do not use the grid, or otherwise disturb the fluid mechanically; we vary only the temperature of the fluid and its rotation rate.

### 6.3.1 The filaments

As is discussed below in section 6.4, it is known that particles can be trapped in vortex cores. The following evidence suggests that the observed filaments are particles collected on such cores. First, the filaments only appear below the transition temperature. Quantized vortex entrapment is the only force we know of that acts on the particles below the transition temperature, and not above. Second, when the liquid helium cell is set in steady rotation, the particles arrange along uniformly spaced lines parallel to the rotation axis, as shown in figure 6.8. This observation agrees with the expectation that quantized vortices form a rectilinear array or lattice aligned with the axis. Third, if we assume that our sheet illuminates a slice of such an array, the density of lines per unit of area normal to the axis of rotation is consistent with Feynman's rule for a series of rotation rates.

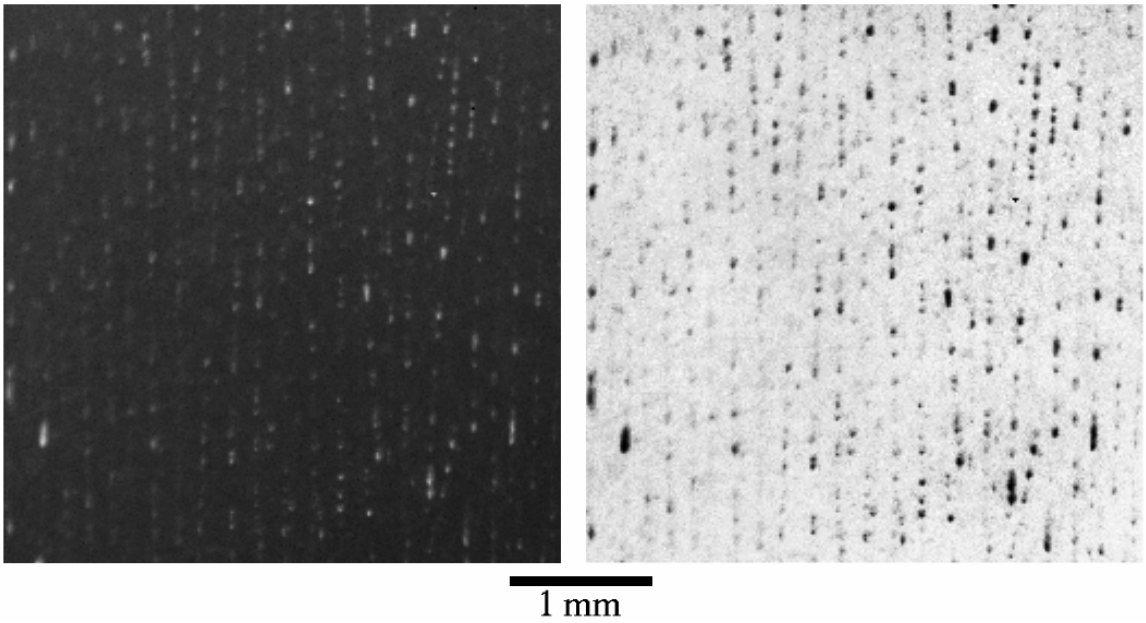


**Figure 6.8**: The picture shows an example of particles arranged along vertical lines. The system rotation axis is vertical. On the left is the original, and on the right is an enhanced and inverted version. The spacing of lines is remarkably uniform, although there are occasional distortions of the lattice and possible points of intersection.

We measure the number density of lines in the image and compare the results with Feynman's prediction under the following four assumptions. The array of vortices appears rectilinear, but we cannot know its underlying geometry because of the orientation of our observation plane. We assume that in a cross section, the vortex cores are at the corners of triangles, and that the laser light sheet illuminates a slice of such a triangular array, as illustrated in figure 6.9. Second, we assume the light sheet is aligned with the lattice by a discrete rotation about the system rotation axis so that the lines appear equally spaced in the image. Furthermore, the alignment is such that this spacing is either the minimum lattice spacing or half of it. Third, we assume that the thickness of the illuminating sheet is roughly equal to the lattice spacing, so that it only illuminates

one row of lines in the lattice. In this case, we measure the minimum lattice spacing, and not its half. Finally, we assume that every vortex in the fluid is decorated with particles, and will be observed if it is illuminated. These assumptions are illustrated in figure 6.9. Clearly these conditions will not always be met – a problem we will address shortly. Although the assumptions may appear stringent, we will show that the general conclusion is favorable even when the conditions hold only approximately.

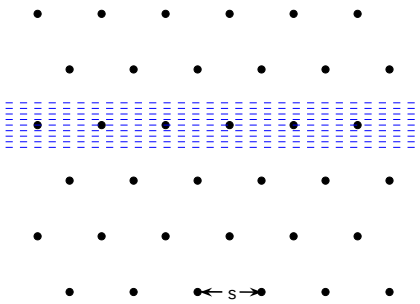


**Figure 6.9**: The axis of rotation is normal to the page. We assume a triangular array of vortices; their intersections with the horizontal plane are indicated by dots. The light sheet also intersects the page, and its cross section is represented by the dashed lines at the orientation relative to the lattice assumed in our calculation of line density.

The images of particles along lines as they appear in rotating He II, as in figure 6.8, show that individual lines remain visible for several rotation periods. Although the lattice undulates slightly with time, it is largely stationary in the rotating frame. (These undulations could be Tkachenko waves, the analogue for a rotating superfluid of the inertial waves described in chapter 5, see Sonin 1987.) Examination of the images also reveals slowly evolving defects in the lattice – places where the lines intersect or fork. The frequency of such defects among experiments appears to increase with particle concentration. In spite of these features, the spacing between lines is

measured by hand in regions of the image where at least three, and preferably four or more, lines appear equally spaced. According to the assumptions just mentioned, the area density of lines as a function of the measured lattice spacing, $s_m$, is

$$n_t = 2 / (3^{1/2} s_m^2). \tag{6.3.1}$$

The resulting data are shown in figure 6.10.

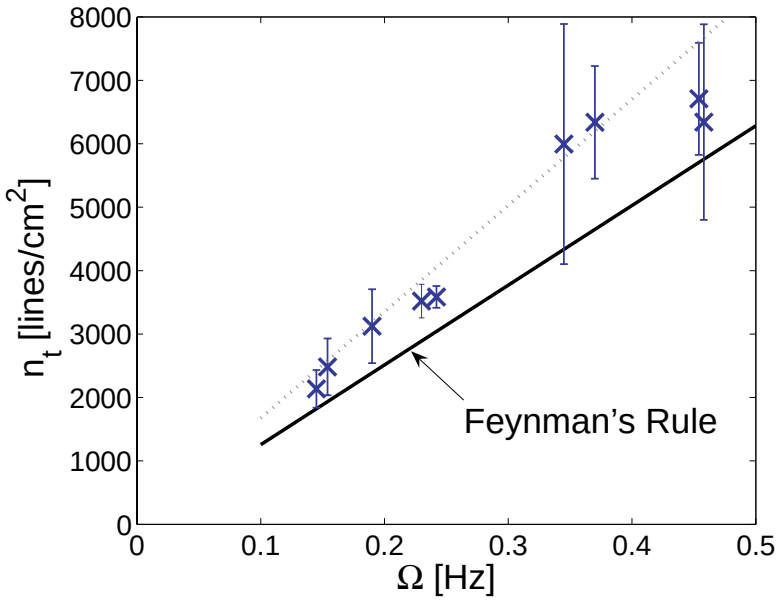


**Figure 6.10**: We compute the density of lines made visible by particles as in figure 6.8, according (6.3.1) and the assumptions discussed in the text. The error bars are the standard deviation of all the measurements made at each rotation rate. Feynman's rule is given by (6.1.14), and the significance of the dashed line is described in section 6.3.2.

### 6.3.2 Review of the assumptions

We show in this section that the measurement of line density is not extremely sensitive to the assumptions outlined in section 6.3.1. We argue, furthermore, that deviations from the assumptions account for the deviations in our result from expectations.

The first assumption concerns the geometry of the array and affects the factor used in converting the line spacing into line density. If, for example, the lines in the array were on the corners of squares instead of triangles, our error is the factor $2/3^{1/2}$ in (6.3.1). The actual line density is then about 14% smaller than we have reported, and closer to Feynman's prediction.

We assume that the sheet aligns with the lattice in such a way that it illuminates a row of equally spaced vortices separated by the minimum spacing of the lattice, $s$. Figure 6.5 shows that the lattice is not perfect, nor should we expect it to be. It is therefore not unreasonable to expect that distortions in the lattice will happen to align it with the sheet locally, in small regions within the extent of the image. Our decision to make measurements only where the lines appear equally spaced is intended to increase the likelihood that the alignment assumption nearly holds.

A sheet thickness that is less than the lattice spacing can be expected to illuminate, when properly aligned, one row of lines separated by the minimum lattice spacing. As described in section 2.1.8, the illuminating sheet of light is formed by expanding a small beam in the vertical direction, and focusing it in the horizontal direction. The camera is aimed at the thinnest portion of the sheet, whose thickness, $d_o$, is roughly 100 μm according to (2.1.1). For the range of rotation rates explored, from 0.46 Hz to 0.15 Hz, we expect from Feynman's rule that the minimum separation between vortices to be between 140 and 250 μm. Our assumption can be expressed as $d_o < s$, and is again reasonable.

It is, of course, possible that the light sheet is not parallel to a row of the vortex lattice. If this were so, the beam might illuminate regularly spaced lines that are,

however, separated by a distance different from the minimum lattice spacing. For a thick beam, the only such angle that is probable is 30 degrees from the one we assumed, and it reveals a spacing that is $3^{1/2}s$. As is illustrated in figure 6.11, if the beam is greater than about $s/2$ in thickness, it is likely to capture two such rows. The resulting measurement, mistakenly attributed to the minimum lattice spacing, yields a calculation of the line density that is in excess by 33%. Much of our data fall between Feynman's prediction and a value that is 33% higher, which we have plotted in figure 6.10 as a dashed grey line.

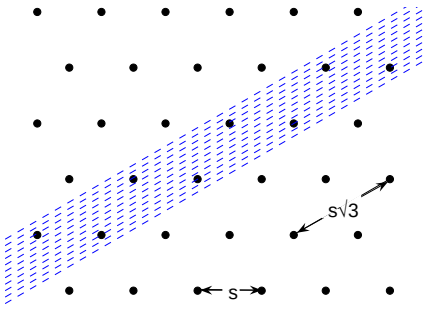


**Figure 6.11**: As in figure 6.9, we show the intersection of vortices with the horizontal plane as spots. However, consider a light sheet orientation different from the simplest one that illuminates a different line spacing than the minimum lattice spacing.

The method described provides only a lower bound on the vortex density in the system. Many vortices may be invisible because they have not collected any particles. However, we consider it unlikely that only a fraction of vortices collect particles and that this fraction appears regularly spaced in the images. If there were uncounted vortices in the light sheet, they would push our result further from Feynman's prediction.

Our vortex count provides only a lower bound for the total circulation they produce, if we allow for the possibility of multiply quantized vortices. If such multiply

quantized lines were present, fewer would be needed to match the system rotation, and the resulting line density measurement would fall below Feynman's rule, instead of above. We take our results to be consistent with the view that each of the lines revealed by particles is singly quantized.

In a final point of detail, on might believe that what appear to be lines are, in fact, the intersections of our light sheet with two-dimensional surfaces stretching through the fluid volume. However, we have observed the lines with volume illumination, with the naked eye, and confirm that they are one-dimensional in character.

### 6.3.3 Evenly spaced particles

Under certain specific conditions, particles are found with remarkably uniform spacing along lines. Some examples are shown in figure 6.12. While the fluid is cooling, the dotted lines appear to form exclusively between 25 and 35 mK below the transition temperature, and about 350 s at our cooling rate after the phase transition occurs. It is not known whether the temperature or the time since transition control the formation of the dotted lines.

The mean separation between particles along lines is about 130 μm, and in figure 6.13 we examine the distribution of spacings in two ways. We find that the separation of particles along a line has a narrow distribution, although the mean separation distance may vary to a greater extent from line to line. This suggests that whatever physics governs the particle spacing is somewhat sensitive to conditions that are local to each particular dotted line.

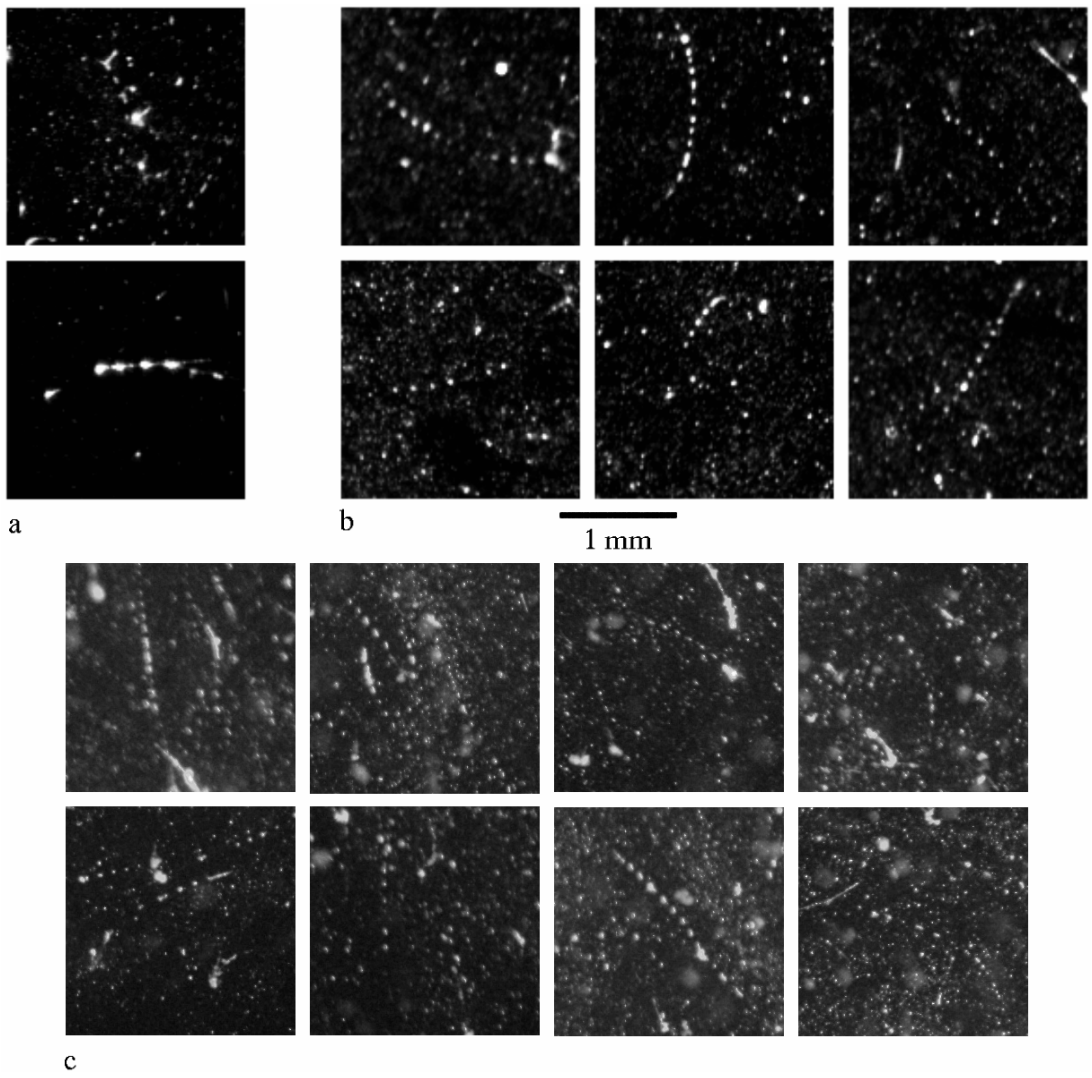


**Figure 6.12**: A series of images of particles regularly spaced along lines, taken during three independent excursions below the phase transition temperature by steadily cooling the fluid (without rotation). In (a), the temperature is 32 mK below the lambda point, and about 350 s have passed since attaining the transition temperature. In (b), the temperature is 25 mK below the lambda point, and about 300 s have elapsed. In (c), the temperature is 28 mK below the lambda point, and about 400 s have elapsed. Temperatures are accurate to within 5 mK, and times within 40 s. Dotted lines such as these were not observed before or after the stated times, or at other temperatures.

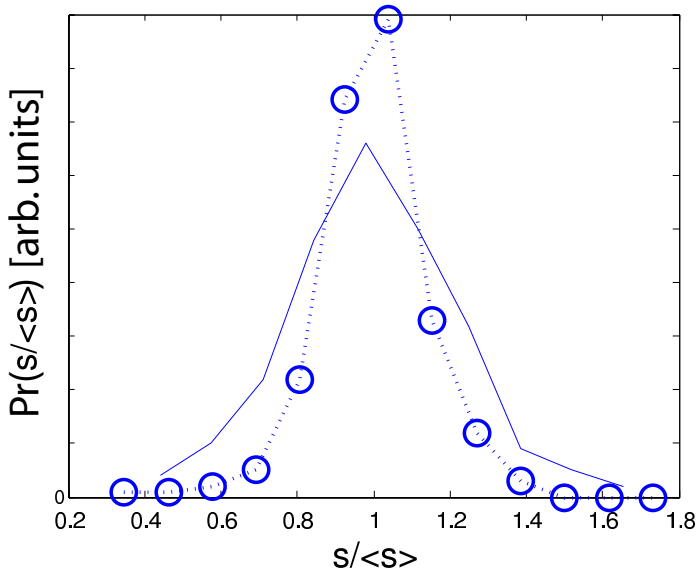


**Figure 6.13**: The circles show the mean of histograms of particle spacings along dotted lines, where the histogram for each line is normalized by the mean spacing along that line. The solid line is the distribution of mean spacings among the different dotted lines normalized by the overall mean spacing. The spacing along a particular line is seen to have a narrower distribution than the difference in spacings between different lines.

## 6.4 Discussion

We have shown in the previous sections that the particles probably collect along filaments which trace the cores of quantized line vortices, and we suggest here a mechanism by which particles are trapped on such cores. In addition, we will explore possible explanations for the complex behaviors exhibited by the filaments, including branched networks and particles evenly spaced along lines. Although particles have been thought of until now only as passive tracers of the flow, our images suggest that the presence of particles in the superfluid may transform the topology of vortex tangles by stabilizing forks in the vortices. Thus, we suggest that He II laced with a particle suspension in many circumstances will behave differently than He II alone. Although

conditions have been established under which particles do not alter the fluid dynamics in classical fluids, the passivity of particles in He II has not been addressed, as far as we know.

### 6.4.1 A particle trapping mechanism

It is known that particles respond in a complicated way to superfluid flows, and that in the context of the two-fluid model they respond to both fluids, and their combined effect depends on the flow conditions (Poole et al. 2005). Parks and Donnelly (1966) showed that ions are trapped by vortices in a superfluid. Ions in liquid helium are hydrodynamically like spheres, though with roughly 1 nm diameters they are much smaller than the hydrogen particles we generate and use. Yet they, too, are substantially larger than the core of the quantized vortices. The following argument is based on the presentation in Parks and Donnelly's paper.

At first glance it is surprising that a vortex can influence the behavior of an object 10,000 times bigger than its core diameter. However, particles are attracted to the cores of quantized vortices by the steep pressure gradient supporting the circulating superfluid. Whether or not a particle is trapped in a vortex core depends on its diameter and on the relative velocities and densities of the normal and superfluid components of the fluid.

To make plausible estimates of the trapping conditions, we note that the centrifugal acceleration of the circulating superfluid is balanced by a pressure field

$$P = -\rho_s \kappa^2 / 8\pi^2 r^2, \tag{6.4.1}$$

for the distance from the vortex centerline, $r$, that is larger than the core radius. Presumably, the pressure flattens out for $r$ values smaller than the core radius, and

reaches a minimum at the vortex core. We consider a fixed vortex in an otherwise quiescent fluid and an initially stationary particle far from the core. The rapidly circulating superfluid exerts no drag on the particle. However, the particle is still subject to the pressure gradient force, which is balanced by friction due to the normal fluid as the particle is drawn toward the vortex core. The actual dynamics are more complex, as the vortex is free to move as well. In this simple model, the force balance yields the equation

$$6\pi a\mu v_n = (4/3)\pi a^3 \nabla P, \tag{6.4.2}$$

where $a$ is the radius of the particle and $\mu$ and $v_n$ are the viscosity and velocity of the normal fluid, respectively. We have used Stokes formula for the drag on a particle in the limit as the particle Reynolds number goes to zero.

Normal fluid velocities relative to the vortex core could arise as a result of thermal counterflows or turbulence in the superfluid. In this case, a relative normal fluid velocity exists above which Stokes drag exceeds the pressure force, and the particle will not be trapped by the line. As a first estimate, we use the particle radius as the distance from the core of maximum attractive force, and find from (6.4.2) that the maximum normal fluid velocity that allows trapping to occur is

$$v_{n,\,max} = \rho_s \kappa^2 / 18\pi^2 a\mu. \tag{6.4.3}$$

According to this model, at 2.10 K a 1 μm diameter particle is dislodged by normal fluid velocities of 2.5 mm/s and higher, relative to the vortex. The particle Reynolds number corresponding to this condition is about 0.1, which is small enough to justify our use of the Stokes drag formula. A bigger particle of the order of 10 μm in diameter will be dislodged by a relative velocity of only 0.25 mm/s. The absolute velocities of particles in the flows we observe are typically about 1 mm/s. These

estimates point to the sensitivity of our technique to particle size and to the need for particles smaller than 1 μm.

It is important to note that in the above analysis, the particle density plays no role. In a classical fluid, a particle is drawn into orbit around a vortex by the action of drag. Once moving in orbit along with the fluid, centrifugal acceleration acts to separate the fluid and particle according to their relative densities, as in a centrifuge. A particle with smaller density than the fluid will 'rise' into the vortex core, and a particle heavier than the fluid will be ejected from the vicinity of the core. It may be that such effects also appear in a more complete dynamical model of the particle-vortex interaction.

### 6.4.2 Trapping time and particle size

We estimate the time required for a newly formed line vortex to collect enough particles to make it visible. We then rearrange the resulting expression to estimate the maximum size for a particle in order for the vortices to become visible within the time of observation.

Consider a stationary vortex that extends through a fluid filled with initially unmoving particles, whose total volume fraction relative to the fluid is Φ, and whose characteristic radius is $a$. The distance between particles in the fluid is then typically

$$l_o = a/\Phi^{1/3}. \tag{6.4.4}$$

Let the vortex be considered 'marked' when all particles within this distance from the vortex centerline have reached the core, according to the mechanism described in section 6.4.1. It can be readily confirmed that this corresponds to a core with particles every 20 diameters, for a typical particle volume fraction of $3 \times 10^{-5}$. If the particle

inertia is small, we can balance the vortex pressure gradient force with drag along its whole trajectory, as in (6.4.2). We construct a timescale by using the velocity, $v_n(r)$, induced by the pressure gradient, such that $v_n$ satisfies (6.4.2). Integrating from a distance $l_o$ to the vortex core, the resulting time scale is given by

$$\tau_v = \int dr / v_n \approx (\mu/2\rho_s)\,(3\pi a/\kappa\Phi^{2/3})^2. \qquad (6.4.5)$$

Similarly, we construct a timescale based on the particle acceleration at a distance $l_o$ from the core, $\alpha_o = F_P/m_p$, where $F_P$ is the vortex pressure gradient force defined in (6.4.2), and $m_p$ is the mass of the particle. This time scale is given by

$$\tau_a = (l_o/\alpha_o)^{1/2} = (\rho_p/\rho_s)^{1/2}\,(2\pi a^2/\kappa\Phi^{2/3}). \qquad (6.4.6)$$

The inertial time scale, $\tau_a$, is $\sim\mu/\rho_s\kappa\Phi^{2/3}$ times smaller than the velocity time scale, for a neutrally buoyant particle of any size. This ratio is usually about $10^3$, so the particle trapping time will always be controlled by viscosity rather than inertia far from the core, which is consistent with our placing of the particle in the Stokes regime. Near the core, more complicated dynamics may take place, but the total time for the particle to reach the core is likely to be dominated by the far field behavior.

Since particle size is a parameter in the trapping time scale, (6.4.5), we use the result to estimate a typical particle size. The filaments appear within tens of seconds of creating He II by crossing the transition temperature. It is therefore reasonable to use this time as an upper bound for the length of time necessary for particles to collect on the filaments. The actual trapping time may, in fact, be much smaller if the time before filaments become visible is determined by their own formation, rather than their decoration. We substitute the particle volume fraction estimated in section 3.7.1, $\Phi = 3 \times 10^{-5}$, and for helium properties at 2.16 K the resulting particle diameter is

$$2a|_{\tau = 100\text{s}} = 0.3\ \mu\text{m}, \tag{6.4.7}$$

which lends additional credence to our expectation that the particles are very small. We may draw from this argument the conclusion that either even smaller particles, or a larger number of particles, are necessary to mark quickly a nascent vortex. In addition, the particles must be 20 times smaller if we demand that they be touching, to form a continuous line, instead of appearing at 20 diameter intervals.

### 6.4.3 The driving force for the formation of vortex filaments

The filaments we observe appear in the absence of any mechanical agitation of the fluid. It is natural to seek the source of energy for the creation of vortices. Because the flows we observe are gentle, with absolute velocities of about 1 mm/s, and remain almost steady over the time a vortex is visible in the image plane, we question whether the flow is turbulent in nature. We find, however, that the flow can probably be described by existing theory about thermal counterflows, as described in section 6.1.7.

Vortices may endure in an observation volume, remnant from the phase transition as described in section 6.1.5. The estimate defined there for the density of residual vortices, $L_r$, is 1.6 $\text{cm}^{-2}$ in our channel, corresponding to about 0.4 mm of line in the volume illuminated by our light sheet and visible to the camera. It is evident in our images (e.g., figure 6.4) that there exist far longer lengths of line, by as much as two orders of magnitude. It is therefore unlikely that the vortices are remnant, though we leave open the possibility that the behavior and subsequent concentration of residual vortices is strongly modified by the presence of particles.

If the He II sample is allowed to sit undisturbed by laser illumination for a period

of several minutes, a nearly filament free state is discovered when the fluid is re-illuminated. Furthermore, the laser intensity has a strong effect on the fluid motion. Unsteady jets with a characteristic velocity of several mm/s emerge from the windows when the beam intensity is above about 2 W. This suggests that a thermal counterflow driven by absorbed laser light at the walls of our channel generates the line vortices. At 2.1 K, the temperature around which most of our observations are made, we make calculations for turbulence driven by a homogeneous counterflow. The critical velocity given by (6.1.15) is $v_c$ = 50 μm/s under these conditions. This value is an order of magnitude smaller than the velocities of the particles and vortices as they drift through our image plane, suggesting that if the observed flow is thermally driven, it is strong enough to sustain superfluid turbulence. We can then express the typical spacing between vortices as the inverse square root of the line density given by (6.1.16) for a homogeneous counterflow. For a counter flow velocity of 1 mm/s, the vortex spacing is

$$1/L_o^{1/2} \approx 1 \text{ mm}. \tag{6.4.8}$$

Here we use the absolute velocity of the particles in the flow as representative of the counterflow velocity. Clearly heating of the fluid in our cryostat is not done under controlled conditions and we should not expect it to result in a homogeneous counterflow. However, the spacing given by the simple analogy is remarkably close to the typical distance between filaments seen in figure 6.4. The result suggests that we are indeed observing a dynamic turbulent flow.

### 6.4.4 Limitations of the observation

We have observed that moderate stirring is effective at gathering the particles into

roughly 30 μm clumps in a matter of seconds. Vortices are likely to bring particles close enough that they bind irreversibly, so that a dense tangle of vortices depletes the fluid of fine particles. The large clumps, though they may also be trapped on vortices, do not successfully mark the outlines of vortices. These considerations point to an important limitation of our technique for marking vortices – that we can see their outlines only in gentle flows with velocities less than a few millimeters per second. Another limitation is that a particle-laden line may behave differently than a line without particles. For these reasons, it may be desirable to minimize the number of particles in the flow. Below we explore the effect of particle number.

As discussed in section 6.1.4, a feature of the two-fluid model is the drag a quantized vortex encounters on passage through the normal fluid, known as mutual friction. We suggest that the drag of particles trapped on a quantized vortex can cause the normal fluid and superfluid to couple more strongly than in the absence of particles. We compare the mutual friction on a vortex line per unit length of line, $f_m$, to the Stokes drag on a sphere per sphere diameter, $f_d$. With the mutual friction given by (6.1.12), this ratio can be approximated by

$$R = f_m / f_d \approx \kappa \rho_s / 3\pi\mu, \tag{6.4.9}$$

an expression that is accurate to within a factor of two between 1.4 K and 2.1 K. A more complete formulation of this ratio, including a parameter describing the temperature dependent strength of the mutual friction, is evaluated and shown in figure 6.14 according to values given by Donnelly (1991). That $R$ is always less than one suggests that the drag on the line is dominated by the presence of the particle. It is probably true that particles interfere with the normal mechanism of mutual friction, and that particle

drag replaces mutual friction when the vortex core is saturated with particles.

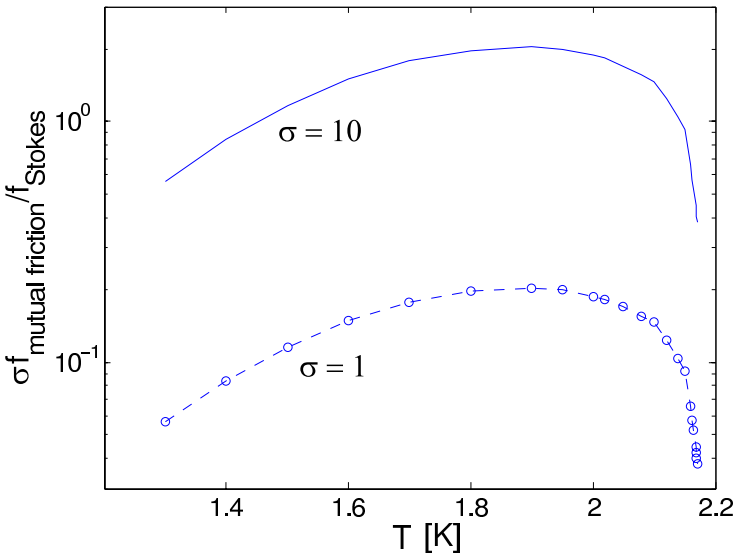


**Figure 6.14**: The chart shows the ratio of the total drag on a vortex due to mutual friction to the drag caused by the presence of particles trapped on the line. We include a factor σ, describing the spacing of the particles. For σ = 1, the particles are next to each other, for σ = 10, they are 10 diameters apart. Particle drag is always stronger than mutual friction if the particles entirely cover the line.

If we allow some space between particles on the line, we can include a factor, say σ, which is the length of vortex line between sphere centers in units of sphere diameters. In figure 6.14, it is evident that σ = 10 will result in the particle contribution to the total drag becoming less important than mutual friction for a wide range of temperatures. Furthermore, in order to distinguish the vortex line from the collection of dispersed particles, we should require that other particle-populated lines be themselves separated by a large multiple of the inter-particle spacing in the bulk. This implies that, under the assumption that the particles do not interfere with the vortex dynamics, there exists an

upper limit on the intensity of the turbulent flow we can observe while tracking individual lines.

We now suggest conditions under which counterflows can be studied using our particles. We suggest that the decorated vortices be separated by at least ten times the particle spacing, or $10\sigma$ diameters, in order to distinguish strings of particles as individual vortices. Consider a collection of vortices decorated with particles spaced typically by 10 diameters. In this case, the typical vortex spacing, $1/L_o^{1/2}$, equals $200a$. From (6.1.16), we see that for a 0.5 μm particle, the maximum counterflow velocity at 2.1 K is roughly 1 cm/s. In addition, according to (6.1.16), vortex density drops with temperature, which indicates that counterflow velocities could correspondingly be increased to maintain the maximum line density at lower temperatures. This result suggests that particles can be used to observe quantized vortex motion over a wide range of turbulent counterflow conditions, provided one has a method to control particle concentration, and provided particles do not interfere with vortex dynamics in other ways. We show in the following section, however, that it is likely the particles do have a dramatic effect on vortex dynamics.

### 6.4.5 The significance of branches

More than one line vortex may trap a particle, and reciprocally, particles may hold collections of vortices together. This interaction may make possible the formation of branches and bundles of vortices. If all of the vortices have one quanta of circulation, Stokes' theorem implies a sum rule fixing the number (always even) and sense of the vortices attached to a particle. However, we are unable to test this rule with existing data,

given that branches may leave the illuminated plane and so go uncounted.

It is evident in our images (see figure 6.4) that the filaments appear as parts of complex networks with stable forks, whereas simulations show the filaments as smooth curves with brief dynamic intersections. We are unaware of any discussion in the literature to date of the possibility that particles in He II transform the topology of a vortex tangle. Poole et al. (2005) mention that a particle may trap more than one vortex, but confine their comment to the case in which the particle diameter is larger than the typical vortex spacing in the flow, and they do not address the consequences. In our experiments, the typical vortex separation is of the order of a millimeter and many orders of magnitude larger than the particles, yet the evidence of multiple vortex-trapping in the form of branching is pronounced. Clearly, more detailed observation and analysis is needed.

### 6.4.6 The dotted lines

Here, we suggest basic principles that may give rise to the dotted lines shown in section 6.3.3. Assume that particles trapped along vortex lines as described in section 6.4.1 are in thermal equilibrium with those free in the volume. This simple picture requires an extremely high temperature to yield average inter-particle separations comparable to the ones observed. The addition to the model of a repulsive potential between particles would make such large separations achievable. Among the possible interaction forces, the electrostatic one is uncommon in that it can just as easily be repulsive as attractive in nature. However, we cannot think of how like charges would accumulate uniformly to produce even spacing, and why the effect would only manifest

itself under specific conditions. We speculate in chapter 7 about alternatives.

## 6.5 Conclusions

We find that particles collect along filaments in He II and show that these filaments probably mark quantized vortex cores. In this way, we have found a method for tracking the vortices, so that their cores can be viewed in three dimensions for the first time. It is almost certainly due to having produced significantly smaller particles that we were able to make these exciting observations. We show that the observed vortices are probably generated by a thermal counterflow, and outline conditions under which such a counterflow can be studied using hydrogen particles. We also discuss several possible pitfalls in the use of particles as passive flow tracers, including the stabilization of vortex intersections.

The images of particles in He II raise a number of interesting questions, including whether the particles contribute to a bending stiffness of the vortex, or cause the vortices to be "sticky" and form branches instead of reconnecting. Both of these mechanisms suggest the possibility that the vortex lines we observe are themselves frozen, the skeletons of a dynamic process that is forced to cease evolving by the presence of particles.

# Chapter 7

# Conclusions and future work

The method for making hydrogen particles that we discovered has made progress possible in several contexts. In chapter 3, we find that the particles are the only ones we know of that are useful for making quantitative measurements of flow velocities in turbulent liquid helium, and that the particles can be used to produce PIV data. Using this technique, we observe the decay of grid turbulence at a higher Reynolds number than previously reported. As discussed in chapter 4, we observe that its decay rate is slightly different from that measured in earlier studies and is a candidate solution for high Reynolds number turbulence. In rotating turbulence experiments described in chapter 5, we find that inertial wave modes of the container are excited in the fluid and that they often dominate the behavior of decaying turbulence in the rotating frame. Finally, we use the hydrogen particles to make visible the cores of quantized vortices in superfluid helium. The images of hydrogen particles along the cores of quantized vortices shown in chapter 6 are probably the first that reveal the geometry and interactions of quantized vortices in three-dimensional configurations.

Although we do not yet have a way to measure directly the size of the hydrogen particles, we find that the particles are likely to be 3 μm or smaller in diameter using

three independent observations. The first argument is described in section 3.7.2, using the number density of particles in the image, and the volume fraction of particles. The second is described in section 6.4.1, and is based on the force required to dislodge a particle from a quantized vortex, and on the estimates of typical flow velocities. Thirdly, we note in section 6.4.2 that the time required for particles to mark a quantized vortex is sensitive to the size of the particles. All calculations support the stated conclusion on the typical particle diameter.

Our experiments are exciting for their discoveries and also for the number of avenues they open for future work. In this chapter, we suggest some opportunities for improvements in the apparatus and for further investigations. These include improved control of experimental conditions, a more detailed investigation of the decay rate of high Reynolds number turbulence, closer examination of inertial wave modes and their effect on rotating turbulence, and several explorations into the behavior of particles in superfluid helium.

## 7.1 Improvements in the apparatus

### 7.1.1 Heat input

The primary limitation of the current apparatus is heat input from the laser illumination, which causes uncontrolled stirring of the fluid. Our small particles must be bathed in intense light in order to be visible to cameras, especially when observing fast dynamics during which the exposure must be short. In practical terms, a beam of a few watts is necessary when the required exposure is less than 1 ms. Empirically, we find that the most important effect of this intense light is to heat the windows' surfaces. The

windows absorb some light and scatter some to the interior walls of the channel that also absorb it.

For experiments in He I, the normal fluid, light impinging on the windows causes convection and boiling. Liquid helium is particularly sensitive to this effect near its boiling point because of its low heat of vaporization and high thermal expansion coefficient. In He II, the heat at the windows causes an easily discernible thermal counterflow across the channel. In either fluid, constant heat input from the laser illumination invariably disturbs and in many cases dominates the flow, but is required only in order to image the flow continuously. Therefore, we believe the only way to probe a liquid helium flow is with brief and intermittent illumination, most easily achieved with pulsed lasers. This procedure would, of course, limit the information that could be gathered about time dynamics, as only one, or a small number, of points in time are observed per experimental trial.

### 7.1.2 Controlling experimental conditions

Further observations of the particle-superfluid system should be made with improved control of experimental conditions toward the goal of repeatability. At least two improvements in the apparatus are needed. First, the injector should allow a batch of particles with predetermined characteristics to be generated. Second, the temperature at which the observations are performed should be controlled better.

The technique for injecting particles is at present a matter of artistry. Two additions to the injector would allow the generation of standardized particles. First, a needle valve should be added and adjusted empirically to control the pressure applied to

the injector. Second, a solenoid valve together with a control circuit should be added to control the duration of the injection. The adjustment of these two settings, along with a control on the concentration of hydrogen in the injected mixture, would probably determine entirely the size and number of the particles that resulted.

Temperature control is a standard tool for almost any low temperature experiment. It would allow investigation of the particle-vortex interaction and He II turbulence under fixed conditions and properties of the fluid. It was not implemented in our apparatus, because the bulk of our experiments were performed with the fluid sitting at its equilibrium temperature at atmospheric pressure. The usual method, however, of over-cooling evaporatively in combination with reheating should be employed when performing experiments in He II. A fixed cooling rate alone will eventually yield a steady state temperature, since there is always heat leaking into the cryostat, but the rate of cooling is difficult to control. The proposed temperature control method would work by setting the cooling rate higher than needed for the desired temperature, and by introducing a continuously controlled amount of heat with a resistive heater.

### 7.1.3 An additional window

An additional window normal to the rotation axis would give a unique perspective on both rotating classical turbulence as well as the lattice of quantized vortices that form in the superfluid. With two cameras for example, we could trace a particle's motion in three dimensions as Voth et al. (2002) have done in water. In the rotating superfluid, we would not have to make assumptions about the form of the vortex lattice; indeed the geometry and time dynamics of the lattice could be investigated.

### 7.1.4 Particle tracking

Although we have invested much work in building the tools for producing and analyzing PIV data, we believe that the best way of using particles to make accurate measurements of turbulent liquid helium flow velocities is to use particle tracking. In chapter 3 we show that the individual hydrogen particles are likely to follow the fluid motions closely. The particle tracking method assigns velocities in space where they are known – at the positions of each particle that is imaged. By tracking the motions of individual particles, rather than ensembles of particles in comparatively large volumes of fluid (as we have done in this work), this technique would remove the barrier to spatial resolution improvement faced by PIV.

## 7.2 Particle characterization

Questions about the nature of the hydrogen particles abound. Their characteristic size and size distribution and how each of these evolves with time are some of the unknowns we have examined only indirectly. The behavior of particle suspensions under turbulent conditions is an active area of research (e.g., Serra et al. 1997), and it is possible that careful monitoring of the clustering of hydrogen particles will yield data beneficial to these scientists. Finding a technique to make these measurements in liquid helium is a challenge. One possible approach is to implement dynamic light scattering, which aims at correlating the fluctuations in the intensity of light scattered from a small volume of suspended particles with their thermal motions. The frequency and amplitude of these thermal motions is a function of the particle size. Another approach may be to monitor

the Brownian motion of individual particles using a microscope, although bringing the particles close enough to the objective of a microscope poses a technical challenge.

## 7.3 Classical turbulence

### 7.3.1 Decaying turbulence in a non-rotating frame of reference

The decay rate of homogeneous and isotropic turbulence is fundamental, and its value as measured experimentally is sometimes used to test computational models of turbulence. It is remarkable that there is no experiment that reliably gives the decay rate of turbulence. Limitations usually are low Reynolds numbers, small durations of observations, or small scaling range. Using our apparatus and methods, we achieve high Reynolds numbers, and observe the flow for significantly longer than others have. We propose repeating the experiments described in chapter 4 for a series of grid velocities and grid mesh sizes. In addition, there are two characteristics of the flow we generate that should be investigated in more detail. These are the mean flow generated by the grid, which we controlled to some extent, and the effect of anisotropy on the resultant turbulence, which we have not explored. The theory of decaying homogeneous and isotropic turbulence at high Reynolds numbers has not been fully developed, either. We believe this may, in part, be due to the lack of appropriate experimental data, such as that which we suggest collecting.

### 7.3.2 Rotating turbulence

As mentioned in chapter 5, we have probed only one small region of the Reynolds number – Rossby number parameter space. Since acquiring the data presented in this

thesis, our methods have improved considerably, notably in particle generation and in control of heat input by the laser. Cleaner and more extensive data may allow more detailed analysis and yield more interesting results.

A problem with our data is the discrepancy between the frequency spectra of the streamwise mean flows in liquid nitrogen and liquid helium in the same geometry. It is possible that a more refined analysis could uncover the reasons for the differences. One idea is to decompose the velocity fields into two parts – the part whose frequencies are less than the inertial frequency, $2\Omega$, that may entirely be inertial waves, and the part with larger frequencies that may be thought of as rotating turbulence. Another way to separate the data may be to identify and extract the spatial structure of the inertial wave modes from the acquired velocity fields, and examine the residue.

Other interesting problems include finding the mechanism by which the dominant inertial wave modes are formed – is their energy content directly injected by the grid motion, or do they interact with and collect energy from smaller scale motions in an 'inverse-cascade' process? Finally, one might work to elucidate the effect of inertial waves on the mechanism by which kinetic energy injected by the grid is dissipated. How is energy redistributed among scales of motion, and how is it ultimately dissipated?

## 7.4 Experiments in He II

The dynamics of the particle – quantum vortex interaction should be explored. Despite the observation that particles interfere with the dynamics of quantum vortices, the system of particles and vortices together reveals some intriguing phenomena. These phenomena include the formation of coarse particle conglomerates when passing through

the superfluid phase transition and the arrangement of particles with equal spacing along lines. Several other experiments could be performed in the superfluid that require some additional equipment and preparation.

### 7.4.1 Quenches through transition

The mist of particles created above the superfluid phase transition temperature of liquid helium shows a marked change of character as the transition is crossed. The particles visibly coarsen in conjunction with the phase change; there appear in the images aggregates of particles that grow in size for several tens of seconds to roughly 50 μm. Although we do not know the origin of these particle clusters, we think it is likely that Casimir forces are responsible. These Casimir forces are analogous to the well-known electromagnetic effect, but derive from random fluctuations in the wave function describing liquid helium near and below the lambda point, rather than from vacuum fluctuations in the electromagnetic field. Because these fluctuations grow near critical points, such as the lambda point, the Casimir force is strongest in the vicinity of the phase transition (Krech 1994). Several authors predict that aggregation in particle suspensions occurs across second order phase transitions (e.g., Burkhardt and Eisenriegler 1995).

Probably the most effective way to affect a rapid phase transition is to vary the pressure; this minimizes the modification of the flow by the convection inherent in evaporative cooling. One way we could accomplish this is by introducing a pressure vessel into the cryostat, and allowing it to fill with the surrounding liquid helium. If the temperature of the fluid is initially slightly below the lambda point, say 2.1 K, rapid phase transitions can be caused by varying the pressure of the liquid between its vapor

pressure, and several tens of atmospheres. The behavior of a particle suspension should be monitored as pressure is released. These observations might reveal some characteristics of the phase transition.

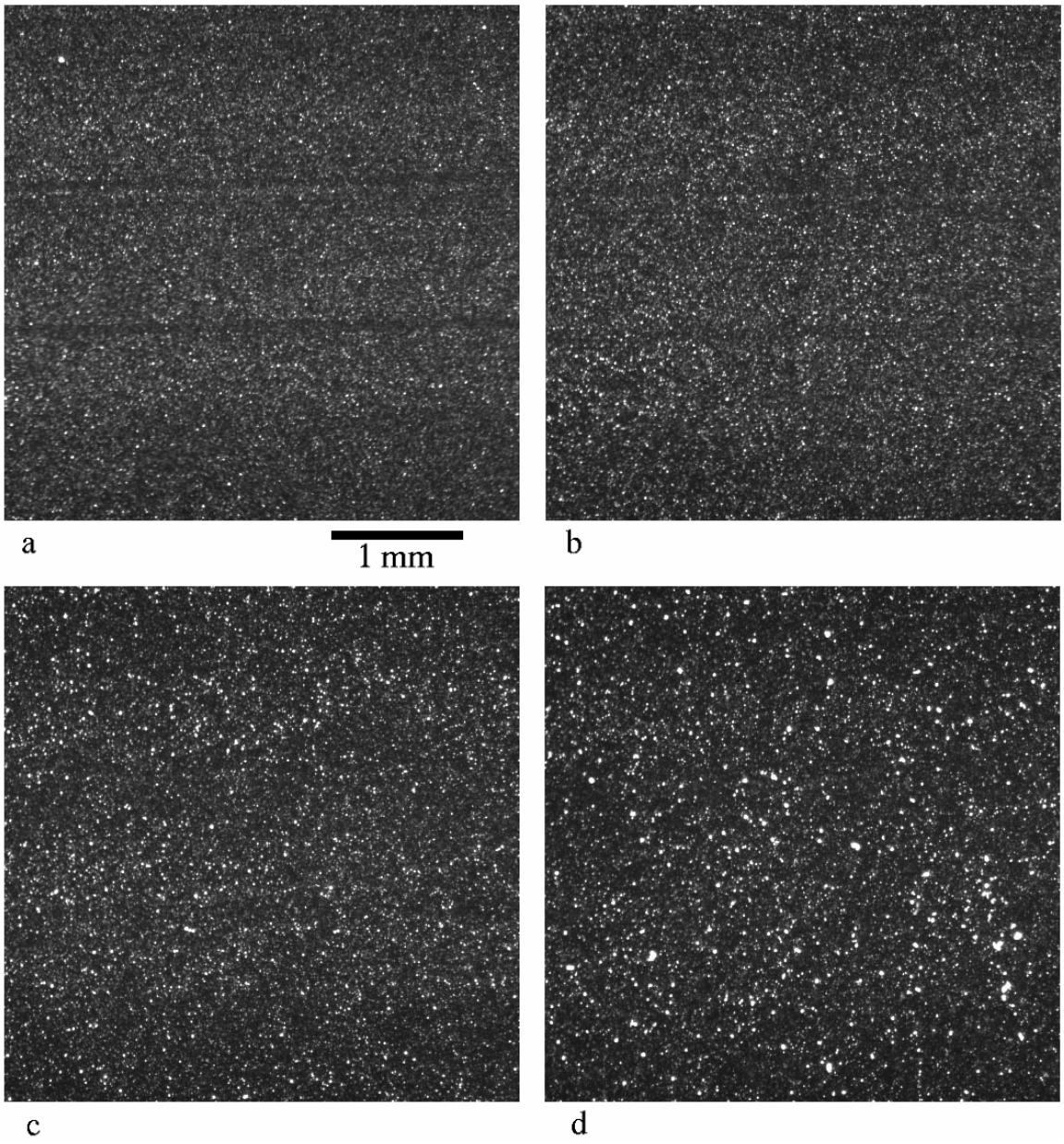


**Figure 7.1**: The panels show the coarsening of a hydrogen particle suspension in liquid helium as the fluid is cooled through the superfluid phase transition. In (a), the temperature is 2.173 K, in (b) it is 2.170 K, in (c) it is 2.167 K, and in (d) it is 2.163 K.

### 7.4.2 Dotted lines

Although we have proposed that a repulsive force is necessary to arrange particles with equal spacing along vortex lines we do not have a complete understanding of the phenomenon. The Casimir force is an intriguing candidate, since its effect grows stronger near the phase transition as discussed in the previous section. We have observed the dotted line phenomenon only near the phase transition. If it is a Casimir-type force that organizes the particles, we believe the result will be interesting to a wide range of physicists. The role of the Casimir force in diverse physical systems and, in particular, whether it manifests itself as a repulsive force (Kenneth et al. 2002), is an active field of research.

### 7.4.3 Tkachenko waves

The rotating lattice of quantized vortices supports transverse waves, called Tkachenko waves, which are propagated by a combination of the tension in individual vortex lines and the elasticity of the vortex lattice. The different types of wave modes of the rotating lattice are discussed by Donnelly (1991) and in a comprehensive review by Sonin (1987). According to these authors, and our own literature search, these waves have not been convincingly demonstrated experimentally in He II, although Coddington et al. (2003) have probably observed them in a Bose-Einstein condensate. It is possible that the undulations we observe in the rotating lattice, described in chapter 6, are the first direct observation of Tkachenko waves in superfluid helium. We propose comparing the frequencies of the observed lattice vibrations, for a series of rotation rates, to those predicted by theory in order to support this hypothesis.

### 7.4.4 Laser tweezers – plucking a quantized vortex

It may be possible to manipulate directly a quantized vortex by optically trapping a particle that the vortex has itself trapped. Such laser tweezers could yield information about the particle-vortex interaction. This technique may make it possible to measure for the first time the tension inherent in a quantized vortex line may be possible.

### 7.4.5 The wanderers

We have observed individual particles breaking from their trajectory parallel to the bulk of particles, and shifting across the background of uniformly drifting particles independently, before conforming to the background flow somewhere else. We ask whether these particles are swept momentarily by the action of a quantized vortex, perhaps one that is normal to the illuminating sheet, and what may be inferred about the turbulent state of the vortices from these observations.

### 7.4.6 Branching and networks

An understanding of the branching structures we observe is central to a complete picture of the role of particles in the dynamics of He II. One way to quantify the effect is to estimate the radial extent of the distortion in a vortex tangle caused by the presence of a single particle. We may begin to find this measure by comparing two more simple states, a rectilinear vortex lattice and a vortex lattice where a certain number of vortices are pinched together by a particle. The two states can be compared energetically to find the maximum number of vortices a particle may collect onto itself, and the linear extent

of the distortion on the vortex lattice. Images of vortices pinched together in the rotating lattice are suggestive of such a configuration. Although such a state may appear to be peculiar, it may give a result that is useful in the general, dynamic case of a turbulent vortex tangle affected by a single particle. This is because vortices that are pinned on a particle lose their identity as single lines, and we may choose to view a collection of aligned vortices trapped on a particle equivalently as a collection of anti-aligned vortices.

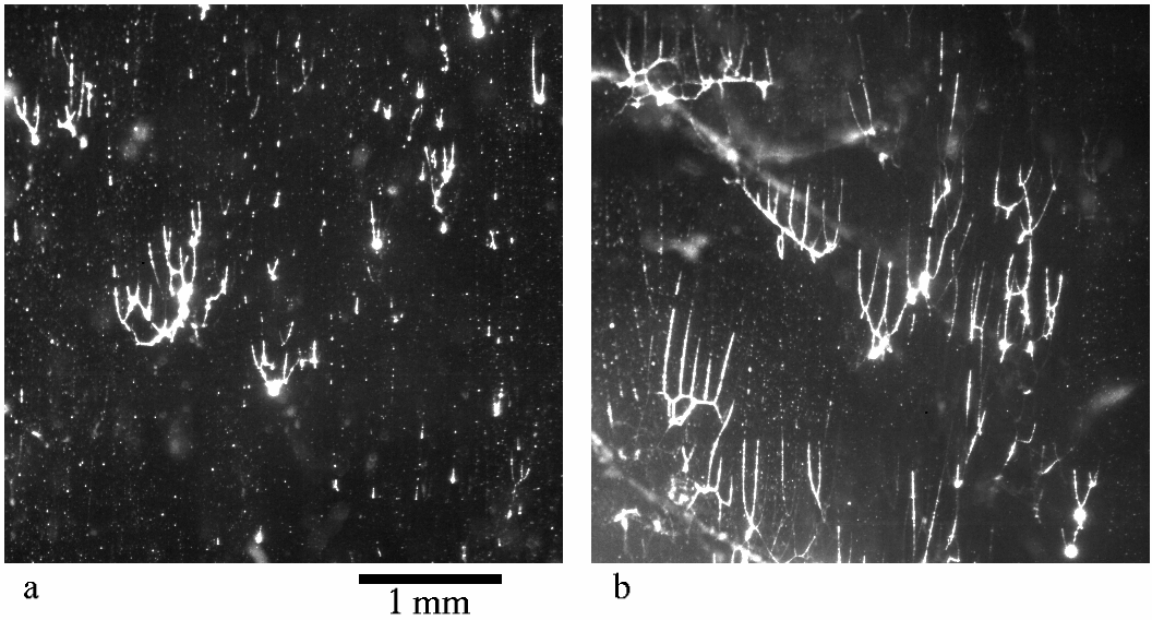


**Figure 7.2**: These images were taken after superfluid liquid helium had reached a state of steady rotation about the vertical axis, as was figure 6.8. It is likely that the presence of a higher concentration of particles in these images has caused the lattice of quantized vortices to pinch together in places.

### 7.4.7 Onset of turbulence

We believe we have shown that particles cannot be considered solely to be passive flow tracers in turbulent He II. Furthermore, because quantized vortices are so effective at agglomerating particles, we believe the utility of particles will be confined to

the laminar regime and to observations during mild forms of quantum turbulence. Experimental observations in this regime are wanting because there is at present no way to probe the fluid. The techniques widely used for measuring the properties of quantized vortices work well only when many of them are present. Donnelly (1991) states explicitly that the lack of understanding regarding the nucleation of quantized vortices is due to the lack of a way of visualizing them.

With these thoughts in mind, the next experiment in He II with hydrogen particles as tracers could study the onset of turbulence in a counterflow between two planes. An implementation of this might place a heater across the entire floor of the channel in the present cryostat. The helium would be seeded, allowed to cool and then reach a quiescent equilibrium at a controlled temperature. At a certain time, a heater would be turned on to deliver a fixed heat flux, and the ensuing transient in fluid flow captured with a series of images, where PIV may be applicable for analysis. The heat would be varied from zero up to a heat flux at which we anticipate the instantaneous destruction of the particle mist by vortex induced agglomeration. We believe that it will be of great interest to know how and when vortices form with increased flow amplitude.

The construction of the heater is more difficult than might be imagined. When constructing a convection cell for classical fluids, it is not difficult to find a material, typically copper, with significantly higher thermal conductivity than the fluid, and to use it to form a surface boundary that remains nearly isothermal. Because of the extremely high thermal conductivity of He II, one must take care in constructing the heated surface so that deviations in the heat flux per unit area over the surface are minimized. One possibility is to deposit a thin nichrome film on a square of electrically insulating

substrate. The electrical resistance of nichrome at low temperatures is nearly unchanged from its value at room temperature, so that it remains an effective heating element at low temperatures. A voltage difference could be applied to copper wires that contact the entire lengths of opposing edges of the nichrome square. The electrical resistance of copper at low temperatures is 6 orders of magnitude lower than it is at room temperature, supplying a nearly uniform current density to the nichrome film across its width.

## 7.5 Closing remarks

We have presented some interesting new results made possible by the development of a technique to produce small hydrogen particles in liquid helium. We find several promising opportunities for future research in fields as diverse as particle suspensions, phase transitions, classical turbulence, and quantized vortex dynamics.

# Bibliography


Baroud, N., Plapp, B.B., She, Z-S. and Swinney, H.L. (2003), "Scaling in three-dimensional and quasi-two-dimensional rotating turbulent flows", *Physics of Fluids*, **15**, 2091-2104.

Batchelor, G.K. (1953), *The theory of homogeneous turbulence*, Cambridge University Press, Cambridge.

Batchelor, G.K. (1967), *An introduction to fluid dynamics*, Cambridge University Press, Cambridge.

Bewley, G.P., Lathrop, D.P. and Sreenivasan, K.R. (2006), "Visualizing quantized vortices", *Nature* **441**, 588.

Boltnev, R.E., Frossati, G., Gordon, E.B., Krushinskaya, I.N., Popov, E.A. and Usenko, A. (2002), "Embedding impurities into liquid helium", *J. Low Temp. Phys.* **127**, 245-258.

Buffet, B.A. (2000), "The earth's core and the geodynamo", *Science*, **288**, 2007-2012.

Burkhardt, T.W. and Eisenriegler, E. (1995), "Casimir interaction of spheres in a fluid at the critical point" *Phys. Rev. Lett.* **74**, 3189-3192.

Cambon, C., Mansour, N.N. and Godeferd, F.S. (1997), "Energy transfer in rotating turbulence", *J. Fluid Mech.* **337**, 303–332.

Campbell, L.J. and Ziff, R.M. (1979), "Vortex patterns and energies in a rotating superfluid" *Phys. Rev.* **B20**, 1886-1902.

Castaing B., Chabaud, B. and Hebral B. (1992) “Hot wire anemometer operating at cryogenic temperatures” *Rev. Sci. Instruments*, **63**, 2442-2446.

Celik, D., Smith, M.R. and Van Sciver, S.W. (1999), “A particle seeding apparatus for cryogenic visualization”, *Advances in cryogenic engineering*, **45**, 1175-1180.

Celik, D. and Van Sciver, S.W. (2002), “Tracer particle generation in superfluid helium through cryogenic liquid injection for particle image velocimetry (PIV) applications”, *Expt. thermal and fluid science*, **26**, 971-975.

Chandrasekhar, S. (1961), *Hydrodynamic and hydromagnetic stability*, Clarendon press, Oxford.

Chopra, K.L. and Brown, J.B. (1957), “Suspension of particles in liquid helium”, *Phys. Rev.* **108(1)**, 157.

Chung, D.Y. and Critchlow, P.R. (1965), “Motion of suspended particles in turbulent superflow of liquid helium II”, *Phys. Rev. Lett.* **14(22)**, 892-894.

Comte-Bellot, G. and Corrsin, S. (1966), “The use of a contraction to improve the isotropy of grid-generated turbulence”, *J. Fluid Mech.* **25(4)**, 657-682.

Dalziel, S.B. (1992), “Decay of rotating turbulence: some particle tracking experiments”, *Applied Scientific Research*, **49**, 217-244.

Dickey, T.D. and Mellor, G.L. (1980), “Decaying turbulence in neutral and stratified fluids”, *J. Fluid Mech.* **99(1)**, 13-31.

Dingle, R.B. (1952), “Theories of helium II”, *Advances in Physics*, **1(2)**, 111-168.

Donnelly, R.J. (1967), *Experimental Superfluidity*, The University of Chicago Press, Chicago.

Donnelly, R.J. (1991), *Quantized Vortices in Helium II*, Cambridge University Press, Cambridge.

Donnelly, R.J. and Barenghi, C.F. (1998), "The observed properties of liquid helium at the saturated vapor pressure", *J. of Phys. and Chem. Ref. Data*, **27**, 1217-1274.

Donnelly, R. J., Karpetis, A. N., Niemela, J. J., Sreenivasan, K. R., Vinen, W. F. and White, C. M. (2002), "The use of particle image velocimetry in the study of turbulence in liquid helium", *J. Low Temp. Phys*. **126**, 327-332.

Feynman, R.P. (1955), "Application of quantum mechanics to liquid helium", *Progress in low temperature physics vol. 1*, ed. Gorter, C.J., North Holland, Amsterdam.

Frisch, U. (1995), "Turbulence: the legacy of A.N. Kolmogorov", Cambridge University Press, Cambridge.

Fultz, D. (1959), *J. Metereol*. **16**, 199.

Glaberson, W.I. and Steingart, M. (1986), "Temperature dependence of the vortex core parameter in He II", *Phys. Rev. Lett*. **26(23)**, 1423-1425.

Greenspan, H.P. (1968), *Theory of rotating fluids*, Cambridge University Press, Cambridge.

Hiemenz, P.C. and Rajagopalan, R. (1997), *Principles of colloid and surface chemistry*, Marcel Dekker, Inc., New York.

Hopfinger, E.J., Browand, F.K. and Gagne, Y. (1982), "Turbulence and waves in a rotating tank", *J. Fluid Mech*. **125**, 505-534.

Huber, G. and Wirth, K.E. (2003) "Electrostatically supported surface coating of solid particles in liquid nitrogen for use in dry-powder inhalers", *Powder technology*, **134**, 181-192.

Ibbetson, A. and Tritton, D.J. (1974), "Experiments on turbulence in a rotating fluid", *J. Fluids Mech*. **68(4)**, 639-672.

Jacquin, L., Leuchter, O., Cambon, C. and Mathieu, J. (1990), "Homogeneous turbulence in the presence of rotation", *J. Fluid Mech.* **220**, 1-52.

Kitchens, T.A., Steyert, W.A., Taylor, R.D. (1965), “Flow visualization in he II: direct observation of helmholtz flow”, *Phys. Rev. Lett.* **14(23)**, 942-945.

Kenneth, O., Klich, I., Mann, A., and Revzen, M. (2002), “Repulsive Casimir forces”, *Phys. Rev. Lett*. **89(3)**, 033001.

Kolmogorov, A.N. (1941), “The local structure of turbulence in incompressible viscous fluid for very large Reynolds numbers”, *Proc. Roy. Soc. A*, (1991), **434**, 9-13.

Kraichnan, R.H. (1967), “Inertial ranges in two-dimensional turbulence”, *Physics of Fluids*, **10**, 1417.

Krech, M. (1994), *The Casimir effect in critical systems*, World Scientific Publishing Co., Singapore.

Kistler, A.L. and Vrebalovich, T. (1966) “Grid turbulence at large Reynolds numbers” *J. Fluid Mech*. **26**, 37-47.

Lamb, H. (1879), *Hydrodynamics*, Cambridge University Press, Cambridge.

Levi, A.C. and Mazzarello, R. (2001), “Solidification of hydrogen clusters”, *J. Low Temp. Phys.* **122**, 75-97.

Lin, C.C. (1948), “Note on the law of decay of isotropic turbulence”, *Proc. N. A. S*. **34**, 540-543.

L'vov, V. and Procaccia. I. (1996), “Turbulence: a universal problem”, *Physics World*, august, 35-40.

Maas, L.R.M. (2003), “On the amphidromic structure of inertial waves in a rectangular parallelepiped”, *Fluid Dynamics Research*, **33(4)**, 373-401.

Maas, L.R.M. (2005), personal communication.

Manders, A.M.M. and Maas, L.R.M. (2003), “Observations of inertial waves in a rectangular basin with one sloping boundary”, *J. Fluid Mech*. **493**, 59-88.

Maurer, J. and Tabeling, P. (1998), “Local investigation of superfluid turbulence”, *Europhysics Letters*, **43(1)**, 29-34.

Maxey, M.R. and Riley, J.J. (1983), “Equation of motion for a small rigid sphere in a nonuniform flow”, *Physics of Fluids*, **26(4)**, 883-889.

McEwan, A.D. (1970), “Inertial oscillations in a rotating fluid cylinder”, *J. Fluid Mech.* **40(3)**, 603-640.

Mei, M.R. (1996), “Velocity fidelity of flow tracer particles”, *Expts. in Fluids*, **22**, 1-13.

Mei, M.R., Adrian, R.J. and Hanratty, T.J. (1990), “Particle dispersion in isotropic turbulence under stokes-drag and basset force with gravitational settling”, *J. Fluid Mech.* **225**, 481-495.

Mohamed, M.S. and LaRue, J.C. (1990), “The decay power law in grid-generated turbulence”, *J. Fluid Mech*. **219**, 195-214.

Moisy, F., Morize, C. and Rabaud, M. (2006), “The decay law of grid turbulence in a rotating tank”, *Conf. on Turb. and Interactions*, Porquerolles, France.

Morize, C., Moisy, F. and Rabaud, M. (2005), “Decaying grid-generated turbulence in a rotating tank”, *Physics of Fluids*, **17**, 095105.

Möttönen, M., Mizushima, T., Isoshima, T., Salomaa, M.M. and Machida, K. (2003), “Splitting of a doubly quantized vortex through intertwining in a Bose-Einstein condensate”, *Phy. Rev. A*, **68**, 023611.

Murakami, M. and Ichikawa, N. (1989), “Flow visualization study of thermal counterflow jet in He II”, *Cryogenics*, **29**, 438-443.

Nakano, A., and Murakami, M. (1992), “Measurement of second sound hemholtz oscillation in he II using laser doppler velocimeter”, *Advances in Cryogenic Engineering*. **37A**, 97-103.

Niemela, J.J. and Sreenivasan, K.R. (2006), “The use of cryogenic helium for classical turbulence: promises and hurdles”

O'Hanlon, J.F. (2003), *A User's Guide to Vacuum Technology, 3rd edition*, John Wiley & Sons, Inc. Hoboken, NJ.

Palaanen, M.A. and Iye, Y. (1985), "Electron mobility on thin He films", *Phys. Rev. Lett.* **55(17)**, 1761-1764.

Parks, P.E. and Donnelly, R.J. (1966), "Radii of positive and negative ions in helium II", *Phys. Rev. Lett*. **16**, 45–48.

Phillips, O.M. (1963), "Energy transfer in rotating fluids by reflection of inertial waves", *Physics of Fluids*, **6(4)**, 513- 520.

Poole, D. R., Barenghi, C. F., Sergeev, Y. A. and Vinen, W. F. (2005), "The motion of tracer particles in He II", *Phys. Rev. B*, **71**, 064514.

Raffel, M., Wilbert, C., Kompenhans, J. (1998), *Particle Image Velocimetry*, Springer Verlag, Berlin.

Reeks, M.W. (1977), "On the dispersion of small particles suspended in an isotropic turbulent fluid", *J. Fluid Mech*. **83(3)**, 529-546.

Roberts, P.H. and Berloff, N.G. (2001), "The nonlinear Schrödinger equation as a model of superfluidity", *Lecture Notes in Physics*, **571**, 236-257.

Saffman, P.G. (1967), "The large-scale structure of homogeneous turbulence", *J. Fluid Mech*. **27**, 581 – 593.

Seidel, G.M., Maris, H.J., Williams, F.I.B., Cardon, J.G. (1986), "Supercooling of liquid hydrogen", *Phys. Rev. Lett*. **56(22)**, 2380-2382.

Serra, T., Colomer, J. and Casamitjana, X. (1997), "Aggregation and breakup of particles in a shear flow", *J. of Colloid and Interface Science*, **187**, 466-473.

Shin, Y., Saba, M., Vengalattore, M., Pasquini, T.A., Sanner, C., Leanhardt, A.E., Prentiss, M., Pritchard, D.E. and Ketterle, W. (2004), "Dynamic instability of a double quantized vortex in a Bose-Einstein condensate", *Phys. Rev. Lett*. **93(16)**, 160406.

Skrbek, L. (2004), “Turbulence in Cryogenic Helium”, *Physica C*, **404**, 354-362.

Skrbek, L., Niemela, J.J. and Donnelly, R.J. (1999), “Turbulent flows at cryogenic temperatures: a new frontier”, *J. Phys.: Condes. Matter*, **11**, 7761-7781.

Smith, M.R., Donnelly, R.J., Goldenfeld, N., and Vinen, W.F. (1993), “Decay of vorticity in homogeneous turbulence”, *Phys. Rev. Lett.* 71,16 2583 - 2586

Smith, L.M., Chasnov, J.R. and Waleffe, F. (1996), “Crossover from two- to three-dimensional turbulence”, *Phys. Rev. Lett.* **77(12)**, 2467-2470.

Smith, L.M. and Lee, Y. (2005), “On near resonances and symmetry breaking in forced rotating flows at moderate Rossby number”, *J. Fluid Mech*. **535**, 111-142.

Smith, L.M. and Waleffe, F. (1999), “Transfer of energy to two-dimensional large scales in forced, rotating three-dimensional turbulence”, *Phys. Fluids*, **11(6)**, 1608-1622.

Sonin, E.B. (1987), “Vortex oscillations and hydrodynamics of rotating superfluids”, *Rev. Mod. Phys*. **59(1)**, 87-155.

Sreenivasan, K.R. (1984), “On the scaling of the turbulence energy dissipation rate”, *Physics of Fluids*, **27(5)** 1048-1051.

Sreenivasan, K.R. and Donnelly, R.J. (2001), “Role of cryogenic helium in classical fluid dynamics: basic research and model testing”, *Advances in Applied Mechanics*, **37**, 239-276.

Stalp, S.R., Skrbek, L. and Donnelly, R.J. (1999), “Decay of grid turbulence in a finite channel”, *Phys. Rev. Lett*. **82(24)**, 4831-4834.

Strykowski, P.J. and Sreenivasan, K.R. (1990), “On the formation and suppression of vortex shedding at low Reynolds numbers”, *J. Fluid Mech*. **218**, 71-107.

Schwartz, K.W. (1985), “Three-dimensional vortex dynamics in superfluid 4He: line-line and line-boundary interactions”, *Phys. Rev. B*, **31(9)**, 5782-5804.

Schwartz, K.W. (1988), “Three-dimensional vortex dynamics in superfluid 4He: homogeneous superfluid turbulence”, *Phys. Rev. B*, **38(4)**, 2398-2417.

Tanner, F.X. (1997), “Liquid jet atomization and droplet breakup modeling of non-evaporative diesel fuel sprays”, *J. of Engines*, **106**, 127-140.

Taylor, G.I. (1935), “Statistical theory of turbulence”, *Proc. Roy. Soc.* A, **151**, 421-444.

Taylor, G.I. and Green, A.E. (1937), “Mechanism of the production of small eddies from large ones”, *Proc. Roy. Soc. A*, **158**, 499-521.

Tisza, L. (1938), *C.R. Acad. Sci. Paris*, **207**, 1035, 1186.

Tkachenko, V.K. (1965), *Sov. Phys. JETP*, **22**, 1282.

Tough, J.T. (1982), “Superfluid turbulence”, *Progress in Low Temp. Phys*. ed. Brewer, D.F., North Holland, Amsterdam.

Vinen, W.F. (1957a), “Mutual friction in a heat current in liquid helium II. I. experiments on steady heat currents”, *Proc. Roy. Soc. A*, **240(1220)**, 114-127.

Vinen, W.F. (1957b), “Mutual friction in a heat current in liquid helium II. III. theory of the mutual friction”, *Proc. Roy. Soc. A*, **242(1231)**, 493-515.

Vinen, W.F. (2006), personal communication.

Vold, R.D. and Vold, M.J. (1983), *Colloid and interface chemistry*, Addison Wesley, Reading, MA.

von Kármán, T. and Howarth, L. (1938), “On the statistical theory of isotropic turbulence”, *Proc. Roy. Soc. A*, **164(917)**, 192-215.

Voth, G.A., La Porta, A., Crawford, A.M., Alexander, J., and Bodenschatz, E. (2002), “Measurement of particle accelerations in fully developed turbulence”, *J. Fluid Mech.* **469**, 121-160.

Wegener, P.P. and Sreenivasan, K.R. (1981), “The effect of cooling rate on binary nucleation”, *Applied Scientific Research*, **37**, 183-194.

Wells, M.R., and Stock, D.E. (1983), "The effects of crossing trajectories on the dispersion of particles in a turbulent flow", *J. Fluid Mech.* **136**, 31-62.

White, C.M. (2001), "High Reynolds number turbulence in a small apparatus", Ph.D. thesis, Yale University.

White, C.M., Karpetis, A.N., Sreenivasan, K.R. (2002), "High-Reynolds-number turbulence in small apparatus: grid turbulence in cryogenic liquids", *J. Fluid Mech.* **452**, 189-197.

Williams, G.A. and Packard, R.E. (1974), "Photographs of quantized vortex lines in rotating He II", *Phys. Rev. Lett*. **33**, 280–283.

Yarmchuk, E.J., Gordon, M.J.V. and Packard, R.E. (1979), "Observation of stationary vortex arrays in rotating superfluid helium", *Phys. Rev. Lett.* **43**, 214-217.

Yeung, P.K. and Zhou, Y. (1998), "Numerical study of rotating turbulence with external forcing", *Physics of Fluids*, **10(11)**, 2895-2909.

Zhang, T., Celik, D., Van Sciver, S.W. (2004), "Tracer particles for application to PIV studies of liquid helium", *J. Low. Temp. Phys*. **134(314)**, 985-1000.

Zhang, T. and Van Sciver, S.W. (2005), "The motion of micron-sized particles in He II counterflow as observed by the PIV technique", *J. Low Temp. Phys*. **138**, 865-870.

Zhang, T. and Van Sciver, S.W. (2005), "Large-scale turbulent flow around a cylinder in counterflow superfluid 4He (He(II))", *Nature Physics*, **1**, 36-38.

Zurek, W.H. (1996), "Cosmological experiments in condensed matter systems", *Physics Reports*, **276**, 177-221.